

# Ultrafast Magnetization Dynamics of Lanthanide Metals and Alloys



Muhammad Sultan

*Im Fachbereich Physik der Freien Universität Berlin eingereichte Dissertation*

February 2012



---

This work was started in October 2007 in the group of Professor Martin Wolf at the Freie Universität Berlin and finished in the February 2012 in the group of Professor Uwe Bovensiepen at the Universität Duisburg-Essen.

Duisburg, February 2012

1<sup>st</sup> Referee: Prof. Dr. Uwe Bovensiepen, Universität Duisburg-Essen

2<sup>nd</sup> Referee: Prof. Dr. Martin Weinelt, Freie Universität Berlin

Day of the defense: May 14, 2012

---



## Abstract

In this study, the laser-induced magnetization dynamics of the lanthanide ferromagnets Gadolinium (Gd), Terbium (Tb) and their alloys is investigated using femtosecond (fs) time-resolved x-ray magnetic circular dichroism (XMCD), the magneto-optical Kerr effect (MOKE) and magnetic second harmonic generation (MSHG). The magnetization dynamics is analyzed from the time scale of a few fs up to several hundred picoseconds (ps). The contributions of electrons, phonons, spin fluctuations, as well as the temporal regimes corresponding to the spin-orbit and exchange interactions are disentangled.

In addition to possible applications in magnetic storage devices, understanding magnetization dynamics in lanthanides is also important because of their different magnetic structure compared to well-studied itinerant ferromagnets. Lanthanides are model Heisenberg-ferromagnets with localized  $4f$  magnetic moments and long range magnetic ordering through indirect exchange interaction. By optical excitation of the conduction electrons, which mediate the exchange interaction, and studying the induced dynamics of the localized  $4f$  and delocalized  $5d6s$  magnetic moments, one can obtain insight into the angular momentum transfer at ultrafast time scales. Moreover, lanthanides offer the possibility to tune spin-lattice coupling via the  $4f$  shell occupation and the concomitant changes in the  $4f$  spin and orbital moments due to Hund's rules. Utilizing this fact, the importance of spin-lattice coupling in laser-induced demagnetization is also analyzed by comparing the magnetization dynamics in Gd and Tb.

By investigating the magnetization dynamics of localized  $4f$  moments of Gd and Tb using time-resolved XMCD, it is found that the demagnetization proceeds in both metals in two time scales, following fs laser excitation, which are classified as: (i) non-equilibrium ( $t \lesssim 1$  ps) and (ii) quasi-equilibrium ( $t \gg 1$  ps), with respect to equilibration of electron and phonon temperatures. The characteristic demagnetization time in this non-equilibrium regime is similar for Gd and Tb, while in the quasi-equilibrium regime it differs following the strength of the spin-orbit coupling.

To disentangle different microscopic mechanisms, conduction electron magnetization dynamics of Gd(0001) is investigated in further detail using time-resolved MOKE. By comparing the dynamics of the  $4f$  moments with the delocalized  $5d6s$  moments, an insight into the angular momentum transfer is obtained and the importance of the intra-atomic exchange interaction is analyzed.

---

The critical spin fluctuations strongly affect the static magnetic properties near Curie temperature ( $T_C$ ). In this study, a real time observation of the critical fluctuations in laser-induced magnetization dynamics near the ferro- to paramagnetic phase transition is described. Moreover, it is concluded that the spin fluctuations contribute to the magnetization dynamics in the quasi-equilibrium regime as well as to the recovery of magnetization while the non-equilibrium dynamics is weakly affected by these fluctuations.

The well known phonon distribution as a function of equilibrium temperatures ( $T_0$ ) allowed us to investigate the role of phonons in magnetization dynamics. From the observed temperature dependence of demagnetization in the quasi-equilibrium regime ( $t \gg 1$  ps), it is concluded that the phonons contribute to the amplitude of demagnetization while the demagnetization time is not affected by them.

In order to disentangle different microscopic contributions in the non-equilibrium regime ( $t \sim 1$  ps), magnetization dynamics is investigated for different laser fluences and equilibrium temperatures by analyzing the MOKE rotation and ellipticity. A slowing down of magnetization is observed with increasing  $T_0$ . Using input from theoretical modeling by the Landau-Lifshitz-Bloch equation, it is shown that both electrons as well as phonons contribute to demagnetization in non-equilibrium demagnetization. Analyzing the dynamics further in the non-equilibrium regime ( $t < 300$  fs) directly after laser excitation, the observation of magnetic as well as non-magnetic contributions is reported.

The comparison of the surface sensitive MSHG and the bulk sensitive MOKE signal gave us the opportunity to investigate the spin-dependent transport processes, which occur from the surface to the bulk of Gd.

Finally, owing to the tunability of spin-orbit coupling in GdTb alloys, ultrafast magnetization dynamics of these alloys is investigated as a function of Tb concentration. The characteristic quasi-equilibrium demagnetization time increases six times by decreasing the Tb content from 70% to Gd metal, due to the known spin-orbit coupling of the system. The non-equilibrium demagnetization time, on the other hand, changes only weakly with concentration due to the fact that this time scale is faster than the spin-orbit coupling.

## Deutsche Kurzzusammenfassung

Die Laser-induzierte Magnetisierungsdynamik der Lanthanid-Ferromagneten Gadolinium (Gd), Terbium (Tb) und deren Legierungen wird mit Hilfe von Femtosekunden (fs) zeitaufgelöstem Röntgenzirkulardichroismus (XMCD), dem magneto-optischen Kerr-Effekt (MOKE) und magnetischer Second Harmonic Generation (MSHG) untersucht. Die Magnetisierungsdynamik wird auf Zeitskalen von wenigen fs bis zu mehreren hundert Pikosekunden (ps) analysiert, um die verschiedenen Beiträge von Elektronen, Phononen und Spinfluktuationen zu unterscheiden und die Zeitskalen der Spin-Bahn- und Austauschwechselwirkung herauszufinden.

Zusätzlich zu ihren Anwendungen in magnetischen Speichermedien, ist das Verständnis der Magnetisierungsdynamik in Lanthaniden auch aufgrund ihrer, im Vergleich zu den intensiv untersuchten *3d*-Ferromagneten, unterschiedlichen magnetischen Struktur von Interesse. Lanthanide sind Ferromagneten mit lokalisierten *4f* magnetischen Momenten, deren langreichweitige magnetische Ordnung durch indirekte Austauschwechselwirkung zustande kommt. Durch optische Anregung der Leitungselektronen, die die Austauschwechselwirkung vermitteln, und die Untersuchung der induzierten Dynamik der lokalisierten *4f* und delokalisierten *5d6s* Momente, kann man Einblick in den Drehimpulstransfer sowie die intra-atomare Austauschwechselwirkung auf ultraschnellen Zeitskalen erhalten. Darüber hinaus bieten Lanthanide die Möglichkeit, die Spin-Gitter-Kopplung über die Besetzung der *4f* Schale und den damit einhergehenden Veränderungen der Spin- und Bahndrehmomente aufgrund der Hundschen Regeln abzustimmen. Unter Verwendung dieser Tatsache wird die Bedeutung der Spin-Gitter-Wechselwirkung in der Laser-induzierten Entmagnetisierung auch durch den Vergleich mit der Magnetisierungsdynamik in Gd und Tb analysiert.

Mittels zeitaufgelöster XMCD-Untersuchungen dieser Dynamik wird festgestellt, dass die Entmagnetisierung nach fs Laser-Anregung in beiden Metallen in zwei Schritten stattfindet: (i) dem Nicht-Gleichgewicht ( $t \lesssim 1$  ps), wenn sich Elektronen und Gitter noch nicht im Gleichgewicht befinden und (ii) dem Quasi-Gleichgewicht ( $t \gg 1$  ps), wenn die Elektronen und das Gitter identische Temperaturen haben. Die charakteristische Entmagnetisierungszeit im Nicht-Gleichgewichts-Regime ist für Gd und Tb ähnlich, im Quasi-Gleichgewichts-Regime unterscheidet sie sich jedoch auf Grund der unterschiedlichen Stärke der Spin-Bahn-Kopplung für beide Materialien.

---

Um die verschiedenen mikroskopischen Mechanismen zu separieren, wird die Magnetisierungsdynamik der Leitungselektronen von Gd (0001) ausführlich mittels zeitaufgelöstem MOKE untersucht. Durch den Vergleich der Dynamik der  $4f$ -Magnetisierung mittels XMCD und der delokalisierten  $5d6s$ -Magnetisierung mittels MOKE erhält man Einblick in den Drehimpulstransfer und die Bedeutung der intra-atomaren Austauschwechselwirkung.

Die kritischen Spinfluktuationen beeinflussen die statischen magnetischen Eigenschaften in der Nähe der Curie-Temperatur ( $T_C$ ) stark. In dieser Arbeit wurde eine Echtzeit-Beobachtung der kritischen Fluktuationen in der Laser-induzierte Magnetisierungsdynamik in der Nähe des ferro- paramagnetischen Phasenüberganges durchgeführt. Darüber hinaus wird der Schluss gezogen, dass die Spin-Fluktuationen auf die Dynamik der Magnetisierung sowohl zum Quasi-Gleichgewichts-Regime als auch zur Relaxation der Magnetisierung beitragen, während die Nicht-Gleichgewichts-Dynamik eher schwach von diesen Schwankungen beeinflusst wird.

Die bekannte Phononen-Verteilung als Funktion der Gleichgewichtstemperaturen ( $T_0$ ) gab uns die Möglichkeit, die Rolle der Phononen in der Magnetisierungsdynamik zu untersuchen. Aus der beobachteten Temperaturabhängigkeit der Entmagnetisierung im Quasi-Gleichgewichts-Regime ( $t \gg 1$  ps) wird der Schluss gezogen, dass die Phononen zur Amplitude der Entmagnetisierung beitragen, während die Entmagnetisierungszeit nicht von Phononen beeinflusst wird.

Um verschiedene mikroskopische Beiträge im Nicht-Gleichgewichts-Regime ( $t \sim 1$  ps) voneinander zu trennen, wurde die Magnetisierungsdynamik für verschiedene Laserfluenzen und Gleichgewichtstemperaturen durch Analyse der MOKE Rotation und Elliptizität untersucht. Eine Verlangsamung der Magnetisierungsdynamik wird mit zunehmender  $T_0$  beobachtet. Durch Heranziehen theoretischer Modellierung der Landau-Lifshitz-Bloch-Gleichung wird gezeigt, dass bei Temperaturen unterhalb der Debye-Temperatur ein durch heiße Elektronen vermittelter Prozess die experimentell festgestellte Entmagnetisierung gut beschreibt. Bei höheren Temperaturen müssen Phonon-vermittelte Prozesse berücksichtigt werden, um die weitere Verlangsamung der Entmagnetisierung zu erklären. Aus der Analyse der Dynamik zu früheren Zeiten des Nicht-Gleichgewichts-Regimes ( $t < 300$  fs) direkt nach Laseranregung, wird auf magnetische als auch auf nicht-magnetische Beiträge zurückgeschlossen.

---

Schließlich gibt uns der Vergleich der oberflächenempfindlichen MSHG mit der volumenempfindlichen MOKE die Möglichkeit, die Spin-Transport-Prozesse, die von der Oberfläche in das Volumen des Gd auftreten, zu studieren.

Aufgrund der Einstellbarkeit der Spin-Bahn-Kopplung in GdTb Legierungen, wurde die ultraschnelle Dynamik der Magnetisierung dieser Legierungen als Funktion der Tb-Konzentration untersucht. Die charakteristische Entmagnetisierungszeit im Quasi-Gleichgewichts erhöht sich um das 6-fache bei einer Verringerung des Tb-Gehalts von 70% bis 0%. Dies wird mit einer Änderung der Spin-Bahn-Kopplung des Systems verknüpft. Die Nicht-Gleichgewichts-Entmagnetisierungszeit hängt nicht von dieser Konzentration ab, da sie auf einer kürzeren Zeitskala stattfindet und nicht durch die Spin-Bahn-Kopplung beeinflusst wird.

---

# Contents

<b>1</b>	<b>Introduction</b>	<b>1</b>
1.1	Previous studies . . . . .	3
1.2	Contribution of this thesis . . . . .	6
1.3	Structure of this thesis . . . . .	8
<b>2</b>	<b>Fundamentals</b>	<b>9</b>
2.1	Magnetism and magnetic interactions in lanthanides . . . . .	9
2.1.1	Indirect exchange interaction . . . . .	11
2.1.2	Spin-orbit interaction . . . . .	12
2.1.3	Magnetic phase transition and critical slowing down . . . . .	14
2.1.4	Electronic structure and magnetic properties of Gd and Tb . . .	16
2.2	Laser-induced dynamics . . . . .	18
2.2.1	Electron dynamics and thermalization . . . . .	18
2.2.2	Phonon dynamics and the two temperature model (2TM) . . . .	20
2.2.3	Spin dynamics . . . . .	24
2.3	Theoretical explanation of ultrafast magnetization dynamics . . . . .	30
2.3.1	Three temperature model (3TM) . . . . .	30
2.3.2	Microscopic three temperature model (M3TM) . . . . .	31
2.3.3	Landau-Lifshitz-Bloch (LLB) equation . . . . .	32
2.4	Magneto-optical techniques as a probe of magnetization dynamics . . .	34
2.4.1	Magneto-optical Kerr effect (MOKE) . . . . .	36
2.4.2	Magnetic second harmonic generation (MSHG) . . . . .	39
2.4.3	Magneto-optical effects in the x-ray energy regime and XMCD .	40

## CONTENTS

---

<b>3</b>	<b>Experimental</b>	<b>45</b>
3.1	Laboratory based setup for magneto-optical characterization . . . . .	45
3.1.1	UHV chamber and sample preparation . . . . .	45
3.1.2	Femtosecond laser system . . . . .	50
3.1.3	Detection system for time-resolved measurements . . . . .	53
3.1.3.1	TRMOKE . . . . .	53
3.1.3.2	TRMSHG . . . . .	55
3.2	Time-resolved XMCD . . . . .	56
<b>4</b>	<b>Laser-induced magnetization dynamics of Gd and Tb</b>	<b>59</b>
4.1	Magnetization dynamics investigated by XMCD . . . . .	60
4.1.1	Quasi-equilibrium demagnetization . . . . .	62
4.1.2	Non-equilibrium demagnetization . . . . .	63
4.2	Comparison of the dynamics investigated by time-resolved XMCD and MOKE . . . . .	66
<b>5</b>	<b>Temperature-dependent quasi-equilibrium magnetization dynamics of Gd investigated by TRMOKE</b>	<b>71</b>
5.1	Influence of temperature on quasi-equilibrium magnetization dynamics .	72
5.1.1	Critical slowing down in the demagnetization . . . . .	75
5.1.2	Comparison with the theoretical models . . . . .	77
5.2	Recovery of magnetization . . . . .	80
5.3	Summary . . . . .	83
<b>6</b>	<b>Non-equilibrium magnetization dynamics investigated by TRMOKE</b>	<b>85</b>
6.1	Laser fluence-dependent magnetization dynamics . . . . .	86
6.2	Effect of temperature on non-equilibrium magnetization dynamics . . .	90
6.2.1	Extraction of concomitant $4f$ and $5d6s$ magnetization dynamics	91
6.2.2	Temperature dependence of non-equilibrium demagnetization time	94
6.2.3	Theoretical modeling based on the Landau-Lifshitz-Bloch (LLB) equation . . . . .	96
6.3	Dynamics within the initial few hundred femtoseconds . . . . .	103
6.4	Summary . . . . .	106



<b>7</b>	<b>Comparison of dynamics: bulk vs surface</b>	<b>109</b>
7.1	Comparison of surface and bulk magnetization dynamics . . . . .	109
7.2	Summary . . . . .	113
<b>8</b>	<b>Magnetization dynamics of the GdTb alloys</b>	<b>115</b>
8.1	Static magnetic properties . . . . .	116
8.2	Concentration dependent laser-induced magnetization dynamics of GdTb alloys . . . . .	118
8.3	Summary . . . . .	122
<b>9</b>	<b>Summary and outlook</b>	<b>125</b>
	<b>Bibliography</b>	<b>129</b>

## CONTENTS

---

# 1

## Introduction

Laser-induced magnetization dynamics has high potential for technological applications [1, 2], however, a microscopic understanding of the underlying processes is essential for device design, optimization and tuning. The technological interest is in their possible applications in magnetic data storage and sensing devices. It always remained an interest to make the devices smaller and faster. Although the size of the magnetic bit is entering into the nanoscale following the so-called Moore's law, which suggests the doubling of the data density in every eighteen months, the processing speed of magnetic information is almost saturated in the range of MHz frequencies [3]. The conventional way to record a magnetic bit is to reverse the magnetization by applying a magnetic field and reversing the magnetic state of an individual domain by domain wall motion and nucleation. The bottleneck in conventional magnetic storage processing is the precessional dynamics which require extremely strong magnetic fields to increase the processing speed. Although due to constraints to produce the current-induced magnetic field pulses as well as precessional dynamics, the current generation of magnetic storage devices already approaches their fundamental limits. Even if such short magnetic field pulses with a very strong magnetic field strength were available for a device, it was shown that the magnetization reversal does not take place if the magnetic field pulses are shorter than 2 ps [4]. Therefore alternative techniques for controlling magnetization can be beneficial. One of the emerging approaches to control the magnetic information is ultrafast optical manipulation of magnetic state [5]. Interaction of collective magnetic excitations with lattice fluctuations, known as spin-lattice relaxation, is thought to limit the speed in magnetic data storage [4]. Angular momentum conservation de-

## 1. Introduction

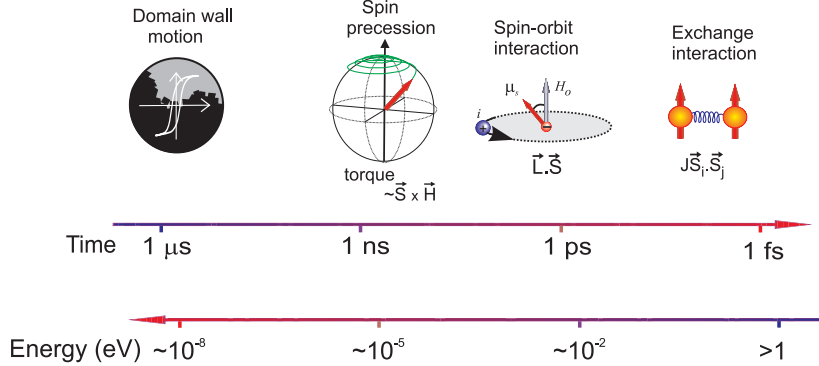


**Figure 1.1:** Magnetic phenomena and estimates of their energies with relevant time scales calculated by  $t = h/E$  [9],  $h$  is the Planck's constant.

mands that excitations faster than spin-lattice relaxation, on the timescales of 0.1-1 ns [6, 7, 8], are spin-conserving. As the fundamental processes occurring at the ultrafast (femtosecond to picosecond) time scale are not yet well understood, this approach requires further investigation to understand the microscopic mechanisms which can lead to device applications. Probing the magnetization dynamics at the ultrafast time scale can open new horizons for the applications of magnetic materials in information technology, especially when it is shown that the laser-heat-induced magnetization switching is possible in two distinct sublattice ferrimagnet at femtosecond time scale [2].

In addition to its technological relevance magnetization dynamics driven by femtosecond laser pulses has opened a new field of the magnetism, the *femtomagnetism*. The understanding of the microscopic processes requires diverse treatment when different systems, like electron, phonon and spin, are in a strong non-equilibrium state. The new and interesting physics emerges as the investigation of dynamics approaches the time scale of the fundamental interactions responsible for and/or affecting ferromagnetic order. These include the exchange interaction, spin-orbit (SO) coupling, electron-phonon coupling, and electron-electron scattering etc. The summary of the most important interactions and magnetic phenomena with the respective time scales is presented in figure 1.1. It remained always an interest to know how fast one can modify the magnetic state of a system. Since a change of the magnetic state requires angular momentum conservation, this question becomes more and more important when components of the system, that is electron, lattice and spin, are getting isolated in a strong

non-equilibrium state after fs laser excitation. The most famous and established mechanism of the magnetization dynamics is the precession of the magnetization, which can be described by the Landau-Lifshitz-Gilberts (LLG) equation [10]. With easily producible magnetic fields this phenomenon takes place at the nanosecond time scale. The question arises whether it is possible to reverse the magnetization at a time scale faster than the period of the precession. In more specific terms it remained an open question: how fast, between which reservoirs and through which mechanisms can angular momentum be exchanged? And is the angular momentum transfer even possible on time scales shorter than that of the spin-orbit or exchange interaction? The transient states, generated by the femtosecond laser, may require the non-equilibrium approach to explain the phenomenon. This study is focused on the ultrafast magnetization dynamics of lanthanide elements which are not only important constituents in modern data storage materials [1, 2, 11, 12] but are also important materials as Heisenberg-like ferromagnets. The bulk magnetization dynamics of these metals at the femtosecond time scale has not been investigated so far.

## 1.1 Previous studies

To investigate the dynamics at femtosecond time scale a novel pump-probe technique can be used. In all-optical pump-probe experiments the magnetization dynamics is driven by an external stimulus laser pulse called "pump" and a second time-delayed laser pulse<sup>1</sup> "probe" study the dynamics induced by the pump. The principle of this time-resolved technique is shown in the inset of figure 1.2 where first laser pulse excites the magnetic sample and a time-delayed second pulse study the dynamics, for example by the magneto-optical Kerr effect (MOKE). One of the first time-resolved experiments on magnetic material was on Gd, where the response time of the material was of the order of 100 ps [6]. Since the pulse duration of the excitation laser was nanoseconds which was three order of magnitude longer than the electron-phonon equilibration, the dynamics related with the non-equilibrium state of electrons and phonons was not distinguished in that experiment [6]. The availability of ultrashort laser pulses

---

<sup>1</sup>The ultrashort x-ray pulses, electron beams and emitted photo-electrons are also used as a probe in routine now a days.

## 1. Introduction

---

made it promising to use the magneto-optical techniques to investigate the dynamics at femtosecond time scale.

The real field of ultrafast magnetization dynamics was triggered with the first time-resolved magneto-optical measurements with a fs laser on Ni by Beaurepaire et al. [13], where sub-picosecond quenching of magnetization was observed upon fs laser excitation, as shown in figure 1.2. This behavior was later confirmed by number of studies with the variety of techniques including magnetic second harmonic generation [14] and photoemission spectroscopy [15]. Demagnetization at the same order of time scale was also observed on Co [16]. The magneto-optical response, as a probe of magnetization, following fs laser excitation was challenged by comparing the MOKE rotation and ellipticity [17]. It was shown that the magneto-optical response can be affected by state filling effects within initial few hundred fs after optical excitation [17, 18, 19]. Using time-resolved photoemission on Ni, Rhie et al. showed that the demagnetization and recovery of magnetization takes place at characteristic time scales of 300 fs and 3.2 ps, respectively [20]. Later Bigot et al. claimed that the magneto-optical response from the CoPt<sub>3</sub> film shows the true magnetization dynamics. From the study of ferro- and ferrimagnetic compounds, it was revealed that the spin-orbit coupling contribute to ultrafast magnetization [7]. Laser-induced spin reorientation [21] and the photo-induced phase transition was observed on the sub-picosecond time scale [22, 23]. For the angular momentum conservation Bigot et al. [24] and Zhang et al. [25] suggest that the light field is involved in magnetization dynamics. Recently Battiato et al. proposed superdiffusive spin transport as a mechanism of ultrafast demagnetization [26]. It is now established that in laser-induced demagnetization a fs laser pulse excites the electrons which equilibrate with each other and with the lattice through electron-electron and electron-phonon scattering, respectively, within a few ps after excitation [27]. The response of the magnetization to the excitation of electron and lattice sub-systems depends on the material characteristics and excitation conditions as discussed above.

Despite experimental progress to observe the fundamental time scales of demagnetization in itinerant ferromagnets and a number of alloys [7, 28, 29, 30, 31, 32], no theoretical model explained the diversity of the observed time scales of demagnetization. To explain the first time-resolved results of Gd [6], Hübner and Bennemann [33] suggested a theoretical explanation based on the spin-lattice relaxation and extracted a time scale of  $\tau_{SL}=48$  ps for Gd. Using the thermodynamic temperatures, specific

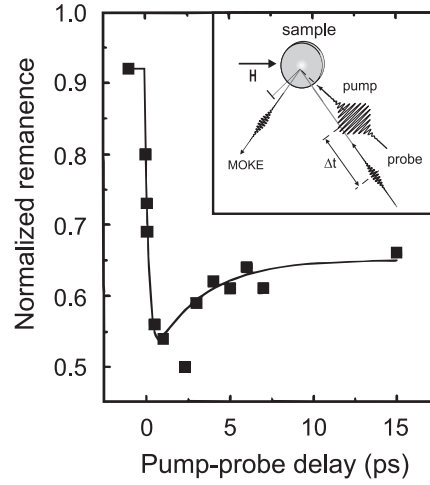


**Figure 1.2:** Change in the MOKE signal following femtosecond laser excitation on Ni. The first time-resolved experiment showing demagnetization at the sub-picosecond time scale, Ref [13]. The inset shows the basic principle of the pump-probe experiment.

heats and coupling parameters of the electron, phonon and spin systems, the three temperature model was suggested to explain the evolution of the magnetization [13]. However the question of angular momentum conservation was not addressed in this model. To include the angular momentum conservation Koopmans et al. suggested a theoretical model based on the LLG equation [34]. Most of these studies are material specific. It is important to mention that recently efforts have been made to explain the diversity of the ultrafast magnetization dynamics. First, the Landau-Lifshitz-Bloch (LLB) model, which is a modified version of the LLG equation, is now used to explain the ultrafast demagnetization [35, 36]. Second, a phenomenological model developed by Koopmans and coworkers based on spin-orbit mediated electron spin-flip scattering [37] has also been proposed. Here an attempt has been made to explain demagnetization in itinerant and rare earth ferromagnets with the same model. In addition, a study of spin dynamics by solving the Boltzmann equations showed another potential explanation [38]. All of the above models have been applied to specific systems and sometimes the same experimental results were explained by two different models with different fundamental basis [26, 37]. The lack of the systematic study of magnetization dynamics could be one reason for such contradictions. In this perspective the goal of this thesis is to test which of the above mentioned models can explain the ultrafast magnetization dynamics of lanthanide ferromagnets.

## 1. Introduction

---

Considerable attention has already been given to the demagnetization of itinerant ferromagnets [14, 30, 39, 40]. These materials demagnetize well below 1 ps after laser excitation, on a similar time scale or even faster than the electron lattice equilibration. Simultaneous temporal evolution of electron, lattice and spin sub-systems and their interplay hinders the separation of the individual contributions to demagnetization. Lanthanide metals, specifically Gd, could be one of the potential systems to disentangle the different contributions due to their slow response to laser excitation, which results from the weak and indirect  $4f$  spin-lattice coupling [6, 33]. In addition to that, the lanthanide ferromagnets present long range magnetic order mediated by indirect exchange interaction and spin polarization of the conduction electrons. The excitation of the conduction electrons, and their effect on the localized and itinerant magnetization dynamics is also a rarely explored area of research.

In view of angular momentum conservation a change in the magnetization requires transfer of angular momentum from magnetization to some other reservoir. The crystal lattice is a prominent candidate here, which turns spin-lattice coupling into an essential, but barely investigated interaction in ultrafast magnetization dynamics. In addition to the indirect magnetic coupling, Gd and Tb are also special cases of spin-lattice coupling. Due to half filled shells, the  $4f$  orbital moment of Gd is zero, which leads to a weak  $4f$  spin-lattice coupling while Tb has strong spin-lattice coupling. This property of the lanthanide ferromagnets can be utilized to explore the role of spin-orbit coupling in ultrafast magnetization dynamics. The dynamics on the surface of Gd has been studied in our group recently [27, 41, 42, 43], which shows demagnetization within the laser pulse duration. Now it remains an open question how fast demagnetization in the bulk of lanthanides proceeds after excitation with the femtosecond laser?

### 1.2 Contribution of this thesis

This thesis comprises the discussion of the magnetization dynamics of lanthanide ferromagnets investigated by the time-resolved techniques.

The important aspect of this project is to exploit the magnetization dynamics from several hundred picoseconds down to few femtoseconds. In this way one can see the difference of dynamics at the time scale of the equilibrium spin-orbit and exchange in-



teraction, when the exchange and spin-orbit interactions become time-dependent quantities.

The study of dynamics was started by employing the time-resolved x-ray magnetic circular dichroism (XMCD) at the  $M_5$  absorption edges of Gd and Tb, which probes directly the  $4f$  magnetic moment out of reach for magneto-optical techniques. Comparing the dynamics of Gd and Tb reveals the role of the spin-orbit coupling on demagnetization. The magnetization dynamics is divided into two regimes: *nonequilibrium* demagnetization within few picoseconds when electron and phonon have different temperatures; *quasi-equilibrium* demagnetization when electron and phonon temperatures are already equilibrated and spin evolves to reach in equilibrium with lattice.

The dynamics is further investigated by the time-resolved magneto-optical Kerr effect which in principle probes the dynamics of the  $5d6s$  magnetic moments. By comparing the  $4f$  and  $5d6s$  magnetization dynamics, possible mechanisms for the loss of angular momentum are discussed.

Owing to well-defined phonon distributions as a function of temperature, the temperature dependent demagnetization is examined. The results are compared with the recent theoretical models, M3TM [37] and LLB [36] model, published during the course of this thesis. Spin-orbit coupling, exchange interaction, hot electron and phonon mediated demagnetization and temporal regimes when these interactions are important are also analyzed. Moreover, contributions of the spin fluctuations, near the ferro-to paramagnetic phase transition, which present a sizeable energy content of the system particularly in excited magnetic systems [44] are also investigated in time domain experiments.

The time-resolved magneto-optical Kerr effect and magnetic second harmonic generation optical pump-probe measurements give the access to the dynamics of bulk and surface magnetization, respectively. In this way the contribution of the spin transport from the surface of the Gd is also investigated. Since an optical wavelength is employed in the experiment, it is reasonable to assume that MOKE is primarily sensitive to the  $5d$  magnetic moment as well as potential non-magnetic contributions to MOKE [17, 18, 19]. This issue is also addressed in this project.

After studying the detailed magnetization dynamics of Gd and Tb metals, the tunability of the magnetization dynamics through the spin-orbit coupling of the GdTb alloys is also analyzed.

## 1. Introduction

---

### 1.3 Structure of this thesis

Chapter 2 of this thesis deals with the theoretical background of the investigated systems and employed techniques. In chapter 3, the experimental techniques used in this project are discussed. The experimental results are discussed from the chapter 4 where first time-resolved XMCD measurements on Gd and Tb metals and their qualitative comparison to the time-resolved MOKE technique is given. The equilibrium temperature dependence of magnetization dynamics is discussed in chapter 5 and 6 separating the quasi-equilibrium and non-equilibrium dynamics, respectively. The role of electrons, phonons and critical spin fluctuations is investigated in those chapters and compared to the theoretical modeling based on LLB equation. Variation of magnetization dynamics as a function of laser fluence is provided in the same chapter. Chapter 6 also deals with the demagnetization dynamics within initial few hundred femtoseconds. The effect of temperature on the recovery of magnetization is discussed at the end of chapter 5. Chapter 7 deals with the comparison of the surface and bulk demagnetization. In chapter 8, possibility to control the magnetization dynamics through the spin-orbit coupling is discussed by investigating the concentration dependent ultrafast magnetization dynamics of GdTb alloys. The last part of the thesis summarizes the major results of the thesis and outlook for future investigations.

## 2

# Fundamentals

In this chapter, basic physics and the theoretical background of the investigated systems and techniques, employed in this project, are discussed. It includes: a general overview of magnetism and the magnetic properties of lanthanides; excitation of material with laser and subsequent dynamics of electrons, phonons and spin systems. The interaction processes between different sub-systems and their coupling for the sharing of energy and/or angular momentum after laser excitation will be addressed. In an overview, recent theoretical models relating these sub-systems are discussed with special consideration of rare earth ferromagnets. In the last section, the basics of linear, nonlinear and x-ray magneto-optical effects will be discussed briefly. In the first section I will start with a discussion of the magnetism and magnetic properties of the lanthanides.

## 2.1 Magnetism and magnetic interactions in lanthanides

The characteristic feature of ferromagnetism is the interaction of the spins and hence spontaneous alignment of magnetic moments even in the absence of an external magnetic field. Magnetic moments are oriented along a particular direction (anisotropy) depending on the crystal structure. The parallel alignment of all the moments requires a strong magnetic field. The well known magnetic dipolar interaction between atomic spins is of the order of 1 K which cannot account for the ferromagnetism at the temperatures of several 100 to 1000 Kelvin<sup>1</sup>. To explain the ferromagnetic ordering, in 1907 Weiss suggested the idea of an internal molecular or mean field, exerted on a moment

---

<sup>1</sup>The Curie temperature for Gd and Tb is 293 K and 220 K, respectively.

## 2. Fundamentals

---

by the rest of the magnetic moments, which is proportional to the magnetization of the sample. The origin of this field was explained by Heisenberg in 1928 by introducing the concept of *exchange interaction*. The exchange interaction has quantum mechanical origin as a result of the electrostatic coulomb repulsion of electrons on neighboring atoms and the Pauli exclusion principle, which forbids two electrons from entering the same quantum state. Depending on the presence of the mediator for the exchange, the interaction can be classified as direct or indirect. The overlap of the nearest neighboring electron orbitals result in direct exchange, in most of itinerant ferromagnets magnetic ordering is through direct exchange. In some magnetic materials the direct overlap of the neighboring electron orbitals is very small and the long range magnetic order is established through the intermediate electrons<sup>1</sup>. This type of interaction is called indirect exchange or Ruderman-Kittel-Kasuya-Yosida (RKKY) interaction. Since the lanthanide ferromagnets belong to this category, it will be discussed in detail in this section, before the basics of magnetism are introduced below.

The total field  $H_{eff}$  experienced by the magnetic moments consist of the external field  $H_0$  and the molecular field  $H_m$  [45]

$$H_{tot} = H_0 + H_m = H_0 + \beta M, \quad (2.1)$$

where  $\beta$  is called the molecular field constant and  $M$  is the magnetization.

Generally, the spin and orbital momenta are coupled and give, in heavy lanthanides, the total angular momentum  $\mathbf{J} = \mathbf{L} + \mathbf{S}$  (where  $\mathbf{L}$  and  $\mathbf{S}$  are orbital and spin angular momenta, respectively). The magnetic moment of an atom with angular momentum  $J$  is given by [46]

$$\mu_J = \mu_B g \mathbf{J}, \quad (2.2)$$

where  $g$  is the so called Landé  $g$ -factor and  $\mu_B$  is the Bohr magneton ( $= \frac{e\hbar}{2m_e} = 5.79 \cdot 10^{-5} \text{ eV/T}$ ).

The energy of a magnetic dipole moment in an external magnetic field is,

$$E = -\mu \cdot \mathbf{H}_0. \quad (2.3)$$

---

<sup>1</sup>The indirect exchange can be further classified depending on the intermediate species. For example, when the latter is a nonmagnetic atom, the exchange interaction is called the super-exchange.

## 2.1 Magnetism and magnetic interactions in lanthanides

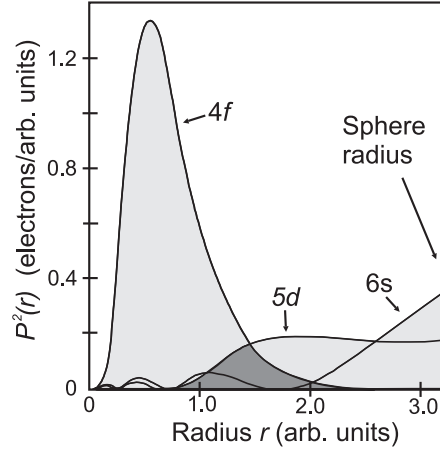


**Figure 2.1:** Radial electronic probability density of Gd for  $4f$ ,  $5d$  and  $6s$  electrons, [47]. The direct overlap of  $4f$  with the nearest one is negligible. The overlapping of  $4f$  and  $5d$  (shaded region) is responsible for the  $4f$ - $5d$  exchange interaction and hence the long-range magnetic ordering.

For a general case with  $n$  the total number of atoms per unit volume, when all magnetic moments are aligned along field direction (at  $T_0=0$ ), the saturation magnetization becomes

$$M_{tot} = ng\mu_B J = \frac{\sum_i \mu_i}{V}. \quad (2.4)$$

At non-zero temperatures the magnetization decreases, as is addressed in the next sections.

### 2.1.1 Indirect exchange interaction

In lanthanide ferromagnets the dominant part of magnetism originates from the  $4f$  magnetic moments which are strongly localized in the ion core. Due to their localized nature, the direct overlap of atomic orbitals is usually very small and is not sufficient to induce the long-range magnetic ordering. As an example the calculated electronic charge densities [47] of the localized and conduction electrons of Gd is shown in figure 2.1. The  $4f$  electronic density vanishes at the  $1.5 \text{ \AA}$  whereas in the basal plane the inter-atomic spacing is  $3.63 \text{ \AA}$  [48, 49]. Therefore, the magnetic ordering of the neighboring moments occurs through indirect interaction. First the overlap of the localized  $4f$  orbitals with  $5d6s$  one (dark shaded region in figure 2.1) results in the spin- depen-

## 2. Fundamentals

---

dent splitting of the electronic band structure which induces a magnetic moment of the conduction electrons. Inter-atomic interaction of these spin-polarized conduction electrons couples the nearest neighbor  $4f$  moments. The indirect exchange or RKKY interaction can be described by the effective Hamiltonian

$$\mathcal{H} = - \sum_{i,j} J_{i,j}(r) \mathbf{S}_i \cdot \mathbf{S}_j, \quad (2.5)$$

where  $\mathbf{S}_i$  and  $\mathbf{S}_j$  are the interacting spins at lattice sites  $i$  and  $j$ . Parameter  $J_{i,j}$  describes the strength of the RKKY exchange interaction [50].

$$J_{i,j}(r) \propto \frac{\cos(2k_F r)}{r^3} \quad (2.6)$$

with  $k_F$  the Fermi radius and  $r$  the distance between the spins. The interaction is long-range and depends on the shape of the Fermi surface; it shows an oscillatory dependence on the distance between the nearest spins. Moreover, the sign of  $J_{i,j}$  defines the parallel or antiparallel (FM/AFM) alignment of the nearest neighbor spins. This can result in a helical or more exotic magnetic ordering in lanthanides [46]. The energy of the intra-atomic exchange interaction between  $4f$  and  $5d$  spins is also an important quantity in the context of this project. The exchange integral for intra-atomic exchange  $J_{4f-5d}$  depends on the  $4f$ - $5d$  overlap. The coupling strength  $J_{4f-5d}$  for an individual  $5d6s$  electron and a  $4f^7$  magnetic moment is estimated to be [51]

$$J_{4f-5d} = 94 - 3.4(x - 1) \text{ meV}, \quad (2.7)$$

where  $x=1, 2$  for Gd and Tb respectively. However, considering interaction of all  $4f$  spins with the conduction electrons give the energy of about 700 meV [52]. In this thesis magnetization dynamics of both  $4f$  and  $5d6s$  electrons is discussed which can give the information about the strength of the exchange interaction.

### 2.1.2 Spin-orbit interaction

Spin-orbit interaction is the interaction of the electron's spin with its orbital motion. The physical origin of this coupling lies in the fact that an electron experiences the time varying electric field of the nucleus while orbiting, which is stationary in lab frame, as depicted in figure 2.2. If  $\mu_s$  is the spin magnetic moment and  $H_{orb}$  the effective magnetic

## 2.1 Magnetism and magnetic interactions in lanthanides

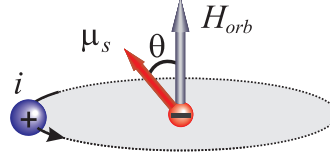


**Figure 2.2:** Spin-orbit coupling originates when the orbiting electron feels the time varying electric field ( $H_{orb}$ ) of the nucleus.

field the electron feels while orbiting around the nucleus, the interaction energy in the atomic picture is [9]:

$$E = -\mu_s \cdot \mathbf{H}_{orb} = -\frac{e^2}{4\pi\epsilon_0 m_e^2 c^2 r^3} \mathbf{L} \cdot \mathbf{S}, \quad (2.8)$$

where  $m_e$ ,  $e$  are the electron mass and charge respectively,  $c$  speed of light,  $r$  is the atomic radius,  $\mathbf{L}$  and  $\mathbf{S}$  are the orbital and spin momentum of the atom.

This interaction couples the electron spins to the crystallographic structure of the materials. The electronic orbitals in the solid state depend on the crystallographic structure. Due to spin-orbit interaction, spin moments follow a preferential direction in the crystal: the easy axis of magnetization. The difference in energy along different directions originating from this effect is called magneto-crystalline anisotropy.

Due to the spherical distribution of the half filled  $4f$  shells, stemming from the half filled  $4f$  orbitals, the direct coupling of  $4f$  to the lattice is absent in Gd (figure 2.4). On the other hand for Tb, a pronounced coupling of the orientation of the atomic magnetic moment to the lattice follows from the non-spherical  $4f$  distribution since spin-orbit interaction couples the direction of the spin moment to the  $4f$  orbital, as depicted in figure 2.4. Indeed, the magnetic anisotropy constant  $K_2$  describing the energy required to rotate magnetization with respect to the basal plane of the hcp lattice is more than two orders of magnitude smaller in Gd than in Tb [46]. The magnetic anisotropy in Gd is, however, non-zero due to the spin-orbit interaction of  $5d$  electrons and the  $4f$ - $5d$  coupling [53]. This conduction electron mediated spin-lattice coupling is referred to as indirect. Note that the spin-orbit coupling is usually weaker than exchange interaction whereas the latter is isotropic.

## 2. Fundamentals

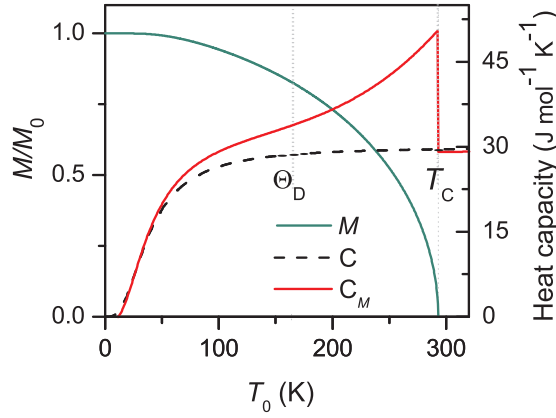


**Figure 2.3:** Temperature-dependent magnetization of Gd calculated using the Brillouin function (green line) with the Curie temperature 293 K. Lattice specific heat calculated from the Debye model ( $C$ , dotted line) [41] and from experimental results with spin contributions ( $C_M$ , red line) [44], with a Debye temperature of 163 K. The heat capacity with magnetic contributions diverges near ferro- to paramagnetic phase transition due to critical spin fluctuations.

### 2.1.3 Magnetic phase transition and critical slowing down

The magnetization of the material stems from the long range order of the magnetic moments through the exchange interaction. With increasing temperature the thermal energy ( $k_B T$ ) of the system increases which disorders the moments while the magnetic exchange interaction tends to align these moments. The competition between these two defines the value of equilibrium magnetization  $M$  at finite temperatures. At a certain temperature when this energy is more than the exchange energy, the long range order of the system breaks. Beyond this temperature the system changes from ordered to disordered state, called the ferro- to paramagnetic phase transition which occurs at the Curie temperature  $T_C$ . For a ferromagnet the second derivative of the free energy, i.e the susceptibility is discontinuous at the Curie temperature. Therefore such a transition is called second order phase transition.

As for ferromagnets we are interested in the spontaneous magnetization at finite temperatures, therefore, the external magnetic field is ignored for the moment. The total magnetic field of eq. 2.1 consists of the molecular field which in term depends on magnetization. Thus the temperature dependence of magnetization can be described by the so called *Brillouin function*  $B_J(x)$  which is calculated using the Boltzmann



## 2.1 Magnetism and magnetic interactions in lanthanides

distribution [50]

$$M = NgJ\mu_B B_J(x), B_J(x) = \frac{2J+1}{2J} \coth\left(\frac{2J+1}{2J}x\right) - \frac{1}{2J} \coth\left(\frac{x}{2J}\right), \quad (2.9)$$

where  $x = gJ\mu_B H_0/k_B T$ , with  $k_B$  the Boltzmann constant and  $H_0 = \lambda M(T)$ .

The temperature dependence of magnetization for Gd, using eq. 2.9 with  $J=7/2$ , is plotted as a function of temperature in figure 2.3 (green line). The magnetization at zero kelvin is equal to  $M_0$  and decreases to zero at the Curie temperature ( $T_C$ ). At low temperatures spin-wave or magnon excitation<sup>1</sup> contribute to magnetization. At higher temperatures close to  $T_C$  critical spin fluctuations lead to a decrease of magnetization. Near the ferro- to paramagnetic phase transition temperature there exists a region where correlation length of the spin fluctuations increases enormously. These fluctuations contribute to the magnetic order parameters such as, magnetization, specific heat [10] and resistivity [46] etc. An example of the lattice specific heat with spin contribution ( $C_M$ ) is shown by the red line in figure 2.3 (for simplicity, contributions above  $T_C$  are ignored). At low temperatures the specific heat increases due to the phonons and effect of the spin fluctuations results in a further increase and divergence of  $C_M$  near the Curie temperature  $T_C$ . The pronounced change in magnetic properties near  $T_C$  is usually attributed to *critical slowing down*. It is well established in the physics of magnetic phase transitions that the correlation length of the spin fluctuations ( $\xi$ ) diverges as the Curie temperature is approached [54].

$$\xi \propto (1 - T_0/T_C)^\nu, \quad (2.10)$$

where  $\nu$  is the critical exponent of the correlation length.

In the critical region the temperature dependence of the magnetic order parameter can be described by a power law with critical exponents. As magnetic properties depend on the critical fluctuations, a relation between the critical exponents of different magnetic parameters can be derived which is called a *scaling law*. The role of the critical fluctuations on the static magnetic properties is already investigated and details can be found for example in the Ref. [55]. Since we will discuss magnetization dynamics,

---

<sup>1</sup>The spin flip spread over large number of magnetic moments is called the magnon.

## 2. Fundamentals

---

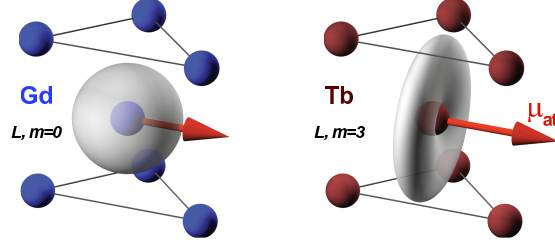


**Figure 2.4:**  $4f$  electron wave-function in a hcp lattice with  $L, m = 0$  and  $3$  for Gd and Tb, respectively. The  $m = 3$  non-spherical distribution of Tb couples to the ion cores via single ion anisotropy, which is absent for the spherical  $m = 0$  state of Gd. From [58].

the relevant order parameter here is the spin fluctuation time  $\tau$  which follows a power law of the form [51, 56]

$$\tau \simeq \tau_0(1 - T_0/T_C)^\omega, \quad (2.11)$$

where  $\omega = \nu \cdot (z - 1.06)$ ;  $\nu$  and  $z$  denote the critical exponents of the correlation length and the dynamical critical exponent, respectively.

### 2.1.4 Electronic structure and magnetic properties of Gd and Tb

Gd and Tb belong to the lanthanides<sup>2</sup>, the materials which follow the successive filling of  $4f$  levels from Ce to Lu. Both materials have a trivalent  $4f^n 5d^1 6s^2$  electronic configuration which results in similar chemical properties of these materials and show the hexagonal closed packed (hcp) crystal structure below the melting point [57]. Elemental Gd and Tb are metals with the conduction band formed by the itinerant  $5d 6s$  electrons.

The magnetization in general originates from spin as well as orbital magnetic moments. The heavy lanthanide Gd ( $4f^7$ ) and Tb ( $4f^8$ ) are well known for their magnetic properties as a function of occupation of the  $4f$  orbital. As the  $4f$  shell is more than half filled, the spin quantum number  $S$  decreases (Gd  $S = 7/2$ , Tb  $S = 6/2$ ) while the orbital quantum number  $L$  increases (Gd  $L = 0$ , Tb  $L = 3$ ) [46]. Magnetic moments of these metals mainly originate from the partially filled  $4f$  levels. Due to their localized nature, the  $4f$  states maintain the atomic-like moment in the condensed phase. As mentioned in the previous section, the magnetic ordering in these metals occurs by

---

<sup>2</sup>Lanthanides are also known as rare earth elements; this name was given because of the difficulty to extract them due to the similarity of their conduction electron configurations.

## 2.1 Magnetism and magnetic interactions in lanthanides

---

indirect interaction through spin polarization of conduction electrons. Therefore, the magnetic moments of the Gd and Tb can be divided into two sub-systems; the localized  $4f$  and induced  $5d6s$  magnetic moment. The total magnetic moment of eq. 2.2 reads

$$\mu_{at} = \mu_{4f} + \mu_{5d6s}. \quad (2.12)$$

The magnetic moment per atom  $\mu_{at}$  follows Hund's rules ( $\mu_{\text{Gd}} = 7.55 \mu_B$ ,  $\mu_{\text{Tb}} = 9.34 \mu_B$  [59]), where the excess from the integer value is attributed to spin polarization of the  $5d6s$  conduction electrons. Although conduction electrons carry a rather small induced magnetic moment, their mediating nature in magnetic ordering plays an important role for magnetic properties. Both the Gd and Tb show ferromagnetic order below room temperature. Gd changes from ferro- directly to para-magnetic phase with the Curie temperature of 293 K [60]. Tb shows in addition, an anti-ferromagnetic phase with helical magnetic structure from 221-229 K before transforming to a paramagnetic state [46]. As indicated in figure 2.4, Gd and Tb are also a special case of the magnetocrystalline anisotropy. With an orbital angular momentum  $L, m = 0$ ,  $m$  is the magnetic quantum number, which results in spherical orbitals with weak interaction with the lattice in Gd. On the other hand, Tb has  $L, m = 3$  with the non-spherical distribution of the electron orbitals, these non-spherical orbitals are attracted by the ion cores of neighboring atoms thus generating a strong anisotropy. In this study, the contrast of spin-orbit coupling in Gd and Tb was used to investigate the role of the spin-orbit interaction in ultrafast magnetization dynamics.

The easy axis of the bulk hcp Gd depends on temperature. At low temperatures easy axis makes  $30^\circ$  angle with the c-axis, this angle increases with temperature and reaches a maximum value of  $65^\circ$  at 170 K. Above this temperatures it continuously turns back towards c-axis and for temperature range between 240 K and  $T_C$  the magnetization aligns along the c-axis [61]. This type of transition is called the magnetic re-orientation transition. However, as a consequence of the strong dipolar anisotropy in thin films this transition can be disregarded for the Gd films below 30 nm thickness where easy axis lies in the basal plane [61, 62]. To avoid such transitions in temperature dependent studies, the film thickness used in this thesis was set to 20 nm. In the ferromagnetic phase below 219 K, Tb moments are aligned along b-axis in the basal plane of hcp structure.

## 2. Fundamentals

---

### 2.2 Laser-induced dynamics

In this section dynamics of electrons, phonons and spin sub-systems following femtosecond laser excitation will be discussed.

The interaction between light and matter takes place through the optical electric field and the conduction electrons of the medium. The intensity of the electromagnetic radiation that passes through a matter of thickness  $d$  can be described according to the Lambert Beer law as

$$I = I_0 e^{-\alpha(\lambda) \cdot d}, \quad (2.13)$$

where  $\alpha(\lambda)$  is a wavelength dependent material specific parameter and is called the absorption coefficient. It is clear from eq. 2.13 that the intensity of the light beam decreases exponentially as it passes through the medium of thickness  $d$ . The *optical penetration depth* or *skin depth* ( $\delta \propto 1/\alpha$ ) describes the distance at which optical light decay by a factor of  $1/e$  in the medium and can be defined as [41]

$$\delta = \frac{\lambda}{4\pi k}, \quad (2.14)$$

where  $\lambda$  is the light wavelength and  $k$  is the imaginary part of the complex refractive index  $n = n' + ik$ . Typical values of the optical penetration depth for metals, for laser wavelengths in the visible spectral range, are 10-30 nm.

#### 2.2.1 Electron dynamics and thermalization

When a metal is excited with the laser pulses of infrared wavelength range ( $\sim 1.5$  eV), the incident electromagnetic field strongly interacts with the conduction electrons generating non-equilibrium electron hole pairs in the material because the much heavier nuclei are not able to follow the high frequencies of visible light. The optical transitions create a broad nonthermal electron distribution that extends from the Fermi energy up to the energy of the incident photons. Up to some finite time the electron oscillations can preserve the memory of the optical phase of the excitation pulse. Dephasing of the coherent electronic distribution occurs due to screening effects which start at sub-femtosecond time at the order of inverse plasma frequency<sup>1</sup> [63]. The electron-electron,

---

<sup>1</sup>The inverse plasma frequency describes the characteristic time the plasma needs to respond to an external perturbation.

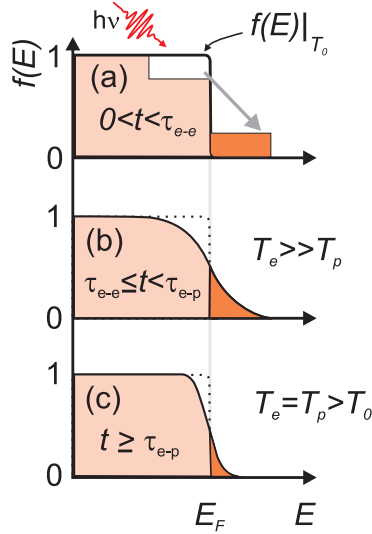


**Figure 2.5:** (a) The equilibrium Fermi-Dirac distribution function  $f(E)$  as a function of energy at temperature  $T_0$  (solid black line). Upon laser excitation the ensemble of electrons has pumped above the fermi level  $E_F$  as shown by the step-like function which cannot be described by the  $f(E)$ . (b) Subsequently, e-e interaction leads to thermalization of electrons with the characteristic time of  $\tau_{e-e}$ ; after this time excited electron gas can be described by the  $f(E)$  and temperature  $T_e$ . (c) The energy is transferred from the electron to the phonon system through e-p scattering and eventually their temperatures equalize at a time of  $\tau_{e-p}$ , with  $T_e = T_l > T_0$ .

electron-phonon or electron-defect scattering of elastic nature can also contribute to the dephasing of electron gas. Note that we consider here only the type of interaction where electrons lose the phase coherence without loss of energy. The optically excited ensemble of incoherent electron-hole pairs do not obey the Fermi-Dirac statistics. The resulting non-Fermi distribution is depicted as a step in figure 2.5(a), sketched with rectangular shape whose dimensions are determined by the energy of the exciting laser pulse  $h\nu$  and the absorbed energy density from the laser. In the low excitation density regime ( $< 10^{-3}e/\text{atom}$ ) the electron dynamics can be described by the single particle interaction where the hot electron interacts with the cold electron below Fermi level. The lifetime of the excited electrons in the vicinity of Fermi energy can be estimated by Fermi-liquid theory (FLT) [64]

$$\tau_{e-e} = \text{Const.} \frac{n^{5/6}}{(E - E_F)^2}, \quad (2.15)$$

which predicts that the life time of the electron depends on the energy above  $E_F$  and the density of electron gas  $n$ . The life time of the electron depends on the number of scattering partners and the available amount of final states for scattering known as *phase space*.

Moreover, an excited electron experiencing an inelastic scattering with another electron will transfer part of its energy to the other electron, generating a cascade of secondary electrons with energies close to Fermi level. Since the specific heat of the

## 2. Fundamentals

---

electron is order of magnitude smaller than the lattice system, electronic temperature evolves to a few 1000 K and then significant energy transfers to the lattice due to electron-phonon coupling.

After this thermalization electron dynamics can be described by the Fermi-Dirac distribution  $f(E)$  with a well-defined electronic temperature  $T_e$ .

$$f(E) = \frac{1}{e^{(E-E_F)/k_B T_e} + 1}, \quad (2.16)$$

where  $k_B$  is the Boltzmann constant and  $E_F$  is the Fermi energy. Figure 2.5 shows the evolution of Fermi-Dirac distribution (FDD) function following fs laser excitation. The non-thermalized electron distribution is shown by the step function, in figure 2.5(a). After thermalization the distribution can be described at higher temperature. The time scale of thermalization of the electron in Gd is about 100 fs as measured by two-photon photoemission [27], depicted in figure 2.7. This will be discussed further in the next section.

### 2.2.2 Phonon dynamics and the two temperature model (2TM)

As the electron heat capacity is typically 1-2 orders of magnitude smaller than that of the lattice, the electronic temperature  $T_e$  increases to several thousand Kelvin within 1 ps while the lattice remains relatively cold [27]. Subsequent to hot electron relaxation, their motion is damped by collisions with the lattice. The collective lattice motions are represented by quasiparticles called phonons.

The energy of hot electrons is used to excite the phonon and the time scale of energy transfer and hence thermalization is defined by electron-phonon coupling. The electron-phonon scattering rate and hence the lifetime can be approximated in the framework of the Debye model [65]:

$$\tau_{e-ph} = \frac{\hbar}{2\pi\lambda k_B T}, \quad (2.17)$$

where  $\lambda$  is the strength of the coupling between the electron and phonon bath and  $k_B$  the Boltzmann constant. In metals, a typical value of  $\tau_{e-ph}$  is of the order of 1 ps.

The electron and phonon temperature ( $T_e$  and  $T_l$ ), following an ultrafast laser excitation, can be evaluated with the so called *two-temperature model*. Figure 2.6 shows the schematic representation of electron and phonon sub-systems of two temperature

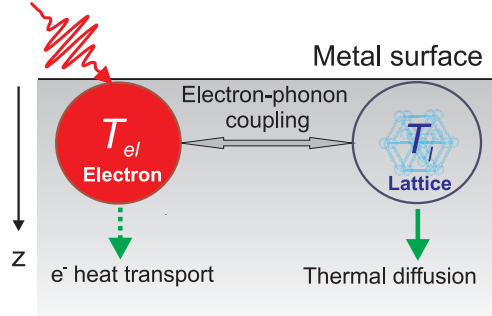


**Figure 2.6:** Schematic of electron and phonon sub-systems as considered in the two temperature model and transfer of energy from electron to the lattice through electron-phonon coupling, transport process and heat diffusion from the surface of metal to bulk and substrate.

model. This model assumes that the electrons and the lattice are in a local thermal equilibrium, and the energy transfer depends on the coupling between electron and phonon and their heat capacities. The dynamics of electron and lattice sub-systems can be described by a set of coupled differential equations given as [41, 66]:

$$C_e(T_e) \frac{\partial T_e}{\partial t} = \frac{\partial}{\partial z} \left( \kappa_e \frac{\partial T_e}{\partial z} \right) - g \cdot (T_e - T_l) + S(z, t), \quad (2.18)$$

$$C_l(T_l) \frac{\partial T_l}{\partial t} = g \cdot (T_e - T_l). \quad (2.19)$$

Here  $C_e$  ( $= \gamma T_e$  with  $\gamma$  is a constant related to the density of the states at the  $E_F$ ) and  $C_l$  denote the electronic and lattice heat capacities, respectively. The first part of equation 2.18 describes the electronic heat transport into the bulk of the sample.  $\kappa_e$  is the thermal conductivity and its temperature dependence can be described by  $\kappa \approx \kappa_0 (T_e/T_l)$  where  $\kappa_0$  can also be a temperature-dependent quantity [67]. With the assumption that the laser beam size is much larger than the electron diffusion length, only the diffusion along the direction of the surface normal is important (z-direction in figure 2.6). The second part of equation 2.18 and equation 2.19 account for the cooling of the electrons and heating of the phonons by the electron-phonon interaction with coupling constant  $g$ . The  $S(z, t)$  is the source term which represents the amount of laser power dissipated in a unit volume from the laser pulse. Following the penetration

## 2. Fundamentals

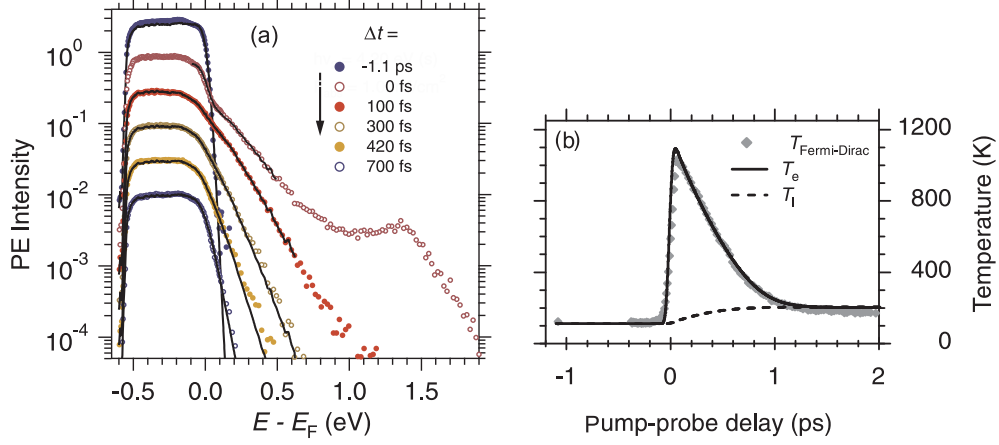


**Figure 2.7:** (a) Experimental time-resolved photo-emission spectra from Gd(0001) for different pump-probe delays. The black lines are fits of Fermi-Dirac distribution function according to a constant DOS. The fits follow the experimental data for all delays except  $\Delta t = 0$  ps, where a nonthermalized distribution is required. (b) Comparison of the experimentally determined electronic temperature ( $T_{\text{Fermi-Dirac}}$  determined from PE results of panel (a), shown by diamonds) and calculated electronic ( $T_e$ ) and lattice ( $T_l$ ) temperatures following femtosecond pulse laser excitation using two temperature model (eqs. 2.18 and 2.19) at equilibrium temperature of 50 K. The parameters used for the calculations are given in table 2.1. Figure from Ref. [27].

depth (eq. 2.13) and finite pulse duration of the laser, the source term is given by [42]

$$S(z, t) = (1 - R - T)I_0\alpha e^{-z\alpha} e^{(-t/\tau_{lp})^2}, \quad (2.20)$$

where  $R$  and  $T$  represent the reflected and transmitted parts of the incident intensity  $I_0$ , respectively, and  $\tau_{lp}$  is the laser pulse duration. The use of exponential decay is only first approximation, reflection from the interface of the sample and substrate can result in the more complex behavior. Following fs laser excitation, the temporal evolution of electron ( $T_e$ ) and lattice ( $T_l$ ) temperature calculated by two temperature model is shown in figure 2.7(b). The values of the parameters used for 2TM calculations are given in table 2.1. The electrons are excited to about 1100 K by the laser and then equilibrate with the lattice system within few ps.

Figure 2.7 shows the photo-emission intensity as a function of energy for 10 nm Gd(0001)/W(110) on different time delays and lines representing the equilibrium Fermi-Dirac distribution function (FDDF). It is clear that the dynamics after 100 fs can be described by fits however at earlier time scales experimental results deviate from FDDF.



## 2.2 Laser-induced dynamics

**Table 2.1:** Physical constants used in the current project, the values are from Ref. [69] unless specified.

Quantity	Symbol	Gd	Tb	units
Mass density	$\rho$	7890	8270	$Kg\ m^{-3}$
Lattice constants	$a, c$	3.63, 5.78	3.60, 5.70	$\text{\AA}$
Electron heat capacity	$\gamma_e$	225.12		$Jm^{-3}K^{-2}$
Electron-phonon coupling const.	$g_{e-l}$	$2.4 \times 10^{17}$		$Wm^{-3}K^{-1}$
Debye temperature	$\Theta_D$	163	144 [70]	$K$
Maximum phonon energy	$\hbar\omega_p$	14	13.4 [70]	$meV$
Speed of sound	$v_s$	2950	2920	$m\ s^{-1}$
Thermal conductivity	$\kappa_0$	8-11( $T_0$ )	11.1	$Wm^{-1}K^{-1}$
Optical penetration depth	$\delta$	20-50	20-50 [41]	$nm$
Magnetic moment	$\mu$	7.55	9.34 [59]	$\mu_B$
Curie temperature	$T_C$	293	220 ( $T_N = 229K$ )	$K$
Magnetocryst. anisotropy energy	$E_{MAE}$	0.032	10 [46, 71]	$meV$

The two temperature model, discussed above, is an oversimplification of the dynamics at the ultrafast time scale when the electron system is not thermally equilibrated. To overcome this drawback one can employ a more extended variant of the 2TM that accounts for the non-equilibrated electron distribution [68]. As shown in right panel of figure 2.7, for Gd two temperature model gives good estimation of electronic temperature which agrees with the experimentally determined temperature  $T_{\text{Fermi-Dirac}}$  determined from photo-emission results of figure 2.7(a). This allow us to use the two temperature model for the description of electron dynamics and comparison with our experimental results.

It is important to mention that with increasing temperature one expects the increase in the electron-phonon energy equilibration time due to: lattice specific heat at low temperatures and electronic specific heat at temperatures higher than the Debye temperatures [68].

### Heat diffusion and recovery

The temperature gradient generated by the optical skin depth generates transport effects that dissipate the energy out of the excited region. The transport effects are competing with electron-electron and electron-phonon scattering processes that redistribute the photo-induced energy within the excited region. The energy can be rapidly

## 2. Fundamentals

---

distributed to unexcited regions of the sample on the time scale which is defined by the Fermi velocity  $v_f \approx 10^6 \text{m/s}$  [72] of electron ( $\tau_d \approx d/v_f^2$ ), this is called the ballistic transport. Second mechanism of energy redistribution of the hot electron bath is known as the electron diffusion process. Efficiency of this process is determined by the electron-phonon coupling and temperature gradient in the sample ( $\tau_d \approx C_e d^2 / 2k_e$  [68]). Typical time scales of both diffusive and ballistic transport processes are well below 100 fs for metals [68, 73, 74]. The electronic heat transport processes are represented by dotted line in figure 2.6.

The gradient of temperature also results into flux of heat from the sample to substrate. The classical heat diffusion equation can be used to describe the flux of heat [42].

$$K \cdot \nabla^2 T + C \cdot \frac{\partial T}{\partial t} = \frac{\partial U}{\partial t}, \quad (2.21)$$

with  $K$  thermal conductivity,  $U$  the heat per unit volume and  $C$  the heat capacity per unit volume. Intrinsically both of the electron ballistic transport and diffusion process are faster than the heat diffusion. The sample cools back to initial temperature from nano- to micro-second time scale due to heat diffusion.

### 2.2.3 Spin dynamics

As discussed in the previous sections, femtosecond laser excitation produces a strongly non-equilibrium ensemble of electrons which thermalizes to Fermi-Dirac distribution by electron-electron scattering. After internal thermalization, energy flows to the lattice system by electron-phonon coupling. How fast and by which mechanism spins of a system react to the dynamics of the electron and lattice system has always remained a quest for the understanding of ultrafast magnetization dynamics. A considerable decrease in the magnetization within a few hundred femtoseconds following laser excitation has been observed almost two decades ago [13], but the mechanism of this decrease in magnetization is still under discussion.

The important feature of spin dynamics is the angular momentum conservation. When spin dynamics is considered, the angular momentum of the isolated system must be conserved in addition to the energy. In the context of ultrafast spin dynamics, the parts of the enclosed system are photon, electron, spin and lattice. Their respective

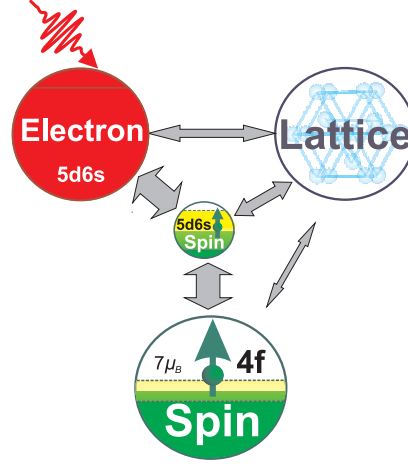


**Figure 2.8:** The exchange of energy and angular momentum among the electron, phonon and spin sub-systems following the optical excitation of the conduction electron. In the lanthanides the spin system can be divided into two sub-systems, localized  $4f$  and itinerant  $5d$ . With optical light only electrons and hence spins from the  $5d$  system are excited, which play the role of mediator for the ferromagnetic ordering.

angular momentum conservation [75, 76] regarding its application to the lanthanide ferromagnets reads

$$\Delta \mathbf{J}_{total} = \Delta \mathbf{L}_{photon} + \Delta \mathbf{L}_{lattice} + \Delta \mathbf{L}_{electron} + \Delta \mathbf{S}_{4f} + \Delta \mathbf{S}_{5d} = 0, \quad (2.22)$$

where  $\mathbf{L}_{photon}$ ,  $\mathbf{L}_{lattice}$ ,  $\mathbf{L}_{electron}$  and  $\mathbf{S}$  represent the photon, lattice, electron orbital, and spin angular momenta, respectively. In the lanthanide materials the spin system consists of two components, the  $4f$  and  $5d$  magnetic moments; and their angular momentum reads  $\mathbf{S}_{4f}$  and  $\mathbf{S}_{5d}$ , respectively. The different systems contributing to sharing of energy and angular momentum are shown schematically in figure 2.8. As a consequence of the angular momentum conservation, any change in the magnetization must be compensated by the change in the angular momentum of the other system, the *reservoir* or *bath*. As reported in Ref. [6] the time scale for transfer of the angular momentum to the lattice, for ferromagnetic Gd, is of the order of 100 ps due to weak  $4f$  spin-orbit coupling. The direct transfer of angular momentum from photons to the spin system, in itinerant ferromagnets, was reported to be too small to reproduce the experimentally observed demagnetization and was excluded as a source of demagne-

## 2. Fundamentals

---

tization at ultrafast time scale [17, 75]. If similar conditions are considered for the lanthanide ferromagnet Gd, one does not expect strong change in magnetization at ultrafast time scale. Therefore, it is important to investigate whether there exists any ultrafast demagnetization in Gd and if so, what the time scale of this demagnetization is and how it is different from the well-studied itinerant ferromagnets. In context of this thesis, sharing of angular momentum between localized  $4f$  and itinerant  $5d6s$  magnetic moments is also addressed in addition to the lattice.

It is also important to understand the photon-, electron-, and phonon-mediated effects on the magnetization under nonequilibrium conditions after femtosecond laser excitation. Some of the mechanisms that have been proposed over the past several years, being responsible for the transfer of angular momentum and hence demagnetization, will be discussed in the following.

### (i) Spin-lattice relaxation

For demagnetization following laser excitation, the most important candidate as a reservoir of the angular momentum is the lattice and the primary mechanism responsible for this is the spin-lattice relaxation which is mediated by the spin-orbit coupling. The spin-lattice relaxation time  $\tau_{SL}$  describes the time required by the spins to reach thermal equilibrium with the lattice. To explain the pioneering work of time-dependent evaluation of magnetization in Gd by Vaterlaus et al. [6], Hübner and Bennemann [33] proposed the mechanism of the spin-lattice relaxation. There are possibilities of different processes, depending on the temperature as discussed in Ref. [33], the direct process, the indirect process and the Raman process. At intermediate temperatures the most important one is Raman process. In this process a phonon of frequency  $k$  is absorbed and a phonon of frequency  $q$  is emitted with emission of a magnon (spin-flip) of frequency ( $\Omega$ ), as shown schematically in figure 2.9.

Considering this process Hübner et al. derived a relation between spin-lattice relaxation time and anisotropy energy [33]

$$\tau_{S-L}^{-1} = \frac{9|E_{anis}|^2}{8\rho^2\pi^3\hbar^7v_s^{10}} \int_0^{k_B\Theta_D} n_k(n_k + 1)E^6 dE, \quad (2.23)$$

where  $n_k$  is the thermal occupation of the phonons and is calculated from the Bose-Einstein distribution ( $n_k = \{e^{(E/k_B T)} - 1\}^{-1}$ ) in the framework of Debye model with

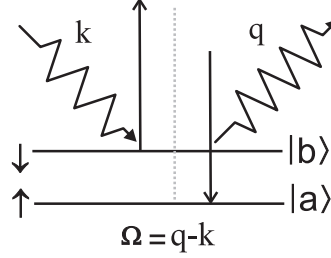


**Figure 2.9:** Raman process of spin-lattice relaxation. The process consists of the absorption of a phonon of frequency  $k$  and emission of a phonon of frequency  $q$  accompanied by a magnon. From Ref. [33].

$v_s$  is the speed of sound and  $\rho$  is the mass density of the material. The first term in equation 2.23 represents the anisotropy energy and second term represents the phonon occupation. The competition between these two terms will define the temperature dependence of  $\tau_{S-L}$ .

For a typical value of the anisotropy energy (for ferromagnetic Gd) of  $735\mu\text{eV}$ , the theory suggested  $\tau_{S-L} = 48\text{ps}$ ; reproducing the experimental value of  $\tau_{S-L} = 100 \pm 80\text{ps}$  available at that time. It is still an open question whether this prediction explains the dynamics at ultrafast time scale following fs laser excitation.

### (ii) $d$ - $f$ ( $sp$ - $d$ ) exchange mediated spin flip scattering

The  $sp$ - $d$  interaction was first time introduced by Zener [77] and Vonsovskii [78] for transition metals. Recently ultrafast demagnetization dynamics of magnetic semiconductors was discussed on the basis of  $sp$ - $d$  interaction [79, 80, 81]. In this interaction first the localized spins of the magnetic impurity interact with the charge carriers in the conduction band and then the direct exchange between conduction electrons result in the long range magnetic order. The  $sp$ - $d$  Hamiltonian [82]  $\mathcal{H} \sim \beta S \cdot s$  couples the localized  $S$  and delocalized  $s$  spins. In this model the rate of change of the average spin polarization of conduction electrons can be described as [80, 81]

$$\frac{d}{dt}\langle s(t) \rangle = -\frac{n_i}{n_c} \frac{d}{dt}\langle S(t) \rangle - \frac{\langle s(t) \rangle - s_0(M, T_e)}{\tau_{sr}}, \quad (2.24)$$

where  $M = -n_i J \langle S_z \rangle$ . The dynamics of spin polarization is determined by two processes: transfer of momentum from the localized spin  $S$  occurs during the characteristic

## 2. Fundamentals

---

demagnetization time  $\tau_M$  and the spin relaxation of conduction electrons to the lattice characterized by time  $\tau_{sr}$ . Due to spin-orbit coupling and strong non-equilibrium state of the system, following fs laser excitation where scattering rates are increased, the  $\tau_{sr}$  is suggested to  $\leq 100$  fs [80]. The physical basis of the demagnetization is suggested to be the [80, 81] *inverse Overhauser effect* in which the excited carriers become dynamically spin polarized at the cost of the localized spins.

Since lanthanide materials also have localized magnetic moments which generate magnetic ordering through the spin polarization of the conduction ( $5d6s$ ) electrons, therefore, this mechanism was believed to be valid also for lanthanide ferromagnets. Our experimental results are compared with one based on this mechanism, as will be discussed in chapters 6.

### (iii) Other mechanisms

There are number of other mechanisms which are proposed to contribute in magnetization dynamics which are briefly summarized here.

The Elliott-Yafet type of scattering, first time proposed by Elliott [83] and Yafet [84], is one of the mechanisms responsible for spin flip and hence demagnetization. The elementary process in this mechanism is the scattering of an electron from a phonon in the presence of spin-orbit coupling. Because of the spin-orbit coupling, the electronic eigenstate in a solid is always a mixture of the spin up  $|\uparrow\rangle$  and spin down  $|\downarrow\rangle$  states [85]

$$\psi_k^\uparrow = \{a_k^\uparrow(r)|\uparrow\rangle + b_k^\downarrow(r)|\downarrow\rangle\}e^{ikr}, \quad (2.25)$$

where  $k$  is the wave vector. After each scattering event the probability to find the electron in one of the spin states  $|\uparrow\rangle$  or  $|\downarrow\rangle$  changes, thus transferring the angular momentum from the electron system to the lattice, as depicted in 2.10(a). In eq. 2.25,  $b_k$  (with  $b_k \ll a_k$ ) is the spin-mixing parameter which is proportional to the strength of spin-orbit coupling ( $\sim E_{S-O}/E_{exchange}$ ). If  $p_k^s$  is the probability to find an electron in the spin state  $s$ , then the spin mixing parameter can be defined as  $b_k^2 = \min(p_k^\uparrow, p_k^\downarrow)$ . This microscopic parameter is believed to be related with the macroscopic spin relaxation and hence demagnetization after laser excitation [37, 85]. The calculated values

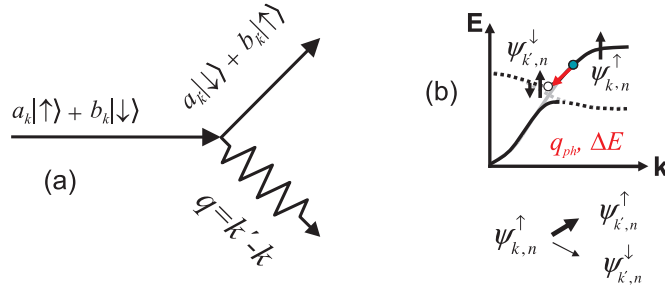


**Figure 2.10:** (a) Elliott-Yafet spin flip scattering mechanism. (b) Spin-flip process from hotspot in electronic band structure, from Ref [29].

of  $b_k^2$  are of the same order of magnitude for Gd 0.059 (0.062) and for Ni 0.025(0.045) corresponding to a thermal (optical) energy of 25 meV (1.4 eV) [85].

In addition to the phonon mediated spin flip, another possibility of the spin flip is discussed as being of electronic origin. Due to spin-orbit interaction there exist some points in Brillouin zone where the states are completely spin mixed, a so-called *spin hotspots* [29] as shown in figure 2.10(b). When the electron scatters from such a hot spot, there is finite probability that the spin will flip. Note that this mechanism may be faster than the phonon-mediated spin flip.

To describe the time scale of laser-induced demagnetization, Koopmans et al. [34, 39] suggested that the demagnetization can be explained considering the Elliott-Yafet spin flip mechanism. Using the Landau-Lifshitz-Gilbert equation the authors derived an analytical expression which connects the demagnetization time with the Gilbert damping parameter. However, this mechanism was challenged in a number of studies [29, 38].

Another mechanism which can lead to the transfer of the magnetic moment out of the region of investigation is the spin transport. In an attempt to explain the demagnetization, Battiatto et al. [26] proposed a mechanism of transport of the excited spins with Fermi velocity, of the order 1nm/fs, from the surface of the metals to the bulk following femtosecond laser excitation. This is known as superdiffusive spin transport. It was suggested that different life time and mean free path of the excited majority and minority electrons can lead to depletion of majority electrons and hence reduction of magnetization. The difference in the propagation of the excited charge carriers depending on their spin character was recently confirmed experimentally [86] but it

## 2. Fundamentals

---

is still not ascertained to what quantitative extent spin transport can affect the total magnetization.

In addition to the processes discussed above, there are some other mechanisms discussed in the literature to affect the magnetization at ultrafast time scale. Which includes for example the coherent interaction of the light with the spins. Recently Bigot et al. suggested that the magnetic state of the system can be directly coupled to the incident light field, provided that the intensity of the light is large [24].

Although these mechanisms contribute to the demagnetization to some extent depending on the excitation conditions and the excited system, there is no clear understanding which mechanism can contribute to what extent and no general agreement has yet been established. Gd is a model Heisenberg ferromagnet with the dominant part of the magnetic moment  $7 \mu_B$  originating from the localized  $4f$  shells. Magnetic ordering occurs through the spin polarization of  $5d$  electrons. Due to half filled  $4f$  shells, the orbital moment of Gd is zero, which leads to a weak  $4f$  spin-lattice coupling. Consequently, demagnetization time for Gd is longer than the electron lattice equilibration time [6, 33], this slow relaxation process can facilitate the disentangling of different contributions to ultrafast demagnetization which is a challenge in the well studied itinerant ferromagnets. As the spin flip scattering takes place in the conduction band of Gd, whereas the major part of the magnetism is localized. Therefore, the investigation of the dynamics of localized  $4f$  as well as non-localized moments and finally their comparison can give further insight into the fundamental mechanism of angular momentum transfer which is also target of this thesis.

In recent years, based on some of the above mentioned mechanisms, some theoretical approaches have been made to couple the dynamics of spin system with the electron and phonon dynamics which are reported in the following.

### 2.3 Theoretical explanation of ultrafast magnetization dynamics

#### 2.3.1 Three temperature model (3TM)

In addition to the two temperature model for the electron and phonon dynamics, with regards to the ferromagnets, a similar approach was employed to describe the spin



## 2.3 Theoretical explanation of ultrafast magnetization dynamics

dynamics [13]. In ferromagnets one can also take explicitly into account the spin thermodynamics and incorporate into 2TM equations (2.18 and 2.19) a spin temperature  $T_s$  in a similar way as the electron and lattice temperatures, resulting thus in the so called *three temperature model* (3TM)<sup>1</sup>,

$$C_s(T_s) \frac{\partial T_s}{\partial t} = g_{e-s} \cdot (T_e - T_s) - g_{l-s} \cdot (T_l - T_s), \quad (2.26)$$

where  $C_s$ ,  $g_{e-s}$  and  $g_{l-s}$  are the spin specific heat, electron-spin coupling and lattice-spin coupling constants, respectively. The major weakness of the 3TM lies in the fact that the conservation of angular momentum is not considered explicitly in this model.

### 2.3.2 Microscopic three temperature model (M3TM)

As discussed in the previous section, the conservation of angular momentum is important ingredient of ultrafast demagnetization. In order to explain the ultrafast magnetization dynamics, Koopmans et al [37] recently suggested a phenomenological model which is based on the ElliottYafet-like spin flip scattering to account the angular momentum conservation. This allows us to relate the microscopic spin-flip process with the macroscopic demagnetization. In combination with the so called 2TM for the dynamics of electron and phonon systems (Eq. 2.18, 2.19), a simple expression for the spin dynamics was derived starting from the Boltzmann rate equations for the electron, phonon and spin systems in combination with the Fermi golden rule. In this model the rate of change of magnetization  $\dot{m} = dm/dt$  is described as [37]

$$\dot{m} = Rm \frac{T_l}{T_C} \left\{ 1 - m \coth \left( \frac{mT_C}{T_e} \right) \right\}, \quad (2.27)$$

where  $m = M/M_s$  is the normalized magnetic moment at finite temperature and  $T_C$  is the Curie temperature of the ferromagnet. Coupling to the phonons and electrons is considered through their temperatures  $T_l$  and  $T_e$ , respectively. In equation 2.27,  $R$  is a material specific scaling factor and contains several microscopic material constants

$$R = \frac{8a_{sf}g_{ep}k_B T_C^2 V_{at}}{(\mu_{at}/\mu_B)E_D^2} \quad (2.28)$$

<sup>1</sup>For instance only one equation is presented here, the other two equations can be written in a similar way as 2TM (equations 2.18 and 2.19) by including the spin specific heat and coupling to spin, details can be found in Ref. [13].

## 2. Fundamentals

---

with  $\mu_{at}$  the average magnetic moment per atom in units of  $\mu_B$ ,  $V_{at}$  the atomic volume and  $E_D$  the maximum phonon energy corresponding to Debye temperature with a spin-flip probability  $a_{sf}$  for electron-phonon momentum scattering events. The spin-scattering mechanisms are described by a single dimensionless spin-flip parameter  $a_{sf}$  that can be derived directly from experimental data. According to this model the magnetic materials can be classified into two distinct types depending on their magnetic properties. The ratio  $T_C/\mu_{at}$  defines the figure of merit which separates the two types of magnetization dynamics. The first one, showing relatively faster demagnetization called type-I (e.g. Ni, Co) and the second follow the slower dynamics showing two step demagnetization categorized as type-II. Gd lies with the type II materials. The comparison of the experimental results with the M3TM calculations will be presented in this thesis.

### 2.3.3 Landau-Lifshitz-Bloch (LLB) equation

In recent years another theoretical approach based on the extended Landau-Lifshitz-Gilbert (LLG) equation exhibited the potential to describe ultrafast magnetization dynamics [34, 36, 87]. The LLG is a classical equation which consists of the precession and damping of a spin. According to LLG equation, the rate of change of magnetization  $\dot{m} = dm/dt$  can be described by [50]

$$\dot{m} = \gamma[-m \times H_{eff} + \alpha m \times \dot{m}], \quad (2.29)$$

where  $m = M/M_s(T = 0)$ ,  $\alpha$  is the damping parameter and  $\gamma$  is the electron gyromagnetic ratio. The first term in equation 2.29 represents the precession while the second damping of magnetization. LLG equation is valid for small damping. This equation describes the magnetization dynamics and precession which occurs up to the order of nanosecond time scale. Since at the ultrafast time scale the excited electrons cause spin-dependent changes of the populations, the magnetization dynamics in ferromagnets involves in general a change of the magnitude of the magnetic moments which is not incorporated in the LLG model. This discrepancy was addressed in the Landau-Lifshitz-Bloch (LLB) model [88], where the damping parameter, which is related with the demagnetization time, can be divided into two components: longitudinal and transverse as depicted in figure 2.11. The longitudinal damping parameter can be used to

### 2.3 Theoretical explanation of ultrafast magnetization dynamics

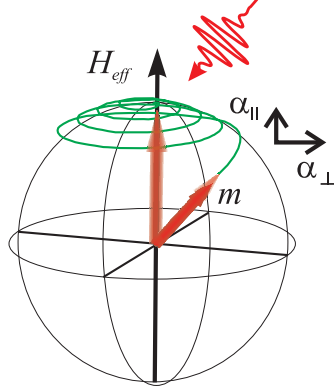


**Figure 2.11:** Landau-Lifshitz-Bloch model where the dimensionless damping parameter  $\alpha$  is divided into longitudinal and transverse components  $\alpha_{\parallel}$  and  $\alpha_{\perp}$ , for  $T < T_C$ .

describe the ultrafast demagnetization. The macroscopic equation for the magnetization dynamics is written in the following form [36, 88]

$$\frac{\dot{m}}{\gamma} = m \times H_{eff} + \frac{\alpha_{\parallel}}{m^2} \{m \cdot H_{eff}\} m - \frac{\alpha_{\perp}}{m^2} [m \times \{m \times H_{eff}\}]. \quad (2.30)$$

The longitudinal damping parameter is [36]

$$\alpha_{\parallel} = \frac{4\lambda T q_S}{3T_C \sinh(2q_S)}. \quad (2.31)$$

In equation 2.31,  $\lambda$  is the important parameter which accounts for the coupling strength of the spin system with the reservoir or bath. The coupling parameter  $\lambda$  contains the matrix elements representing the scattering events which are proportional to the spin-flip rate due to the interaction with the environment (bath).  $q_S = 3T_C m / [2(S + 1)T]$ , where  $S$  is the spin quantum number and  $m$  is the equilibrium magnetization at finite temperature  $T$ . The effective field  $H_{eff}$ , contains all usual micromagnetic contributions, denoted by  $H_m$  (Zeeman, anisotropy and magnetostatic) and exchange term which is given by [88]

$$H_{eff} = H_m + \frac{m}{2\tilde{\chi}_{\parallel}} (1 - m^2) m. \quad (2.32)$$

In this model the temperature-dependent equilibrium magnetization  $m$  and longitudinal susceptibility  $\tilde{\chi}_{\parallel}$  were determined from mean field approximation by using the Curie temperature from the experiments.

## 2. Fundamentals

---

Using a combination of the 2TM (Eq. 2.18, 2.19) and LLB equations, sub-picosecond to picosecond demagnetization as well as the recovery of magnetization and nanosecond magnetization precession was qualitatively described, see Ref. [36]. The coupling parameter described above can also be a temperature-dependent quantity which is not discussed so far and is addressed in chapter 6.

Since the M3TM and LLB models were first presented when our study was already underway, our experimental results can be considered as a test case for the validation of these models. This will be further discussed in chapters 4-6.

### 2.4 Magneto-optical techniques as a probe of magnetization dynamics

The understanding of spin dynamics in ferromagnets is widely based on radio frequency spectroscopy [89] and inelastic scattering techniques employing photons [90] or neutrons [91]. These experimental methods provide frequencies and decay rates of magnetic excitations by the line position and line width, respectively. More recently time domain (pump-probe) techniques that employ short laser pulses have been established in a considerable number of laboratories and provide a complementary approach to analyze spin dynamics [92, 93, 94]. The photo emission techniques can also be used for the study of magnetization dynamics, magneto-optical techniques have advantages over the latter one including greater penetration depth and applicability to measure in applied magnetic fields. Owing to their advantage to probe real time dynamics, magneto-optical techniques are used in this project. Therefore, in the following, the fundamentals of linear, non-linear and x-ray magneto-optical effects are discussed briefly.

The wave equation describes the propagation of electromagnetic waves through a medium, derived from Maxwell's equation [95, 96]

$$\nabla \times \nabla \times \mathbf{E}(\mathbf{r}, t) + \frac{1}{c^2} \frac{\partial^2 \mathbf{E}(\mathbf{r}, t)}{\partial t^2} = -\frac{1}{\epsilon_0 c^2} \frac{\partial^2 \mathbf{P}(\mathbf{r}, t)}{\partial t^2}. \quad (2.33)$$

Here,  $\mathbf{P}$  is the polarization induced in the material, defined as the average dipole moment per unit volume,  $c$  is speed of light in vacuum,  $\epsilon_0$  is permittivity of the vacuum. The light can interact with the matter in two different ways: firstly, there can be a real transition of atoms or molecules from one quantum state to another corresponding to the resonance interaction; and secondly, the induced dipole moment due to optical field

## 2.4 Magneto-optical techniques as a probe of magnetization dynamics

---

which results in polarization of material. The electric polarization acts as a source term in eq. 2.33 and describes the response of the medium to the electromagnetic wave. The polarization is a non-linear function of the electric field and can be expanded in higher order terms using Taylor's expansion as

$$\mathbf{P}(\mathbf{r}, t) = \mathbf{P}^1 + \mathbf{P}^2 + \mathbf{P}^3 + \dots = \mathbf{P}^L + \mathbf{P}^{NL}, \quad (2.34)$$

where  $\mathbf{P}^L$ ,  $\mathbf{P}^{NL}$  are linear and nonlinear optical polarizations, respectively. The first term in eq. 2.34,  $\mathbf{P}^L = \epsilon_0 \chi^{(1)} \mathbf{E}$  (where  $\chi^{(1)}$  is the first order optical susceptibility), is linear in the electric field, the remaining non-linear terms represent the second and higher order optical effects which are important for higher light intensities.

The susceptibility  $\chi^{(i)}$ , which represents the response of a material to an electromagnetic field contains all the information about the optical properties of the macroscopic medium and describes processes like dispersion, reflection, absorption etc. It is related with the permittivity  $\epsilon$  and an index of the refraction of a material. For instance ignoring the nonlinear and nonlocal effects, the optical response can be defined by the dielectric tensor [92]

$$\chi_{ij} = \frac{1}{4\pi} (\epsilon_{ij} - \delta_{ij}). \quad (2.35)$$

Since  $\epsilon$  connects the different components of the electric field vector with the components of induced polarization, it is considered a tensor; which can be represented as [96]

$$\epsilon_{ij}^{(1)} = \begin{pmatrix} \epsilon_{xx}^{(1)} & \epsilon_{xy}^{(1)} & \epsilon_{xz}^{(1)} \\ \epsilon_{yx}^{(1)} & \epsilon_{yy}^{(1)} & \epsilon_{yz}^{(1)} \\ \epsilon_{zx}^{(1)} & \epsilon_{zy}^{(1)} & \epsilon_{zz}^{(1)} \end{pmatrix}. \quad (2.36)$$

The number of the tensor components, which are non-zero, depends (for a specific order of polarization) on symmetry of the system. For an isotropic system the off-diagonal components of the tensor are zero. For magnetic materials the off-diagonal components of this tensor depend on the magnetization. These fulfill the Onsager identity [97] which describes that in the presence of magnetization  $M$  the time reversal symmetry is broken i.e.  $\epsilon_{ij}(-M) = -\epsilon_{ij}(M)$ . These off-diagonal components make the optical probes sensitive to the magnetic state of the system.

## 2. Fundamentals

---

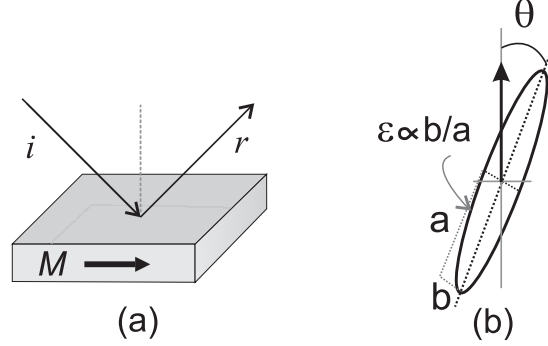


**Figure 2.12:** (a) Magneto-optical Kerr effect in longitudinal configuration. (b) Two types of effects on the polarization of light after reflection from magnetic material, rotation ( $\theta$ ) of plane of polarization and ellipticity ( $\epsilon$ ).

### 2.4.1 Magneto-optical Kerr effect (MOKE)

The change in the state of polarization of light after reflection from a magnetized material is called magneto-optical Kerr effect. In transmission, this is called Faraday effect. In both cases, the change in the state of the light is proportional to the strength of the magnetization. Generally, the MOKE is measured in three different geometries depending upon the orientation of the magnetization with respect to the incident light: (a) transverse when magnetization is in the surface plane of the film and perpendicular to light propagation direction, (b) longitudinal when magnetization is aligned in plane of the film and along the light propagation direction (as depicted in figure 2.12(a)) and (c) polar configuration when magnetization is normal to the surface of the film. In this project, longitudinal geometry was used as shown in figure 2.12 and is discussed in detail in the following.

The relation between the magneto-optical Kerr effect and the dielectric constant can be phenomenologically described by using the classical electrodynamics. For an isotropic magnetic material with magnetization  $M$  in the plane of the sample, if y-axis is considered to be parallel to both the propagation of light and magnetization (figure 2.12), the dielectric tensor  $\epsilon$  that describes the optical response of the medium can be represented as [95, 96, 98]

$$\epsilon(\omega) = \begin{pmatrix} \epsilon_{xx} & 0 & \epsilon_{xz} \\ 0 & \epsilon_{xx} & 0 \\ -\epsilon_{xz} & 0 & \epsilon_{xx} \end{pmatrix}, \quad (2.37)$$

## 2.4 Magneto-optical techniques as a probe of magnetization dynamics

where  $\epsilon$  is a complex quantity. In the presence of magnetization the medium becomes optically anisotropic, the effects induced by the presence of magnetization being described by the off-diagonal tensor components.

From the solution of the electromagnetic wave equation (eq. 2.33) one can get [98]:

(i) The eigenvectors

$$E^\pm(\omega) = E^\pm e^{i\omega[t - (1/c)n_\pm \cdot r]}, \quad (2.38)$$

which represent a circular polarized light with  $\pm$  used for left and right circular polarization.

(ii) The eigenvalues

$$n_\pm^2 = \epsilon_{xx} \pm i\epsilon_{xz} \sin \theta_t, \quad (2.39)$$

where  $\theta_t$  is angle of refraction in the medium. It is clear from the equations 2.38 and 2.39 that the refractive index of the medium is different for left and right circular polarized light. As a linearly polarized light can be considered as two circular polarized components with equal magnitude and opposite helicity, after reflection from the surface the state of the polarization will change due to the difference of response of material to left and right components of light. After reflection (figure 2.12), the plane of polarization of the light will be rotated because of the phase difference introduced between the two circular components of linearly polarized light. In addition, the output light will be elliptically polarized because the circular components will no longer have equal magnitude due to different absorptions for left and right circular polarization, the resulting effect on polarization is depicted in figure 2.12(b).

Using the Fresnel formula, that relates incident and reflected electric fields, and Snell's law one can derive the expression for the complex magneto-optical effect. The magneto-optical effect on the polarization for the longitudinal geometry with incident angle of light of  $45^\circ$  can be written in terms of tensor components as [98, 99],

$$\Theta = \theta + i\varepsilon \cong \frac{\epsilon_{xz}}{(1 - \epsilon_{xx})\sqrt{\epsilon_{xx}(\epsilon_{xx} - 1/2)}}. \quad (2.40)$$

$\Theta = \theta + i\varepsilon$  is the complex magneto-optical Kerr effect with  $\theta$  the rotation, while  $\varepsilon$  is the ellipticity in the polarization after reflection from the magnetic surface. As the magnetization dependent off-diagonal element  $\epsilon_{xz}$  determines the complex Kerr effect, the latter will change if the magnetization is altered. Moreover, the rotation

## 2. Fundamentals

---

and ellipticity also contain diagonal elements which have non-magnetic origin. The non-magnetic contributions need to be minimized to have good magnetic sensitivity.

### Limitations of MOKE as a probe of ultrafast magnetization

In general, the magneto-optical Kerr effect is proportional to the magnetization in equilibrium conditions. However, after fs laser excitation when the system is in a strong nonequilibrium state, the MOKE signal may not be attributed directly to the magnetization [17, 18, 19]. It was suggested that the transient MOKE signal following femtosecond laser excitation can be affected by both magnetic and non-magnetic contributions, therefore the pump-induced change in the MOKE response can be expressed as [92]

$$\Delta\Theta(t) = \Delta G(t) + M_0\Delta F(t) + F_0\Delta M(t), \quad (2.41)$$

where  $G$  and  $F$  are effective Fresnel coefficients and ' $_0$ ' represent the equilibrium values before pump-excitation. In a specific case when the non-magnetic contributions are time independent i.e  $F(t) = F_0$  and  $G(t) = G_0$ , one can show direct relation between transient MOKE rotation and ellipticity as

$$\frac{\Delta\theta(t)}{\theta_0} = \frac{\Delta\varepsilon(t)}{\varepsilon_0} = \frac{\Delta M(t)}{M_0}. \quad (2.42)$$

According to the above relation if a difference in MOKE rotation and ellipticity exists as a result of non-vanishing transient Fresnel coefficients, the magneto-optical signal cannot be directly related with the magnetization. The situation becomes more complex when the non-magnetic contributions also depend on time. The most important time-dependent contributions are the *state filling* or *bleaching* effects when both pump and probe have the same frequency [92]. Directly after fs laser excitation empty states (and electrons) above (below) the Fermi level are filled (removed) which lower the available transition probability for probe photons propagating through the material, as a result the magneto-optical response changes. For temperature-dependent measurements it needs additional care due to some contributions from the temperature dependence of magnetization and specific heats of electrons and phonons. The temporal limitations of the MOKE as a probe of magnetization dynamics in lanthanides is also addressed in this project and will be discussed in the chapter 6. To exclude the non-magnetic contributions, study of the magnetization dynamics in this project was started by



## 2.4 Magneto-optical techniques as a probe of magnetization dynamics

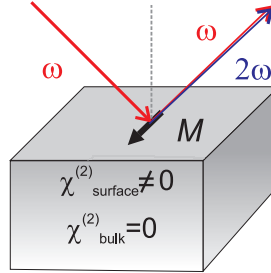


**Figure 2.13:** Magnetic second harmonic generation from surface and bulk of material. For isotropic materials like Gd the second order susceptibility tensor vanishes in the bulk material while at the surface this component is non-zero which makes SHG a surface sensitive probe.

XMCD measurements and then MOKE rotation and ellipticity results were compared with the XMCD measurements as discussed in chapter 4 and 6.

### 2.4.2 Magnetic second harmonic generation (MSHG)

The second harmonic generation was first time observed after the availability of lasers which provided high intensity optical fields [100]. For large optical fields, the response of the material is nonlinear and a considerable fraction of the light with frequencies multiple of the incident light can be observed. The second and higher order terms (in equation (2.34)) are important when the intensity of the incident light is approaching the strength of the material's intra-atomic fields, we consider here only the second order term which is responsible for the second harmonic generation. This is the reason for the first SHG observation after the invention of the laser. The phenomenon of the second harmonic generation can be understood considering the charges as a collection of oscillating dipoles acting as a source of the secondary radiations, in response to the field of incident light. In principle the oscillating dipoles emit radiation at  $\omega_2 = \omega + \omega = 2\omega$  in all directions in space. With appropriate arrangements [101] (called phase matching conditions) defined by the energy and particularly the angular momentum conservation, the radiation pattern can be maximized in one direction.

For second harmonic generated from a magnetic material the nonlinear susceptibility can be presented as a combination of magnetic and non-magnetic part as [42]

$$\chi_{ijk}^{(2)} = [\chi_{\text{even}}^{(2)}]_{ijk} + [\chi_{\text{odd}}^{(2)}(M)]_{ijk}, \quad (2.43)$$

## 2. Fundamentals

---

where odd (even) part of the susceptibility tensor (does not) changes upon magnetization reversal. Experimentally one measures the second harmonic intensity for opposite magnetization directions, which can be expressed as

$$I_{2\omega}^{\uparrow,\downarrow} \propto |E_{\text{even}}^{2\omega} \pm E_{\text{odd}}^{2\omega}|^2, \quad (2.44)$$

where  $\uparrow$  and  $\downarrow$  are used to represent opposite directions of magnetization.

Due to spatial inversion symmetry in the isotropic materials the nonlinear susceptibility tensor vanishes  $\chi^2 = 0$  in the bulk of the material (figure 2.13), within the dipole approximation, as a result the second harmonic signal from the bulk of the material is negligible. At the surface, however, when the spatial symmetry is broken the second harmonic signal is non-zero  $\chi^2 \neq 0$ . This is a very important aspect of SHG which is used excessively to investigate the surfaces and interfaces of the ferromagnetic materials [102, 103]. With the application of the femtosecond laser pulse the higher intensities of light can be applied without generating strong thermal load on the sample, therefore, the study of SHG with fs laser is beneficial in addition to its time resolution for time-resolved experiments. Gd having isotropic symmetry is a special case with more surface sensitivity for SHG due to resonance absorption from surface state [42].

### 2.4.3 Magneto-optical effects in the x-ray energy regime and XMCD

As optical absorption is related to sum over all allowed transitions in the conduction band up to a specific energy of the exciting beam, it is reasonable to assume that the MOKE is primarily sensitive to the  $5d6s$  magnetic moments (as shown in figure 2.14) and potential non-magnetic contributions to MOKE may not be avoided [17, 18, 19], as discussed in section 2.4.1. Therefore, a complementary approach which can be used is the x-ray magnetic circular dichroism (XMCD) technique. The difference in the absorption of left and right circular polarized x-rays when passing through magnetic material is called the XMCD. In figure 2.14 the difference between magneto-optical and x-ray magneto-optical spectroscopy is highlighted. The basic phenomenon of the magneto-optical effect for the x-ray energy can be explained in a similar way as the Kerr effect, however, the higher and tunable x-rays energies give access to the characteristic core level transitions.

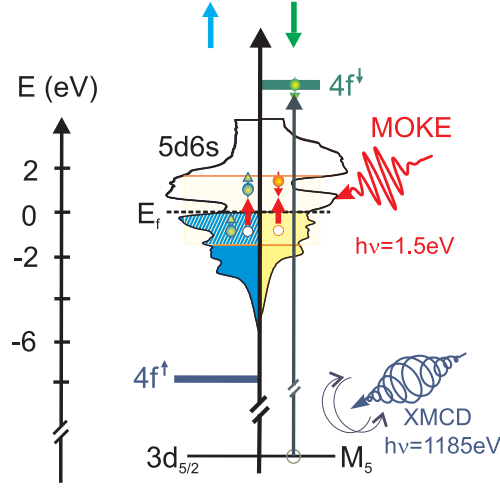


**Figure 2.14:** Schematic representing the magneto-optical spectroscopy with visible (with  $h\nu=1.5$  eV) and x-ray photons in Gd. In XMCD, firstly spin-polarized photo electrons are generated from the spin-orbit split  $3d$  states. In the second step these electrons are collected by the unoccupied  $4f$  states. The transition probability is determined by the density of the final states, the selection rules and the polarization of the photons. Using visible light to study the MOKE corresponds to the excitation of electrons in the conduction band. Conduction electron density of states used after Ref. [104].

In x-ray spectroscopy an electron from core level is promoted to the valence band. Since the characteristic core level transitions can be well resolved for different materials, this property of x-ray spectroscopy makes it a very powerful tool for the characterization of the magnetic materials with its element specificity. The x-ray absorption coefficient  $\mu(E)$  for a transition from core level  $i$  to final level  $f$  can be described in the frame-work of the Fermi Golden Rule [105, 106]

$$\mu(E) \propto \sum_f |\langle f | \mathbf{p} \cdot \mathbf{A} | i \rangle|^2 \delta(\hbar\omega - E_i - E_f), \quad (2.45)$$

where  $\mathbf{p} \cdot \mathbf{A}$  ( $\mathbf{p}$  is the electron momentum operator and  $\mathbf{A}$  the vector potential of the electromagnetic field) accounts for the interaction of the x-ray field with the matter. In dipole approximation it can be shown that  $\mathbf{p} \cdot \mathbf{A} \approx \hat{\epsilon} \cdot \hat{r}$  with  $\hat{\epsilon}$  the polarization of the incident photon and  $\hat{r}$  the position of the electron. This single electron picture with dipole approximation gives a reasonable practical solution. The selection rules for

## 2. Fundamentals

---

dipole transitions can be described as [9]

$$\Delta l = \pm 1, \Delta m_l = \begin{cases} 0 & \text{(linear polarization)} \\ \pm 1 & \text{(circular polarization)} \end{cases}, \Delta s = 0, \quad (2.46)$$

where  $m_l$  is magnetic orbital quantum number and  $\pm$  is used for helicity of the x-rays. As indicated by the eq. 2.45, the absorption coefficient depends not only on the initial state but also on the final state. This is very important for magnetic materials, since the density of available states is different for majority and minority spins; along with the selection rules this leads to a different absorption for the left and right circular polarized light which is discussed below and highlighted in figure 2.14. Due to the magnetic origin of the splitting, the difference in the absorption for opposite helicity of the x-rays can be attributed to the magnetization.

$$\Delta\mu = \mu^\uparrow - \mu^\downarrow \propto M. \quad (2.47)$$

Note that the effect remains similar if one changes the direction of the magnetization with fixed helicity of the x-ray beam [107].

To explain the XMCD process Stöhr and Wu suggested a two-step model [107]. In the first step, circularly polarized x-rays with energy corresponding to a particular absorption edge generate electrons with a spin and/or orbital momentum from a core level of an atom. In the second step, the valence shell serves as the detector of the spin or orbital momentum of the photoelectron. The physical mechanism on the microscopic level which give rise to the magneto-optical effects in general is the combined effect of the spin-orbit coupling and the exchange interaction together with the selection rules for optical transitions, the details can be found in Refs. [98, 108]. Another important aspect of XMCD is to resolve the spin and orbital moment contributions using so called *sum rules* [109], that are experimentally proved to work well for transition metals ferromagnets. However, their applicability to lanthanide ferromagnets is not yet fully understood [110].

To sum up, the rich variety of applicability and availability of the fs time-resolved MOKE technique will be used to study the magnetization dynamics of the  $5d6s$  magnetic moments in lanthanides. Since the laser with 1.5 eV energy excites the electrons in the conduction band of the lanthanides (figure 2.14), optical artefacts as well as the state blocking effects can contribute to the MOKE signal in strongly excited conditions

## 2.4 Magneto-optical techniques as a probe of magnetization dynamics

---

after fs laser excitation. Complementary to MOKE, the time-resolved XMCD technique was also utilized with resonant excitation of the electron from occupied  $3d_{5/2}$  to unoccupied  $4f$  level (figure 2.14), corresponding to the  $M_5$  absorption edge. By XMCD we probe the dynamics of the  $4f$  magnetic moments. The availability of these two techniques gave us a good opportunity to compare the magnetization dynamics of two spin sub-systems ( $4f$  and  $5d6s$ ) which can give information about the flow of angular momentum from localized  $4f$  system to the lattice through the conduction electrons. In addition to both these techniques, the time-resolved SHG is used to probe dynamics at the surface of the crystalline Gd film and then compare them with the bulk dynamics investigated with the time-resolved MOKE. This can give an interesting insight into the spin transport processes from the surface to the bulk of the investigated system. The experimental realization of these techniques will be discussed in chapter 3.

## 2. Fundamentals

---

## 3

# Experimental

The purpose of this chapter is to give the details of experimental techniques used in this work. We used two type of techniques in this project: (i) Lab based techniques which comprise the time-resolved magneto-optical Kerr effect (MOKE) and the magnetic second harmonic generation (MSHG) techniques and (ii) synchrotron based technique, time-resolved x-ray magnetic circular dichroism (TRXMCD). Therefore the first section consists of experimental details of the laboratory based setup with ultrahigh vacuum chamber (UHV), sample preparation, femtosecond laser system and detection system for the time-resolved MSHG and MOKE measurements. The time-resolved XMCD technique is briefly discussed at the end of the chapter.

### 3.1 Laboratory based setup for magneto-optical characterization

Most of the experiments discussed in this thesis were carried out at a laboratory-based setup that combines a femtosecond (fs) Ti:Sapphire laser, an ultrahigh vacuum (UHV) chamber for in situ sample preparation and an optical characterization and detection system for MSHG and MOKE measurements.

#### 3.1.1 UHV chamber and sample preparation

The high reactivity of the lanthanide metals leads to the build up a monolayer coverage of rest gases on metal surfaces within a few seconds for the pressure of the order of  $10^{-6}$  mbar [111]. Therefore, the study of high quality single crystal films requires to

### 3. Experimental

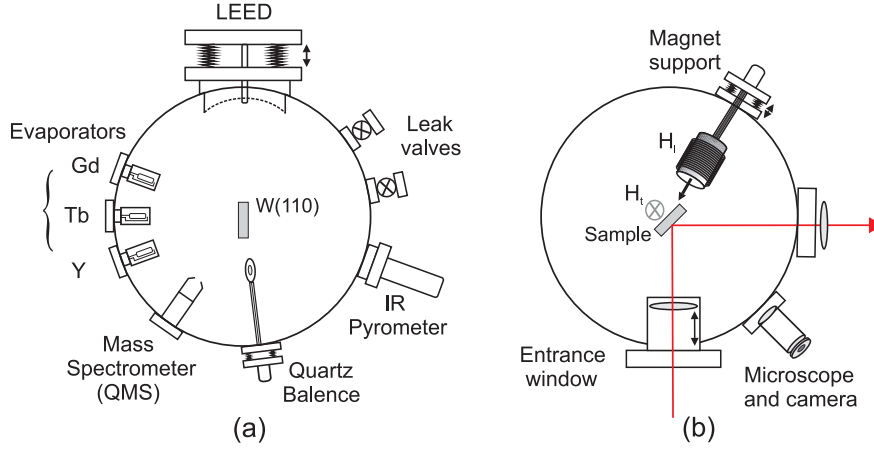


**Figure 3.1:** Schematic of ultrahigh vacuum chamber with (a) preparation chamber and (b) optical level. The preparation chamber comprises: sample holder, evaporators, QMS, microbalance and LEED. The optical level consists of specially designed fused silica entrance and exit windows, magnets in longitudinal ( $H_l$ ) and transverse ( $H_t$ ) direction with respect to optical propagation and a microscope for optical alignment.

work in ultrahigh vacuum (UHV) conditions with a pressure  $p < 10^{-10}$  mbar to assure clean surfaces during investigation.

The UHV chamber used in this work was pumped by a turbomolecular pump (Leybold Turbovac 361) together with a pumping stage (Pfeiffer), which consists of a turbomolecular pump and a diaphragm pump attached in series, the latter serving as a pre-vacuum pump. In order to get lower pressures, a titanium sublimation pump (TSP) was also employed. The high reactivity of gadolinium gives opportunity to utilize it as an additional modality of chemical pumping. Careful bake-out of the chamber followed by the cycles of pumping with TSP pump and degassing can result in a base pressure of  $\approx 10^{-11}$  mbar. The residual gas analysis of the obtained vacuum was performed with a quadrupole mass spectrometer (QMS).

The UHV chamber can be divided into two levels as shown in figure 3.1: (a) The preparation level for thin film deposition and respective structural characterization and (b) the optical level for the linear and nonlinear magneto-optical measurements. The preparation level consists of three home-built evaporators of gadolinium (Gd), terbium (Tb) and yttrium (Y). These evaporators consist of a tungsten crucible and filament for electron beam evaporation of thin films. The film thickness and deposition rate were monitored by a quartz microbalance (QMB). A low electron energy diffraction (LEED)



### 3.1 Laboratory based setup for magneto-optical characterization

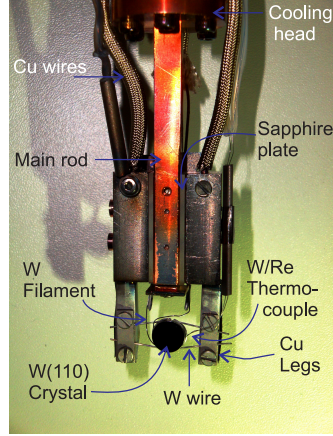


**Figure 3.2:** Sample holder with tungsten W(110) substrate used for the epitaxial film preparation and optical characterization.

instrument was installed in order to check the long-range structural ordering of the deposited films and substrate quality. For the optical level, a special entrance flange has been installed which allows the positioning of the focusing lens closer to the sample. A focusing diameter of the laser beam up to  $\sim 70\mu\text{m}$  can be achieved [42], this results in higher laser fluences of the order of  $1\text{mJ}/\text{cm}^2$ . Fused silica UHV windows were used for the entrance and exit of laser beams which exhibit a high transmission ( $\geq 95\%$ ) over a wide spectral range ( $250\text{ nm}$  to  $2\mu\text{m}$ ). Two electromagnets with longitudinal ( $H_l$ ) and transverse ( $H_t$ ) magnetic fields with respect to the optical polarization were installed which produce magnetic fields up to 800 Oersted.

#### Sample holder

In order to have good cooling efficiency for low temperature measurements a specially designed sample holder was used in this work which can be employed in a variable range of temperatures from 30K for optical investigation to 3000K for flashing (The process of heating the sample to elevated temperatures of 3000 K for a few seconds.) of the film. The parts of the sample holder are shown in figure 3.2.

The W(110) crystal which was used as a substrate for the thin film preparation was mounted and tightly fixed with the help of two tungsten wires (diameter 0.3 mm). The tungsten wires hold the sample on one side and were tightened between a thick tantalum plate and the sample holder leg on the other side. A thermocouple was installed in a 0.3 mm hole made in the W crystal. For safety precautions during flashing, the copper legs

### 3. Experimental

---

were covered with a thin tantalum foil. In order to obtain good thermal conductivity and electrical isolation at low temperatures, a pair of polished sapphire plates (thickness 1 mm) was mounted between the main rod and the Cu legs. A protective Cu shield was mounted in order to avoid the deposition of metal films on the sapphire plates during flashing and hence electrical short circuits. This Cu shield also acts as radiation shield for good cooling efficiency.

The sample holder was attached to the cold finger with continuous flow cryostat which was generally used with liquid helium, the best obtainable cooling temperature was 30 K. The whole construction was mounted on a differentially pumped manipulator that allows displacements along x and y directions as well as vertical z motion with a 360° rotational degree of freedom. The sample can be heated in two ways: by resistive heating via the tungsten wires which hold the sample or by electron bombardment using a separate tantalum filament (diameter 0.3 mm) installed behind the sample. The filament was generally used for high temperature treatments, for example flashing. In order to obtain high temperatures, electrons were produced by a 5 A current flowing through the filament and accelerated by  $\sim 700$  V voltage applied between sample and ground. A temperature of up to 1200 K can be obtained through resistive heating by flowing a current of 20 A through the tungsten wires supporting the sample. A W/Re (W5%Re/W26% Re) type C thermocouple attached directly to the tungsten substrate was used to monitor a wide range of temperatures (20 K – 2500 K). Complementary to the thermocouple, a pyrometer was also installed outside the chamber which can be used for temperature measurements above 1000 K.

#### Sample preparation

Two types of samples have been used in this work: first epitaxial lanthanide metals (Gd, Tb) films and their alloys on tungsten W(110) substrate and second poly-crystalline films of the same materials on Al substrate, latter used for the XMCD study. Although the evaporation conditions are the similar for both types of samples, the crystalline films require additional substrate preparation before evaporation and annealing of the sample after evaporation. The sample used for the XMCD measurements was an amorphous film of Gd, Tb metals and their alloys, evaporated on Al substrate as described in section 4.1. The growth of epitaxial sample on W(110) substrate is discussed in detail in the following.

### 3.1 Laboratory based setup for magneto-optical characterization

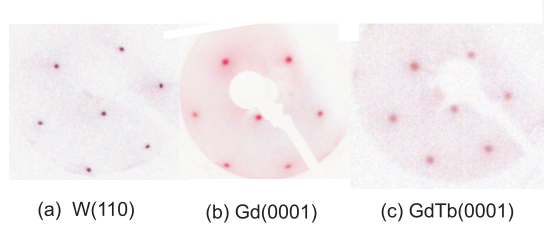


**Figure 3.3:** LEED images (inverted contrast) of (a) W(110) substrate after preparation for thin film evaporation. (b) Gd(0001)/W(110) and (c) GdTb(0001)/W(110) alloys films of 20 nm thickness after annealing at 700 K. The images were recorded at about 120 eV and 100 K sample temperature.

A relatively small mismatch ( $< 15\%$ ) between (110) surface of the W and (0001) surface of the lanthanide metals (Gd and Tb) makes it advantageous to use W as a substrate for crystalline lanthanide films. This small difference of lattice constant can still generate strains that vanish after four monolayers of Gd [112]. Preparation of high quality crystalline films requires the substrate to be clean and smooth, which can be achieved through special treatment. The W(110) substrate is cleaned by short (few seconds) cycles of heating up to 2600 K, the flashing. Contaminants like carbon and sulfur can diffuse into bulk upon heating. In order to remove these contaminants, several cycles of heating the sample to 1600 K in partial pressure of oxygen ( $p = 2 \times 10^{-7}$  mbar) were used. The high reactivity of the lanthanide metals can also be helpful for further preparation of the substrate.

Home-built evaporators were used for evaporation of the material on the substrate. The substrate temperature were kept constant (300 K) during evaporation. The crucible was heated by electron beam acceleration generated by tungsten filament. For the preparation of a single crystal film, lanthanide metals of 99.99 % purity filled in tungsten crucible were evaporated by electron beam heating onto a W(110). The deposition rate of  $5 \text{ \AA}/\text{min}$  was controlled by a quantum micro balance, followed by 10 minutes annealing to 700 K. This produced a smooth and epitaxial film [113], which were confirmed by the LEED images. As an example the LEED images of W(110), Gd(0001) and GdTb(0001) alloys films after annealing are shown in figure 3.3. The sharp images confirm the crystallinity and good quality of the films. For the preparation of the GdTb alloys film, the two evaporators were simultaneously used by controlling their rate prior to the evaporation. Although it was not possible to resolve the rate of

### 3. Experimental

---

evaporation of the individual constituents Gd/Tb during evaporation, the investigation of the prepared films by x-ray absorption spectroscopy confirmed that the measured ratios of Gd and Tb in the alloy films were within 5 % of the estimated values.

#### 3.1.2 Femtosecond laser system

The femtosecond laser system employed in this project is a home built cavity dumped Titanium-sapphire (Ti:Al<sub>2</sub>O<sub>3</sub>) oscillator laser [42]. The layout of the whole experimental system with the laser cavity, optical pump-probe scheme and the detection system are depicted in figure 3.4. The discussion of the laser system is divided into two parts: first the laser cavity to generate femtosecond pulses along with the pump laser and pump-probe scheme, and second part related with the detection system to focusing on the linear and non-linear magneto-optical detection.

##### (a) Generation of femtosecond laser pulses by mode locking/Titanium:Sapphire oscillator

The broader spectral bandwidth<sup>1</sup>(centred around 790 nm wavelength) along with its excellent thermal and hardness properties make the Ti-sapphire one of the most efficient media to generate femtosecond oscillator laser systems [114]. The Ti:Sapphire crystal is enclosed in a special arrangement of mirrors called the cavity. The length of the cavity allows waves of certain frequencies as standing waves, the longitudinal modes of the cavity. These longitudinal modes usually oscillate with random phase in the cavity. A technique to achieve the phase-locking of these longitudinal modes is called *mode-locking*. By mode locking one can produce intense, coherent and extremely short light pulses. Their pulse duration is defined by a number of parameters like locked modes and pulse profile. In our setup, mode locking was achieved using the nonlinear optical Kerr effect which produces self focusing and self-phase modulation of the longitudinal modes [42].

In figure 3.4 an outline of the entire experimental setup is shown schematically. The cavity of the oscillator is constructed in an X configuration with two asymmetric length branches. The second-harmonic (532 nm) of a continuous wave (CW) diode laser (Millennia 5W, Spectra Physics) is used for pumping the Ti:Sapphire crystal. The

---

<sup>1</sup>The laser pulse duration  $\tau_p$  is determined by the gain bandwidth  $\Delta\nu$  i.e  $\tau_p \cdot \Delta\nu \geq C$ ,  $C$  is a constant defined by the pulse profile.

### 3.1 Laboratory based setup for magneto-optical characterization

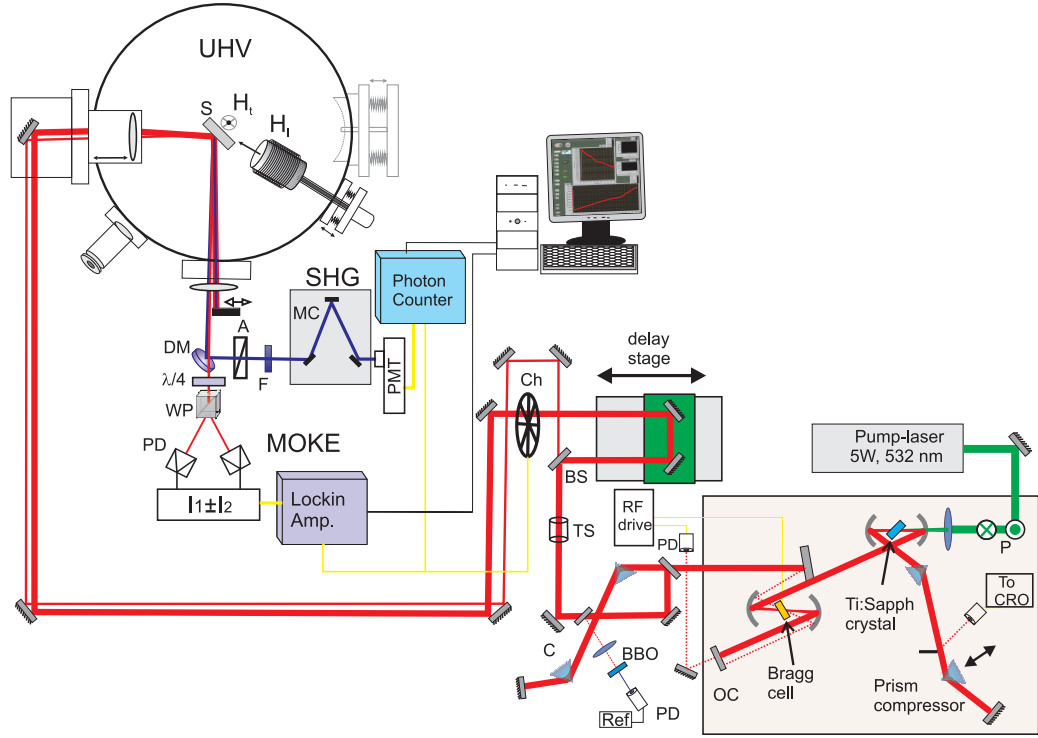


**Figure 3.4:** Schematic view of the whole experimental setup with femtosecond laser system, UHV chamber and detection system. Starting from the right, the laser oscillator comprises: Nd:YVO<sub>3</sub> (Millennia) used for pumping the Ti-Sapphire crystal through a perimeter (P); curved mirrors enclosing the Bragg cell and Ti-Sapphire crystal; prism compressor; cavity dumper control (RF Drive) unit; OC-output coupler; PD-photodiode. The second part outside the oscillator is the pump-probe scheme which comprises: second prism compressor; reference channel with nonlinear BBO crystal; BS-beam splitter; delay stage; Ch-chopper and guiding path of the beam into UHV chamber. In the UHV chamber S is the sample with  $H_l$  and  $H_t$  the longitudinal and transverse magnetic fields, respectively. After reflection from the sample the beam is guided to the detector systems which consist of SHG and MOKE detectors. For the MOKE measurements, a balanced detection scheme is used with: optional  $\lambda/4$  (quarter) wave plate for MOKE ellipticity measurements; WP-wollaston prism; PD-photodiodes; preamplifier and lock-in amplifier. The SH signal is directed into a photomultiplier tube (PMT) through: DM-dichroic mirror; A-analyzer; F-filter and MC-monochromator. The signal is then collected and analyzed by computer.

### 3. Experimental

---

CW pump beam is focused on to the Ti:Sapphire crystal through a periscope which serves as a polarization rotation device. The crystal was oriented at Brewster angle for minimizing the losses due to reflection. The optical resonator comprises six mirrors: two spherical mirrors around the Ti:Sapphire crystal, which are highly transmissive for pump light (532 nm) and highly reflective for laser radiation centered at 800 nm. Two more high-reflective (HR) mirrors enclose the cavity with one of them acting as an output coupler (OC). In cavity dumping mode of operation the OC transmits 4% of the signal from the cavity.

In order to deflect the beam out of the oscillator a Bragg cell together with a fused silica crystal is inserted in the shorter arm of the cavity which is enclosed within two curved mirrors. By applying an external electrical signal an acoustic wave can be produced by a piezoelectric transducer attached at the bottom of the fused silica crystal. When the external electrical signal is appropriately synchronized with the mode-locked laser, the Bragg cell acts as an acoustically induced optical grating which diffracts the laser beam out of the oscillator through a (pick-off) mirror. The synchronization was achieved electronically by a driving unit (APE Berlin). In addition, two fused silica prisms mounted in a double-pass configuration are installed for the group velocity dispersion (GVD) compensation. The residual light reflected from a knife placed close to the prism compressors, detected by a fast photodiode, is used to monitor the pulse train in the oscillator with an oscilloscope. In addition, a spectrometer (not shown) is also installed in the cavity to analyze the spectrum of the laser in the cavity. The initial repetition rate of the laser in cavity (78 MHz) can be divided in a ratio from 20 to 5000. However, we used 1.52 MHz repetition rate corresponding to a 1:50 ratio which results in high pulse energy with a negligible DC heating in the sample, providing a stable operating regime of the oscillator. In order to obtain the high repetition rate, the cavity dumped mode of the oscillator was used in this project. Laser pulses of 35 fs duration and 40 nJ energy at 800 nm central wave length with a repetition rate of 1.52 MHz were used for the measurements.

#### (b) Pump-probe scheme

In order to compensate any additional GVD acquired along the optical path from oscillator to sample (e.g. air, mirrors, UHV window), a second prism compressor is installed at the exit from the oscillator cavity. The prisms are made of SF11 material

### 3.1 Laboratory based setup for magneto-optical characterization

---

and their combination (compressor) can provide a negative GVD in the order of  $-4550 \text{ fs}^2$  [115]. A small part of the laser output is reflected and focused in the BBO crystal that produces SHG in transmission which is detected by the photodiode. This SHG signal is used as reference channel to monitor the fluctuations and instabilities in the laser intensity.

A beam splitter divides the laser into two beams, labeled as pump and probe beams at a 4:1 ratio. A delay stage (Physik Instruments) is installed in the path of the pump beam in order to control the time delay between pump and probe for time-resolved measurements. The smallest achievable delay step is 0.5 fs. A chopper working at a frequency of 500 Hz is inserted in the pump beam that makes it possible to measure the pump-induced variations of the detected signal i.e. to measure the probe signal for on and off-pump. After that both beams are directed to the UHV chamber in a collinear manner and focused on the sample using a plano-convex lens (fused silica  $f=100 \text{ mm}$ ). For better focusing at the sample position a telescope is also installed before the delay stage. The obtainable absorbed pump fluence is  $\sim 1 \text{ mJ/cm}^2$  for a focus diameter of  $\sim 70 \mu\text{m}$  and a pump pulse energy of 40 nJ. To check the position, focus quality and the spatial overlap of the pump and probe on the sample a microscope with a CCD (charge coupled devices) camera is installed outside the UHV chamber. The beam is directed to the sample at  $45^\circ$  incidence angle. After reflection from the sample the beams are directed in the detection part.

#### 3.1.3 Detection system for time-resolved measurements

The detection system consists of two main setups: time-resolved magneto-optical Kerr effect (TRMOKE) and magnetic second harmonic generation (TRMSHG) for linear and nonlinear magneto-optical spectroscopy, respectively. In the following both of these are discussed separately.

##### 3.1.3.1 TRMOKE

After reflection from the sample, a balanced detection scheme [92, 116, 117] was used to measure the magneto-optical Kerr effect (MOKE) in the longitudinal MOKE geometry. A wollaston prism (WP) was used to split the beam into two perpendicular polarized components which were detected by two photodiodes (PD). The magneto-optical Kerr rotation ( $\theta$ ) and its pump induced change ( $\Delta\theta$ ) were recorded with open as well as

### 3. Experimental

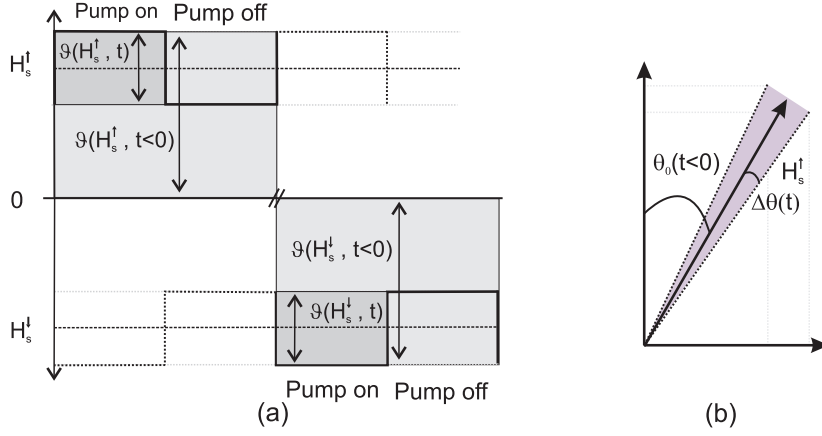


**Figure 3.5:** (a) Detection of the differential  $\vartheta(H_s, t)$  and integrated  $\vartheta(H_s, t < 0)$  MOKE signal with and without pump excitation, respectively. (b) Schematic showing the time-resolved detection of change in polarization.

blocked pump using a chopper operating at 500 Hz. The magneto-optical signals were analyzed by a lock-in amplifier to detect the differential signals for open and blocked pump in opposite saturation magnetic fields ( $H_s^{\uparrow, \downarrow}$ ) as a function of pump-probe delay  $t$ . Figure 3.5 represents the schematics of the MOKE measurement principle. The  $\vartheta(H_s^\uparrow, t)$  represents the differential signal collected during the excitation with the pump and  $\vartheta(H_s^\uparrow, t < 0)$  denote the integrated signal collected before the optical excitation has occurred. In order to compare different transients the pump-induced change in signal is normalized to the total MOKE signal before optical excitation as

$$\frac{\Delta\theta(t)}{\theta_0} = \frac{\theta(t)}{\theta_0} - 1 = \frac{\vartheta(H_s^\uparrow, t) - \vartheta(H_s^\downarrow, t)}{\vartheta(H_s^\uparrow, t < 0) - \vartheta(H_s^\downarrow, t < 0)} - 1, \quad (3.1)$$

where  $\vartheta$  is the angle between the linear polarization of the reflected probe pulse and a fixed reference polarization and  $\theta$  is the magneto-optical Kerr rotation.  $\Delta\theta$  is the time-dependent change in the Kerr rotation which represents the magnetization of the bulk part of the Gd film.

Figure 3.6(a) shows typical hysteresis loops of the Gd(0001) film before pump excitation (squares) and 50 ps after excitation (circles). A change of 15 % in saturation magnetization was observed 50 ps after pump excitation. In time-resolved measurements, Kerr rotation was recorded for the opposite direction of magnetization and the difference between both  $\Delta\theta = \Delta\theta(H_s^\uparrow) - \Delta\theta(H_s^\downarrow)$  was used to minimize the non-



### 3.1 Laboratory based setup for magneto-optical characterization

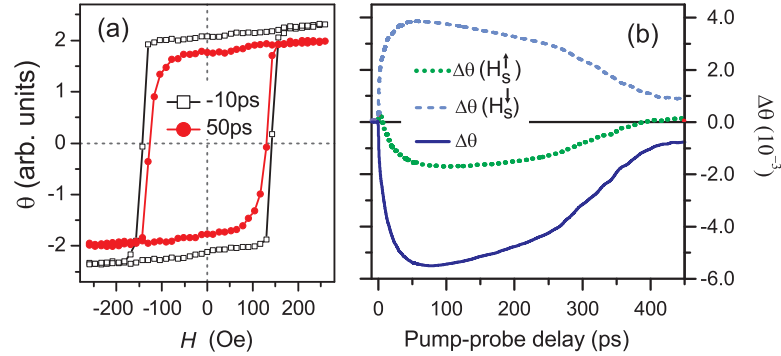


**Figure 3.6:** (a) Magnetic hysteresis before (squares) and 50 ps after (circles) the pump laser excitation. The difference in hystereses at the saturation fields show the pump-induced change. (b) Exemplary time-resolved MOKE rotation data for opposite direction of magnetization as a function of pump-probe delay and the difference of the signal  $\Delta\theta$  gives the evolution of magnetization.

magnetic contributions (shown by solid line in figure 3.6(b)). Figure 3.6(b) shows the temporal evolution of the pump-induced change  $\Delta\theta$  for opposite direction of magnetization as a function of pump-probe delay up to 500 ps after laser excitation recorded at  $T_0 = 130$  K. For comparison of different measurements, the MOKE signal was normalized to the MOKE signal  $\theta_0$  without pump excitation, as shown in equation 3.1. In order to measure the MOKE ellipticity ( $\varepsilon$ ) a  $\lambda/4$  wave plate was installed before the Wollaston prism. It produces a  $\pi/2$  phase shift of incident light which interconverts Kerr rotation and Kerr ellipticity.

#### 3.1.3.2 TRMSHG

The details of the magnetic second harmonic generation (SHG) and measurements can be found in earlier work [42]. Therefore, only a brief discussion of the experimental principle is presented here.

As SHG is a nonlinear effect, it requires high electric fields which were here provided by ultrashort laser pulses and were recorded by a sensitive detection scheme. To detect the  $p$ -polarized second harmonic (SH) generated by the  $p$ -polarized probe pulse the second harmonic signal was separated from the first harmonic using a dichroic filter and directed on to a monochromator selecting 400 nm and finally on a photomultiplier tube. The monochromator further removes the first harmonic from the signal. An additional analyzer can be used to detect the  $s$ -polarized component of the SH signal.

### 3. Experimental

---

A single photon counter was used to record the signal from photomultiplier tube. SHG was detected in the transversal geometry leading to magneto-induced changes in the SH intensity (from eq. 2.44)

$$I_{2\omega}^{\uparrow,\downarrow} \propto (E_{\text{even}}^{2\omega})^2 + (E_{\text{odd}}^{2\omega})^2 \pm 2E_{\text{even}}^{2\omega}E_{\text{odd}}^{2\omega} \cos \phi, \quad (3.2)$$

here  $E_{\text{even}}^{2\omega}$  and  $E_{\text{odd}}^{2\omega}$  are the SHG optical fields which behave as even or odd with respect to the reversal of the magnetization  $M$ . The phase between these two field contributions is  $\phi$  which is smaller than  $15^\circ$  and weakly time-dependent [43]. Since  $E_{\text{odd}}^{2\omega} \propto M$  we plot below

$$\Delta_{\text{odd}}^{2\omega}(t) \approx \frac{E_{\text{odd}}^{2\omega}(t) - E_{\text{odd}}^{2\omega}(t < 0)}{E_{\text{odd}}^{2\omega}(t < 0)} \approx \frac{M(t) - M(t < 0)}{M(t < 0)} = \frac{\Delta M(t)}{M_0}, \quad (3.3)$$

which represents the time-dependence of the surface sensitive magneto-optical signal.

### 3.2 Time-resolved XMCD

The time-resolved XMCD facility of the BESSY-II synchrotron was used to investigate the dynamics of the localized  $4f$  magnetization of lanthanides. This setup was used as a user facility and XMCD measurements were only possible with the cooperation of the BESSY staff. In this experiment the  $5d6s$  conduction electrons were excited by 1.5 eV laser pulses (pump) and the dynamics of the  $4f$  magnetic moments is investigated by time delayed circular x-ray pulses (probe). The general overview of the experimental setup is depicted in figure 3.7. The important feature of this setup is the production of circularly polarized x-ray pulses with the help of an elliptical undulator down to femtosecond pulse duration. X-ray pulses of different pulse duration can be generated using various modes of operation of the x-ray source. Depending on the temporal region of interest for dynamical studies, a specific mode of operation can be utilized.

The normal mode of operation can be used to study the static magnetic properties. In order to study the magnetization dynamics, low alpha and femtoslicing mode of operation were used. The schematic of the laser pump x-ray probe setup is shown in figure 3.7. In the BESSY low- $\alpha$  operation mode special electron optics are used to compress the electron bunches [118] and reduction of the length of the bunches in the storage ring to 10 ps can be achieved, however at the cost of reduced intensity.

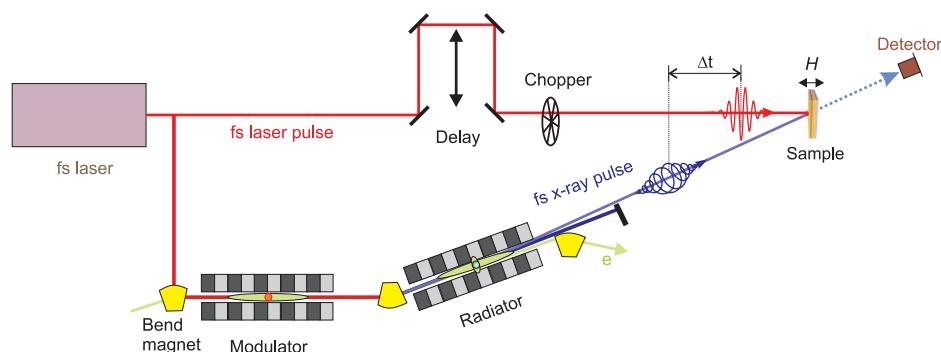


**Figure 3.7:** General view of femtosecond slicing facility of BESSY-II [40] used for the time-resolved XMCD measurements. A laser beam is used to excite the sample as well as to modulate the portion of electron bunch (slicing) in the modulator. The sliced X-ray beam is separated in radiator and incident on the sample at  $30^\circ$ .

A Ti:sapphire laser system with a repetition rate of 1-3 kHz,  $\sim 40$  fs pulse duration, a pulse energy of 2 mJ and 780 nm wavelength is used as a pump to excite the sample. In femtoslicing mode a part of the laser was used to generate the short x-ray pulses. The fs slicing technique [40, 119] employs fs laser pulses that co-propagate with electrons in the storage ring through a planar undulator. By this procedure an energy modulation of the electrons is generated, which is transferred into an angular separation by a dipole magnet. A subsequent elliptical undulator produces circularly polarized x-ray pulses and beamline apertures let only its fs component pass to the sample. This results in x-ray pulses as short as 100 fs. A small fraction of the total bunch current contributes to the slicing process, therefore, the x-ray intensity is reduced by a factor of about  $10^5$  compared with the incident intensity of the beam. This leads to a strong reduction of the number of photons per pulse at sample position. Despite efficient single photon counting, the duration of individual time-resolved measurements can be up to several weeks. This limitation was partially improved by the installation of a zone-plate-monochromator (ZPM), which increased the x-ray flux by an order of magnitude [120, 121]. The GaAs photodiode and Si avalanche photodiode detector were used for static and time-resolved measurements, respectively. The time-dependence of magnetization was determined with magnetization saturated in an external magnetic field  $H$  of 5 kOe parallel and antiparallel to the direction of x-ray incidence with sensitivity to changes in magnetization projected onto  $H$ .

### 3. Experimental

---

## 4

# Laser-induced magnetization dynamics of Gd and Tb

As discussed in chapter 2, the magnetic structure of lanthanide ferromagnets is different from the itinerant one. The dominant part of magnetization originates from the localized  $4f$  magnetization which results in ferromagnetic ordering through the spin polarization of  $5d6s$  conduction electrons. Therefore the magnetization of the lanthanides consist of two sub-systems: the  $4f$  and  $5d6s$  one. In this project two complementary techniques were employed, x-ray magnetic circular dichroism (XMCD) and magneto-optical Kerr effect (MOKE) which are specifically sensitive to the two spin sub-systems.

The angular momentum conservation requires transfer of momentum from the spin system to some other reservoir. The crystal lattice is a prominent candidate as a sink of angular momentum, which turns spin-lattice coupling into an essential, but barely investigated, interaction in ultrafast magnetization dynamics. Therefore the investigation of these dynamics is started to exploit the role of spin-lattice interaction.

As we will see in the results, the dynamics depends on the temporal regimes and therefore it is important to introduce the terminology here. The dynamics in the time regime when electron and phonon temperatures are strongly different, following fs laser excitation, is called the *non-equilibrium* regime. Since the electrons and phonons have equilibrated after 1 ps [27, 41], we refer to delays  $> 1$  ps as a *quasi-equilibrium*. This terminology will be used in the discussion of all results.

The XMCD measurements which are presented in section 4.1 were performed on

#### 4. Laser-induced magnetization dynamics of Gd and Tb metals

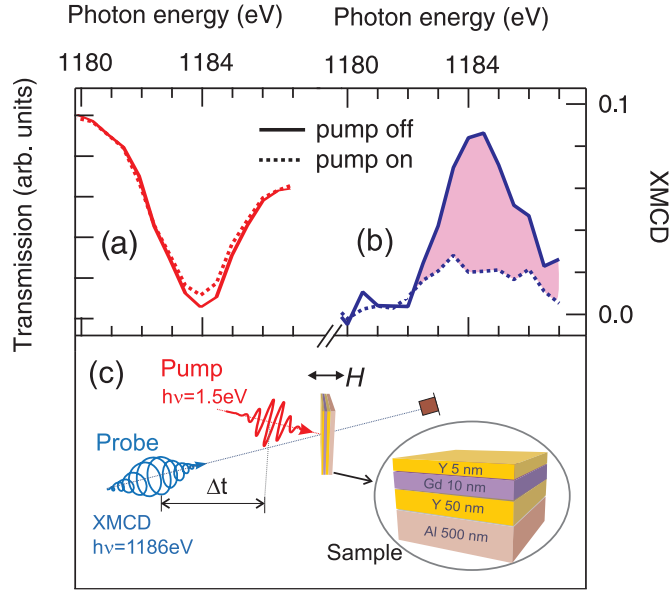


**Figure 4.1:** (a)<sup>1</sup> Transmission spectrum at the  $M_5$  absorption edge of Gd by circularly polarized x-ray pulses recorded without and with optical excitation (solid and dotted red lines, respectively). (b) The corresponding XMCD ( $\mu^\uparrow - \mu^\downarrow$ ) spectrum. The pink shaded region shows the pump-induced change in the spectrum. (c) The experimental pump-probe scheme and the sample used for the XMCD measurements.

the femtoslicing facility of BESSY-II. These results were obtained in a larger collaboration between BESSY, FU Berlin and MBI. In this project I participated by sample preparation, in beam times and in discussions. These results were already presented as a part of Marko Wietstruk thesis [122]. This data is included in section 4.1 because it provides the basis of the MOKE results which are discussed in the remaining chapters of this thesis. These results are reproduced by time-resolved MOKE and are compared with XMCD results in section 4.2.

#### 4.1 Magnetization dynamics investigated by XMCD

For the XMCD measurements in transmission mode, polycrystalline films were prepared on a free-standing  $0.5\text{ }\mu\text{m}$  thin Al substrate. The films were grown under UHV conditions by electron beam heated evaporation as described in chapter 3. As depicted in figure 4.1(c) the sample consists of Y(50 nm)/R(10 nm)/Y(5 nm), with R = Gd,Tb. The 50 nm layer of Y acts as a buffer between Al and R. In order to avoid oxidation, Gd and Tb surfaces were covered with an additional 5 nm layer of Y.

## 4.1 Magnetization dynamics investigated by XMCD

---

Before starting the time-resolved measurements, the static magnetic properties of the sample were analyzed using the normal mode of operation (see section 3.2 for details), the experimental geometry and x-ray absorption spectra are shown in figure 4.1. For optical pump–x-ray probe measurements the  $5d6s$  conduction electrons were excited by 1.5 eV laser pulses of 50 fs duration with the sample held in an applied magnetic field of 5 kOe at an equilibrium temperature of 140 K. The low alpha mode of operation was employed to optimize the fluence so that sizeable demagnetization can be achieved without load of DC heating. In this way the optimized fluence of  $F = 3 - 5 \text{ mJ/cm}^2$  was used. In figure 4.1<sup>1</sup> (a) the transmission of x-rays at the  $M_5$  edge is shown before and 200 ps after laser pulse excitation shown by solid and dashed lines, respectively. XMCD is determined from the difference of the absorption for opposite direction of magnetization. The corresponding XMCD spectra are shown in figure 4.1(b). Comparing XMCD signals before and 200 ps after laser excitation (figure 4.1(b) exhibits a pronounced pump-induced change, shown by the shaded area. The pump-induced change is not pronounced from simple absorption spectrum. The sum of the spectra (not shown here) remains unaffected even though the temperature is increased by the optical excitation. This guarantees that the change in XMCD is a purely magnetic effect. The  $M_5$  edge corresponds to resonant excitation of the  $3d_{5/2}$  core-level electrons to the unoccupied  $4f^\downarrow$  states with a binding energy of 4 eV above  $E_F$  [123] (as indicated in figure 2.14). Since optical transitions between  $4f$  and  $5d$  require photon energies far above 1.5 eV,  $4f$  levels are not affected by the optical excitation [124] and therefore XMCD can be used as a reliable monitor of magnetization [125]: pump-induced state filling of  $4f$  levels and saturation effects [17, 18, 19] do not affect the XMCD signal.

Time-resolved measurements were performed by tuning the energy of x-ray photons corresponding to the  $M_5$  absorption edges of Gd and Tb. By changing the time delay ( $\Delta t$ ) between pump (laser) and probe (x-rays) the dynamics is studied. The experimental scheme is depicted in figure 4.1(c). In the next section, the magnetization dynamics investigated by time-resolved XMCD is discussed.

---

<sup>1</sup>The XMCD results were obtained in close collaboration with the femtoslicing team (Marko Wietstruk, Christian Stamm, Torsten Kachel, Niko Pontius) at BESSY-II, Helmholtz-Zentrum Berlin and the Max-Born-Institute (M. Weinelt, C. Gahl).

## 4. Laser-induced magnetization dynamics of Gd and Tb metals

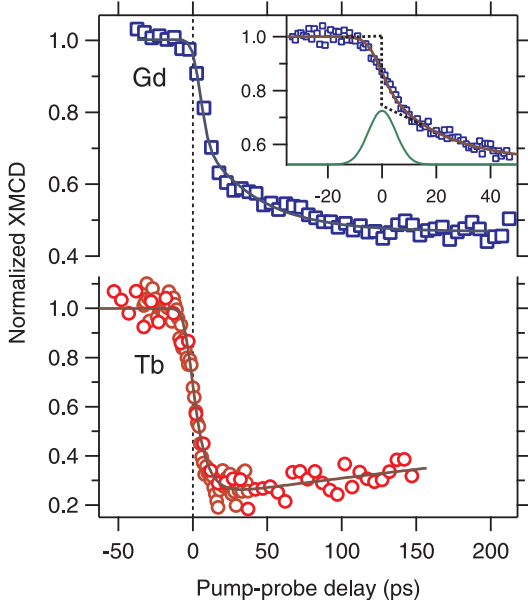


**Figure 4.2:** Change in XMCD signals for Gd (top) and Tb (bottom) measured by 10 ps x-ray probe after 50 fs laser pump excitation. The Gd shows slower demagnetization than Tb. Solid lines indicate fits to the data. The inset depicts Gd data in a smaller time window with the actual time-resolution of 10 ps indicated. The double-exponential fit (solid line) highlights the two step demagnetization process and the dashed line indicates the behavior expected for an instantaneous first step. From [58].

### 4.1.1 Quasi-equilibrium demagnetization

Investigation of the dynamics is started with the measurement in the low alpha-mode of operation. In this mode x-ray pulses of about 10 ps duration are available [118]. Figure 4.2 depicts the time-dependent XMCD signal for Gd and Tb measured at the  $M_5$  absorption edge. The data were normalized to the value before optical excitation. For both materials a pronounced demagnetization is found, however, in detail the behavior is different. For Gd the minimum of magnetization is reached after 200 ps whereas for Tb maximum demagnetization is reached at about 20 ps. The demagnetization of Gd near time zero cannot be described by a simple exponential behavior and demagnetization proceeds in a two-step process. This two-step process is evident with considering a 40 ps region of interest with better statistics, as shown in the inset. The x-ray pulse duration is represented by a gaussian pulse with FWHM of 10 ps which represents the temporal resolution of the experiment. About half of the final demagnetization occurs within the 10 ps pulse duration of the x-ray pulse, while the second process lowers the magnetization until 200 ps, the latter demagnetization can be described by an exponential decay. The double-exponential fit convoluted with the temporal x-ray pulse profile [122] gives a characteristic time constant of  $\tau_2^{\text{Gd}} = 40 \pm 10$  ps for the slower process. The obtained  $\tau_2^{\text{Gd}}$  is characteristic for the weak indirect spin-lattice coupling in Gd (as



## 4.1 Magnetization dynamics investigated by XMCD

---

depicted in figure 2.4 with  $L = 0$ ). The experimental resolution is not enough to resolve the dynamics of Tb quantitatively.

In the laser-induced process the absorption of the femtosecond laser pulse results in laser-heating of the conduction electrons to temperatures above 1000 K [8, 27]. After typically 1 ps an equilibrium between valence electrons and the lattice is established through electron-phonon scattering [8, 13, 20, 27]. Subsequently, the hot lattice will cool via heat transport within the sample. Hence, the lattice is heated within the x-ray pulse duration and remains hot thereafter, for hundreds of picoseconds time. The transient magnetization shows a fast drop, not resolved here, and a decay with a characteristic time of 40 ps, which describes equilibration of the  $4f$  spin and phonon systems under quasi-equilibrium conditions. Our measurements thus corroborate earlier indirect measurements [6, 8]. Regardless of its approximation for low temperatures, the theoretical calculations of Hübner et al. [33] based on the spin-lattice relaxation ( $\tau_{SL} = 48ps$ ) nicely agree with our experimental observation. The lower panel in figure 4.2 shows the demagnetization of Tb. In Tb the minimum of magnetization is reached already after 20 ps indicating a faster demagnetization, which is a consequence of the direct spin-lattice coupling (shown in figure 2.4 for  $L = 3$ ). In Gd diffusive cooling and slow demagnetization occur on similar time scales and lead to a plateau; in Tb cooling occurs after demagnetization and a recovery of magnetization is observed at delays  $> 20$  ps.

Following the direct spin-lattice coupling, the Tb shows faster demagnetization than Gd. However, the following is still not clear from the above results: (i) What is the fast demagnetization time scale in Gd? (ii) Does Tb also show two distinct demagnetization time scales and (iii) if yes do both differ with respect to Gd? To answer these questions femtosecond slicing mode of operation with better temporal resolution is employed as discussed in the following section.

### 4.1.2 Non-equilibrium demagnetization

To examine the magnetization dynamics within few picoseconds following laser excitation x-rays pulse of about 100 fs resolution from the slicing mode of operation were utilized. The results of magnetization dynamics with this time resolution are shown in figure 4.3 focusing on the initial few picoseconds dynamics. It is clear from figure 4.3 that both Gd and Tb show the reduction in magnetization within a few ps.

#### 4. Laser-induced magnetization dynamics of Gd and Tb metals

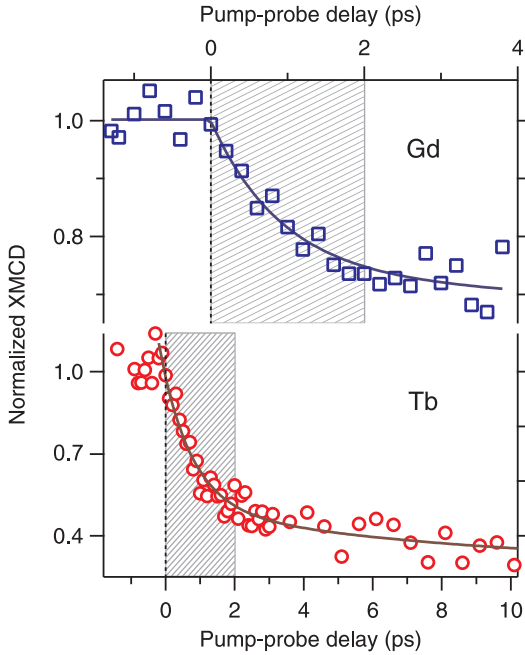


**Figure 4.3:** Laser-induced change in XMCD signals following laser excitation for Gd (top) and Tb (bottom) measured with 120 fs x-ray pulses. Note the different time intervals, shown as hatched. Solid lines depict double-exponential fits. From [58].

The normalized XMCD signal in Gd decreases to 0.7 after 3 ps, identical to the level at which the slower demagnetization process sets in (inset in figure 4.2). Also results for Tb reveal a sizeable drop of magnetization within 2 ps (hatched areas in figure 4.3) followed by a slower dynamics. To determine the characteristic time scales, the ps and fs time-resolved data have been fitted simultaneously by double-exponential functions taking into account the different x-ray pulse durations [122] (solid lines in figures 4.2 and 4.3). This allows to extract the two time scales. In particular a demagnetization time of  $\tau_2^{\text{Tb}} = 8 \pm 3$  ps in the quasi-equilibrium regime is observed for Tb. This process is explained as being mediated by direct spin-lattice coupling under quasi-equilibrium conditions persisting at corresponding delays  $> 1$  ps. The quasi-equilibrium demagnetization follows the strength of spin-orbit coupling and hence the demagnetization is faster in Tb than Gd, as mentioned in the earlier section.

Considering the ultrafast dynamics again, the determined values of non-equilibrium demagnetization times are identical for Gd and Tb within error bars ( $\tau_1^{\text{Gd}} = 0.76 \pm 0.25$  ps and  $\tau_1^{\text{Tb}} = 0.74 \pm 0.25$  ps), irrespective of the difference in spin-orbit coupling.

These times are shorter than reported for Gd/Fe multilayers [28] where 2 ps laser pulses were used for the investigation. Moreover, these observations are similar to

## 4.1 Magnetization dynamics investigated by XMCD

---

reports on TbFe alloys [32]. Note that these observations are not compatible with demagnetization via superdiffusive spin transport [26]. The ultrafast component of the demagnetization is 50 % of the total loss in magnetization and thus too large to be explained by the transport of  $5d$  electrons. Since they are clearly longer than the pulse durations, the coherent processes suggested in Ref. [24] are also ruled out.

For comparison, the current experimental observations are partially in agreement with the theoretical model by Koopmans et al. [37] (M3TM). The obtained results show that both Gd and Tb exhibit a two step demagnetization following fs laser excitation. However, it is observed that the orbital momentum of the  $4f$  shell cannot be ignored. Ref. [37] does not consider direct spin-lattice coupling, shown here to be essential, and predicts a figure of merit for the demagnetization time that is proportional to the ratio of Curie temperature and magnetic moment  $T_C/\mu_{\text{at}}$ . Applying this to Gd ( $T_C = 293$  K,  $\mu_{\text{at}} = 7.55 \mu_B$ ) and Tb ( $T_C = 225$  K,  $\mu_{\text{at}} = 9.34 \mu_B$ ) suggests that demagnetization in Gd is faster than in Tb by a factor of 1.6. Even within our conservative error bars our observations cannot support this estimation; the non-equilibrium demagnetization times coincide for Tb and Gd. Furthermore these times are comparable with the time scale of electron-phonon equilibration [27]. It is therefore considered that the time interval during which the non-equilibrium demagnetization process is active is determined by electron-phonon interaction. The observation of similar  $\tau_1$  for Gd and Tb is more than plausible since the sub-systems of valence electrons and crystal lattice are widely comparable for Gd and Tb. This is further investigated in chapter 6 to understand whether the dynamics on this time scale is merely described by electron-phonon equilibration or some other contribution also plays a role.

From these experimental results it is concluded that the demagnetization of the localized  $4f$  moments can be changed in the sub-picosecond time scale contrary to the well known spin-lattice relaxation [33]. The characteristic timescale of  $\tau_1 = 0.75 \pm 0.25$  ps for the  $4f$  demagnetization demonstrates that after optical excitation the  $4f$  angular momentum is dissipated on a much faster timescale than equilibrium spin-lattice relaxation  $\tau_{SL}$  [33]. Since we probe the total  $4f$  angular momentum along the x-ray incidence direction [122], the 27 % drop in figure 4.3 corresponds to a decrease of  $4f$  angular momentum by  $1\hbar$  ( $\approx 0.27 \cdot (7/2) \hbar$ ). Suppose this  $4f$  angular momentum change is compensated by the conduction electrons, the  $5d6s$  angular momentum should increase. Since the equilibrium value of  $5d6s$  is  $0.55 \mu_B$ , an increase by  $1\hbar$  would mean

#### 4. Laser-induced magnetization dynamics of Gd and Tb metals

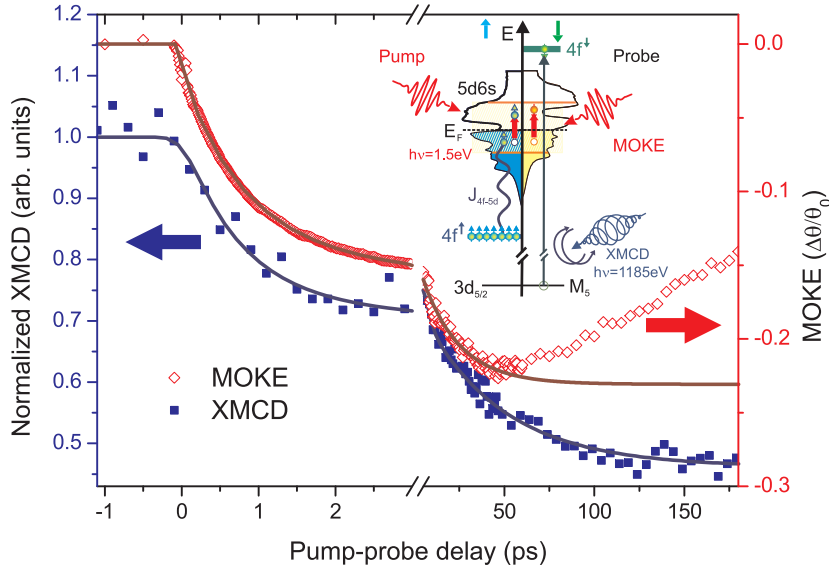


**Figure 4.4:** Time-dependent MOKE signals from Gd(0001) following fs laser excitation at equilibrium temperature  $T_0 = 140\text{K}$ . The diamonds show the experimental results and lines are double exponential fits. For comparison, the dynamics investigated by the time-dependent XMCD is shown by solid squares. Both MOKE and XMCD show the similar dynamics even at sub-ps time scale. In MOKE, recovery of the magnetization starts earlier due to faster heat flow from the crystalline film to the W(110) substrate. The principle of the time-resolved MOKE and XMCD spectroscopy is highlighted in the inset.

a tripling of the initial value. To investigate this question and observe the transfer of angular momentum between the two spin systems ( $4f$  and  $5d6s$ ), the  $5d6s$  spin dynamics is probed by time-resolved magneto-optical Kerr effect with  $h\nu = 1.5\text{ eV}$  energy as discussed in the following section and also in further details in the next chapters.

#### 4.2 Comparison of the dynamics investigated by time-resolved XMCD and MOKE

After investigation of the localized  $4f$  dynamics, as a complementary technique time-resolved MOKE was used to investigate the dynamics of the conduction electron moments. The experimental details have already been discussed in section 3.1.3. In brief, for all-optical experiments a 20 nm epitaxial Gd(0001) film, grown onto a W(110) substrate, was used to reduce the diffuse light scattering background in MOKE [7]. Here we investigated a film thickness of 20 nm, ensuring a single domain state of the sample

## 4.2 Comparison of dynamics probed by MOKE and XMCD

**Table 4.1:** Summary of results obtained using time-resolved XMCD and MOKE at  $T_0=140$  K.

Technique	Material	$\tau_1/\text{ps}$	$\tau_2/\text{ps}$
XMCD	Gd	0.76 (0.25)	40 (10)
	Tb	0.74 (0.25)	8 (3)
MOKE	Gd	0.84 (0.10)	28 (8)

[61, 126]. The magneto-optical Kerr rotation ( $\theta$ ) and its pump induced change ( $\Delta\theta$ ) were recorded using a balanced diode detection scheme with open as well as blocked pump using a chopper operating at 500 Hz. The estimated absorbed pump fluence was  $1 \text{ mJ/cm}^2$ .

The magnetization dynamics investigated by time-resolved MOKE at the equilibrium temperature of 140 K is presented by red diamonds in figure 4.4. The solid line shows the fit of the data with a double exponential function. The maximum decrease in the time-resolved MOKE signal is about 25 % following optical excitation. The dynamics can be separated into different temporal regimes. An ultrafast drop in the MOKE signal within few ps after laser excitation, on the time scale when optically excited electron transfer their energy to the lattice [41], which is followed by a slower demagnetization related to the spin-lattice relaxation, as discussed in the earlier section. After heat had been transferred to the substrate, the recovery of the magnetization starts around 40 ps and continued to 500 picosecond.

For comparison, the time-resolved XMCD results are also shown by blue squares in figure 4.4. It is evident from the experimental results that the time-resolved MOKE reproduces the general features observed by XMCD. This means that the  $4f$  and  $5d6s$  spin systems show the concomitant demagnetization even at the time scale of sub-picoseconds. The fast time scale of the demagnetization  $\tau_1 = 0.84 \pm 0.1 \text{ ps}$ , obtained by exponential fit to the time-resolved MOKE results, is also comparable to the one obtained from XMCD within the error bars if the excitation conditions (fluence) and a different sample geometry is considered. The recovery of the magnetization, in MOKE results, starts earlier in the case of the crystalline film on the tungsten substrate due to a faster heat flow from the investigated region to the tungsten substrate. Please note that the study of Gd by XMCD was performed in transmission mode and therefore, a free standing Al substrate was used which only allows the lateral flow of heat and

#### 4. Laser-induced magnetization dynamics of Gd and Tb metals

---

hence the recovery of magnetization is delayed in this case. The time scale of the slower demagnetization observed by MOKE is affected by the recovery of magnetization which is further analyzed by considering the recovery of magnetization and is discussed in chapter 5.

The study of magnetization dynamics by XMCD and its comparison with the time-resolved MOKE results show that the  $5d6s$  and  $4f$  spin systems couple strongly to each other and show the concomitant demagnetization on the picosecond time scale. As polycrystalline films are investigated by XMCD and epitaxial films by MOKE, it is concluded that the sample crystallinity do not affect the non-equilibrium demagnetization. The quasi-equilibrium demagnetization, on the other hand, is slightly faster in the epitaxial films as compared to the polycrystalline one. This is reasonable because anisotropy of the system could increase in the crystalline structure. This study also confirms that the MOKE, which probes the magnetization of the conduction electrons, can be safely used to study the magnetization dynamics down to sub-picosecond time scale. However, as it is discussed in chapter 6, the MOKE signal may suffer from non-magnetic effects [17] within few hundred femtoseconds following optical excitation when the whole system is in a strong non-equilibrium state.

To explain the behavior of ultrafast demagnetization a mechanism [58] is proposed which speeds up the spin-lattice relaxation. The  $4f$  and  $5d$  moments are strongly coupled by intra-atomic exchange with energy of about 700 meV [52], which provides the possibility of spin transfer from the  $4f$  shell to the conduction band. By means of the  $4f$ - $5d$  coupling a spin-flip scattering process in the conduction band affects the  $4f$  electrons as well and drives the ultrafast demagnetization via indirect spin-lattice coupling. Time-resolved magneto-optical Kerr effect (MOKE) experiments which probe primarily the conduction band spin polarization, demonstrate a reduction of the MOKE signal concomitant with the XMCD one. From the comparison of XMCD and MOKE a mere transfer and accumulation of angular momentum in the conduction band can be excluded on the time scale of few ps. However, the accumulation of angular momentum in the conduction electron cannot be ruled out at even faster time scales as will be addressed in the next chapter.

Let us then come back to the general discussion of demagnetization dynamics of both lanthanide elements Gd and Tb. Interestingly, in both  $4f$  elements the quasi-equilibrium demagnetization time is similar. Although this effect is significantly faster

## 4.2 Comparison of dynamics probed by MOKE and XMCD

---

than the previously known spin-lattice relaxation [33], it is still considerably slower than the observed demagnetization time in the itinerant ferromagnets [13, 37, 40]. The possible reason for this difference is the indirect exchange coupling and localized magnetization of lanthanide ferromagnets. In contrast to itinerant ferromagnets, where the laser excited electron can also contribute to magnetization, the dominant part of magnetization in lanthanides is generated by the  $4f$  electrons and is considerably larger for Gd and Tb than for Fe, Co, and Ni. Thereby, during the transfer of angular momentum from the magnetization to the lattice, several spin flips in the conduction band are required to obtain the same relative demagnetization as in  $3d$  ferromagnets, where the magnetic moment resides completely in the conduction band and is much smaller. This is why in both  $4f$  elements the ultrafast process lasts longer than in the  $3d$  transition metals [13, 37, 40].

After the confirmation of the reliability of MOKE and its frequent availability in lab, as opposed to synchrotron based XMCD technique, we had the opportunity to investigate the dynamics in further detail which will be discussed in the following chapters.

## Summary

In this chapter it is shown that magnetization dynamics of the  $4f$  moments in Gd, investigated by time-resolved XMCD technique following the fs laser excitation, proceeds in two temporal regimes: the quasi-equilibrium and the non-equilibrium. The study of the dynamics of Gd and Tb helps to analyze the two regimes in more detail. From the comparison of the dynamics of Gd and Tb, it is observed that in the quasi-equilibrium regime the demagnetization time in Tb is smaller than in Gd, due to the magneto-crystalline anisotropy which is much stronger in Tb than in Gd. On this basis it is concluded that the quasi-equilibrium demagnetization is defined by the equilibrium spin-lattice relaxation. The non-equilibrium demagnetization timescale is comparable for both Gd and Tb and shows a pronounced enhancement of the conduction electron-mediated indirect spin-lattice relaxation, which is about 50 times faster than the previously known spin-lattice relaxation of Gd [33], and proceeds at the time scale of electron-phonon equilibration.

#### 4. Laser-induced magnetization dynamics of Gd and Tb metals

---

In addition to the dynamics of localized  $4f$  moments, the magnetization dynamics of  $5d6s$  conduction electrons of Gd is also investigated using the time-resolved MOKE technique. A comparison of the dynamics investigated by these two techniques gave details about the angular momentum transfer as well as the intra-atomic exchange interaction. Interestingly, both  $4f$  and  $5d6s$  moments show similar dynamics down to sub-picosecond time scales. These findings demonstrate that the  $4f$  angular momentum change is not redistributed among the spin sub-systems, but must be transferred to the lattice with a time constant of less than 1 ps. In fact, the concomitant demagnetization of the localized and itinerant spin system also provides experimental evidence for the strong coupling of both spin systems in Gd [52]. Moreover, the comparison of the MOKE results with the XMCD suggests that MOKE can be used as a reliable probe of magnetization dynamics down to sub-picosecond time scale. Therefore, time-resolved MOKE is employed to obtain insights in the observed two-step demagnetization and disentangle different microscopic processes, which will be presented in the following chapters.



## 5

# Temperature-dependent quasi-equilibrium magnetization dynamics of Gd investigated by TRMOKE

In the previous chapter it was shown that the time-resolved MOKE successfully reproduces the magnetization dynamics observed by time-resolved XMCD. This allows us to use the time-resolved MOKE to investigate the magnetization dynamics in more detail. Initially a detailed equilibrium temperature ( $T_0$ ) dependence of magnetization dynamics is analyzed focusing on the quasi-equilibrium regime. It should be noted that the quasi-equilibrium means that the electron and phonon temperatures are already equilibrated at this time scale ( $t \gg 1ps$ ).

In this chapter I will discuss the laser-induced demagnetization of Gd and the recovery of magnetization thereafter, investigated using time-resolved MOKE from several picoseconds to a few hundred picoseconds. The detailed temperature-dependent magnetization dynamics and a comparison of the experimental results with recent theoretical models is presented in section 5.1. At the end of the chapter the temperature dependence of the recovery of magnetization is discussed.

## 5. $T_0$ dependent quasi-equilibrium magnetization dynamics

---

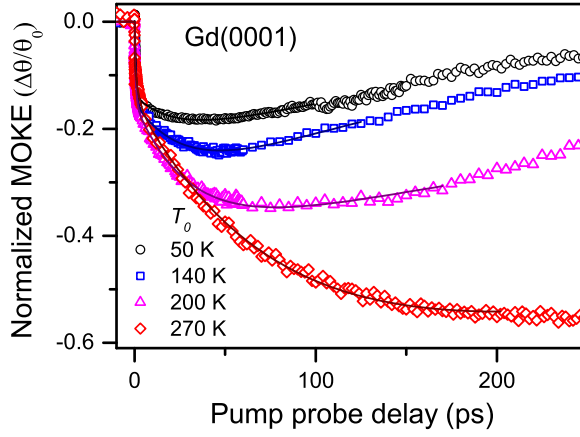


**Figure 5.1:** Laser-induced change in the magneto-optical Kerr rotation signal normalized to the respective equilibrium values for 20 nm Gd(0001)/W(110) measured at different equilibrium temperatures  $T_0$ . Symbols show experimental results and lines show the exponential fit. Both demagnetization amplitude and time delay at minimum magnetization increase as temperature rises.

### 5.1 Influence of temperature on quasi-equilibrium magnetization dynamics

As discussed in chapter 3 the time-resolved MOKE measurements were performed on epitaxial Gd films which were prepared on a W(110) substrate in an ultrahigh vacuum (UHV) chamber. The magneto-optical Kerr rotation ( $\theta$ ) and its pump induced change ( $\Delta\theta$ ) were recorded with open as well as blocked pump using a chopper operating at 500 Hz, as described in section 3.2. The temperature dependent measurements were performed in nominally constant absorbed pump fluence of about  $1 \text{ mJ/cm}^2$ . For temperature-dependent measurements the sample was cooled below 50K with a liquid He cryostat and the temperature was controlled through resistive heating. To monitor the sample temperature, a WRe thermocouple attached directly to the W(110) substrate was used. The time-dependent Kerr rotation was recorded for different equilibrium temperatures  $T_0$  from 50 K to 290 K. Since the absolute value of magnetization and hence the MOKE signal changes with temperature, the pump-induced change  $\Delta\theta$  was normalized to the total MOKE signal  $\theta_0$  before pump excitation in order to compare the transients at different temperatures. In this way one can also minimize the effects of changing laser intensity in different experiments.

## 5.1 Influence of temperature on quasi-equilibrium magnetization dynamics

Figure 5.1 shows the change in the normalized MOKE rotation as a function of pump-probe delay for different  $T_0$ . As already discussed in section 4.2, the curves show a fast decrease within 3ps, followed by the slower decrease from 3 to few 100 ps and then the recovery of the signal which starts around 60 ps. As a function of the equilibrium temperature three effects can be observed right away. Firstly, the maximum drop in magnetization increases from about 15 % at 50 K to 55 % at 270 K. Secondly, the demagnetization continues to longer time delays as temperature rises. Thirdly, the recovery of magnetization, which also starts at longer time delays as temperature increases, above 270 K the transients do not recover in the investigated time domain of 500 ps. To quantitatively determine the demagnetization time and amplitude of demagnetization, the time-dependent experimental MOKE results are analyzed using a tri-exponential fit of the form

$$\Delta\theta/\theta_0 = \{\Delta M_1/M_0(1 - e^{-t/\tau_1}) + \Delta M_2/M_0(1 - e^{-t/\tau_2})\} \times e^{-(t-t_0)/\tau_r} + C_0. \quad (5.1)$$

The first part in above equation represents the ultrafast demagnetization (non-equilibrium) within few ps after laser excitation with demagnetization amplitude  $\Delta M_1/M_0$  and time  $\tau_1$  while the quasi-equilibrium demagnetization from several to hundreds of ps is represented by the second part with amplitude  $\Delta M_2/M_0$  and demagnetization time  $\tau_2$ . In order to account for the recovery of magnetization, the third exponential function is included with the recovery time  $\tau_r$ . The step function within the initial few hundred femtoseconds is considered in  $C_0$ , as will be discussed in section 6.3.

Before going into a detailed discussion of quasi-equilibrium magnetization dynamics, it is important to note that the dynamics within few hundred femtoseconds may be affected by the optical artefacts. This is concluded from the different behavior of the MOKE rotation and ellipticity (figures 6.4 and 6.5 in the next chapter) when energy is accumulated in the electronic sub-system after optical excitation. Therefore, detailed analysis is required to extract the pure magnetization at non-equilibrium time scale and will be addressed in chapter 6.

The demagnetization amplitude as a function of temperature, determined by fitting the time-dependent Kerr rotation, is shown in figure 5.2. The demagnetization amplitude  $\Delta M_2/M_0$  increases from 7 % at  $T_0 = 50K$  to about 60 % at 290K. The slope

## 5. $T_0$ dependent quasi-equilibrium magnetization dynamics

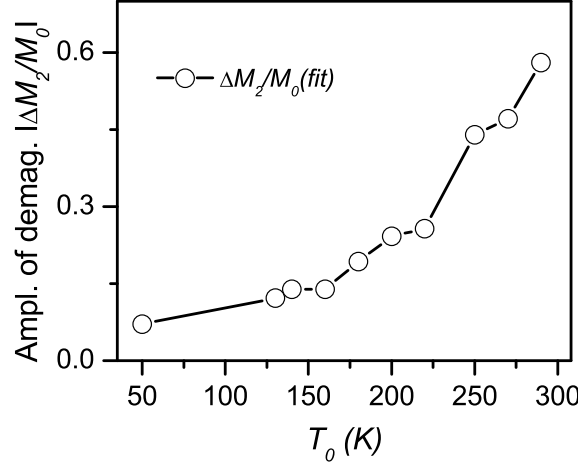


**Figure 5.2:** Amplitude of demagnetization as a function of temperature. The symbols show the values obtained by fitting (equation 5.3) the transient MOKE results (line is guide to the eye). The amplitude of the demagnetization increases with temperature changing slope close to Debye temperature of 163 K.

$(\partial(\Delta M_2/M_0)/\partial T_0)$  changes in the vicinity of 163 K, which is the Debye temperature  $\Theta_D$  of Gd. The steady increase and changing slope of the amplitude of demagnetization close to  $\Theta_D$  indicates that phonons are contributing to the amplitude of demagnetization. In order to compare the demagnetization amplitude as a function of temperature, the change in the MOKE signal was also measured in a single experiment with increasing temperature at different fixed delays of 0.1, 3 and 60 ps. In this way it was ensured that excitation conditions were the same.

A qualitative discussion of the equilibrium temperature dependence of magnetization is presented here to understand the demagnetization amplitude. The magnetization of Gd decreases with increasing temperature  $T_0$  (as shown in figure 2.3 in chapter 2), however, the rate of change of this decrease ( $|\partial M/\partial T_0|$ ) will be larger at a higher  $T_0$ . On the other hand the laser-induced change in the lattice temperature ( $\Delta T$ ) depends on the specific heat. The specific heat of Gd also increases with  $T_0$  (as shown in figure 2.3) which will decrease the  $\Delta T$  at higher temperatures (provided that the excitation laser fluence is constant). Above Debye temperature, while increasing  $T_0$  further, change in the lattice temperature  $\Delta T$  will no more decrease unless critical fluctuations are excited. This competition between change in magnetization  $|\Delta M(T_0)|$  and change in lattice temperature  $\Delta T$  defines the temperature dependence of the demagnetization amplitude.

## 5.1 Influence of temperature on quasi-equilibrium magnetization dynamics

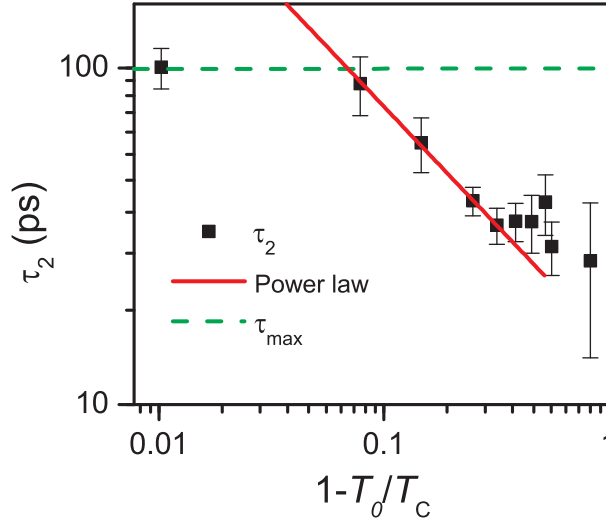


**Figure 5.3:** Double logarithmic plot of demagnetization time as a function of reduced temperature  $r=1 - T_0/T_C$ . Symbols are experimental results fitted with a power law as shown by red solid line. The power law fits the experimental data nicely with  $\omega = 0.70 \pm 0.08$ . Due to the finite time effects the value of  $\tau_2$  saturates to maximum value  $\tau_{\max}$  (shown by dashed line) close to  $T_C$ .

In the following I will discuss the temperature dependence of the demagnetization time  $\tau_2$ . Figure 5.3 shows the double logarithmic plot of  $\tau_2$  as a function of reduced temperature which is defined as  $r=1 - T_0/T_C$  (demagnetization time as a function of temperature on a linear scale is shown in figure 5.5).  $\tau_2$  increases 4 times as temperature rises from 50 K to 290 K. The demagnetization time is nominally constant at low temperatures, but increases strongly as  $T_0$  approaches the Curie temperature. Very close to  $T_C$  the demagnetization time saturates to a maximum value. The strong increase in  $\tau_2$  as temperature approaches  $T_C$  suggests to us an analysis of such behavior by a power law, as discussed in the following section.

### 5.1.1 Critical slowing down in the demagnetization

The pronounced change in the magnetic properties near  $T_C$  is usually attributed to an increase in the spin fluctuations and hence a phenomenon known as *critical slowing down* (as described in section 2.1.3). For the study of magnetization dynamics, the relevant quantity is the spin fluctuation time  $\tau$  which follows a power law [56]

$$\tau \propto |r|^{-\omega} \quad (5.2)$$

## 5. $T_0$ dependent quasi-equilibrium magnetization dynamics

---

where  $r=1 - T_0/T_C$  is the reduced temperature and  $\omega = \nu \cdot (z - 1.06)$ ;  $\nu$  and  $z$  denote the critical exponent of the correlation length and the dynamical critical exponent, respectively. The theoretically predicted value of  $\omega$  for Gd, on the basis of the Heisenberg model, was 0.72 [56]. This behavior is well-known for relaxation of the system towards its equilibrium value after a perturbation. The slowing down of the recovery of magnetization observed in this experiment (figure 5.1) can be related to a similar phenomenon. However, in addition to the relaxation of magnetization in the current study we observed a similar behavior of the laser-induced demagnetization time, while the ferromagnet is driven out of the equilibrium magnetization by excitation through an external stimulus laser pulse. Figure 5.3 (solid squares) shows the experimentally measured demagnetization time as a function of reduced temperature in a double logarithmic plot. The demagnetization time increases four times for  $0.01 < r < 0.8$ . The effect becomes more pronounced as  $T_0 \rightarrow T_C$ . An approximately linear dependence of  $\tau_2$  on reduced temperature is found for the range  $0.078 < r < 0.31$ , indicating the power law dependence of the demagnetization time. The value of the critical exponent derived from the power law analysis of the experimentally determined demagnetization time is  $\omega = 0.70 \pm 0.08$ . We observed that the  $\tau_2$  deviates from the power law for the temperature values very close to  $T_C$ ,  $r < 0.078$ .  $\tau_2$  saturates to a value of  $\tau_{max} \approx 100$  ps as temperature approaches  $T_C$ . One potential reason for this can be the recovery of magnetization. In pump-probe experiments it becomes obvious that the recovery of magnetization competes with the demagnetization. At very long delays after heat transport to the substrate the recovery is dominant. As a result demagnetization for infinite time is not expected.

The value of the exponent  $\omega$  for the spin fluctuation time in Gd has been a topic of discussion for the last three decades [56, 127, 128, 129, 130]. Using Mössbauer and spin resonance techniques, the observed value of  $\omega = 0.5$  for autocorrelation time, was smaller than theoretical predictions of 0.7 [56, 127]. Note that this value of  $\omega$  was determined for Gd in the paramagnetic phase above  $T_C$ . The small value of  $\omega$  was explained by Frey et al. by considering the combined effects of dipolar interaction and uniaxial anisotropy [128, 129, 130]. The authors suggested that a crossover from pure Heisenberg to dipolar critical behavior occurs at  $T - T_C = 10K$ . Very close to  $T_C$  anisotropy results in further reduction of  $\omega$ . The value of  $\omega = 0.7$  measured in our experiment is larger than the previous experimental observations [56, 127]. Furthermore,

## 5.1 Influence of temperature on quasi-equilibrium magnetization dynamics

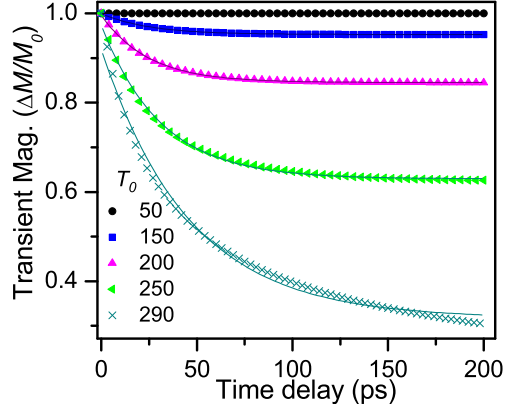


**Figure 5.4:** Time-dependence of the demagnetization transients calculated using M3TM for different equilibrium temperatures  $T_0$ . The symbols show the results of M3TM calculations and the lines are fits of an exponential function to determine the demagnetization time. The calculations are made for  $T_e = T_l$  and parameters from Ref. [37].

this value is also larger than the mean field value of 0.5 [131], but is consistent with the theoretical values [129], suggesting Heisenberg-like critical behavior for Gd with dipolar contributions. Since the value of  $\tau_2$  at 290K deviates from the single power law, in addition to finite time effects originating from the recovery of magnetization as described above, we cannot rule out the crossover from Heisenberg to dipolar behavior [129] at high temperatures very close to  $T_C$ .

This analysis confirms that the strong increase in demagnetization time can be explained by a power law with the critical exponent  $\omega$ . Therefore, the significant increase in the quasi-equilibrium demagnetization time as a function of temperature is attributed to the critical slowing down.

### 5.1.2 Comparison with the theoretical models

In this section a comparison of the experimental observations with different theoretical models is presented. Recently Koopmans et al. published a phenomenological microscopic three-temperature model (M3TM) [37] which is based on phonon mediated Elliott-Yafet (EY) type spin flip scattering, which is already discussed in section 2.3.2. The authors explain the two step demagnetization of Gd and related it to the phonon mediated EY scattering rate (as discussed in section 4.1 and in Ref. [37]). In order to compare it with our experimental results, we estimated the time-dependence of demag-

## 5. $T_0$ dependent quasi-equilibrium magnetization dynamics

---

netization as a function of equilibrium temperature using M3TM with  $T_e = T_l$ ,  $s=1/2$ <sup>1</sup> and a constant value of  $R=0.092 \text{ ps}^{-1}$  [37]. The time-dependent evolution of magnetization based on these calculations is shown by symbols in figure 5.4. Qualitatively, the transient behavior is similar to our experimental observations. For quantitative comparison, these transients are fitted by an exponential function to determine the demagnetization time, shown by solid lines in figure 5.4. The resulting demagnetization time is shown by a red dashed line in figure 5.5. The value of demagnetization time suggested by M3TM concurs with our experimental observation at intermediate temperatures. Contrary to our experimental observations, however, at low temperatures the M3TM model predicts a decrease in the demagnetization time with increasing temperature, due to increasing phonon population. At high temperatures  $T_0/T_C > 0.7$ , M3TM suggests a slight increase in the demagnetization time from 30 to 50 ps. The increase in the demagnetization time as predicted by M3TM is smaller than the experimentally observed values. As M3TM does not take the spin fluctuations into account, it deviates from the experimental results at high temperatures as well. It should be mentioned that the M3TM with  $s=7/2$  (not shown here), which in principle should be more appropriate for Gd, shows much stronger and faster demagnetization than the experimental observations. This suggests that the spin-flip probability constant suggested in M3TM [37] may require careful reconsideration in order to reproduce the experimental observations.

A second theoretical approach suggested to demonstrate the ultrafast demagnetization is based on the Landau-Lifshitz-Bloch (LLB) equation [34, 132, 133], as discussed in section 2.3.3. Using this model, the temperature dependence of the longitudinal relaxation time was calculated [36, 133]. A slowing down of the demagnetization time was reported as the system approaches Curie temperature. The results of the relaxation time calculated by Chubykalo-Fesenko et al. using the LLB model [36] are shown by the dotted line in figure 5.5. Since the model calculations were made for a general case, the calculated values of demagnetization time are multiplied by 10 to compare with the experimental results. This is reasonable as the magnetic order of Gd is due to indirect exchange as well as spin-orbit coupling; therefore, the spin-lattice relaxation time in Gd is longer than in direct (itinerant) ferromagnets (as discussed in chapter

---

<sup>1</sup>The Gd is a  $s=7/2$  system. For simplicity and to see the temperature dependence of demagnetization,  $s=1/2$  is used for these calculations as suggested in the M3TM model [37].



## 5.1 Influence of temperature on quasi-equilibrium magnetization dynamics

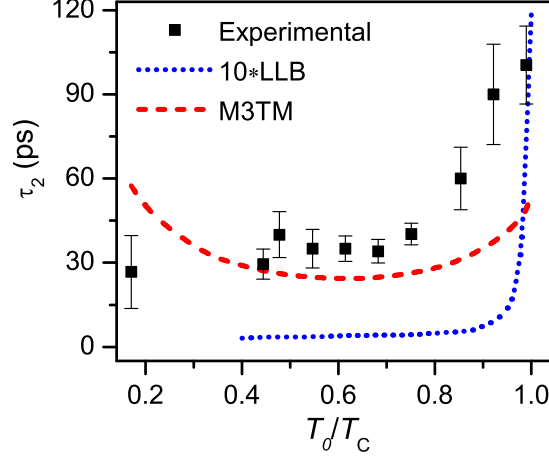


**Figure 5.5:** Comparison of experimental demagnetization time ( $\tau_2$ ) with theoretical model calculations as a function of normalized equilibrium temperature  $T_0/T_C$ . Symbols represent the experimental results, the dashed line shows the demagnetization time calculated by M3TM and the temperature dependence of demagnetization rate from the LLB model is shown by the dotted line. LLB model calculations are taken from Ref. [36].

4) [58]. Although the absolute value of the relaxation time does not match our experimental results, with its simple general form the theory predicts the divergence of the relaxation time near  $T_C$  which is also observed experimentally. As discussed in section 2.3.3, according to the LLB calculations the competition between increase of both longitudinal damping rate and magnetic susceptibility defines the temperature dependence of the demagnetization time. At high temperatures critical fluctuations contribute to the longitudinal susceptibility which diverges near  $T_C$  and results in slowing down of the demagnetization time. Another point to note is the earlier increase in the experimentally measured time  $\tau_2$  at about  $T_0 = 0.8T_C$  compared with the LLB model. In a pump-probe experiment one expects the rise in the lattice temperature within few picoseconds [27] which can excite the critical fluctuations even if the equilibrium temperature before excitation is significantly lower than  $T_C$ . This is the reason for the broad critical region observed in this experiment.

To summarize this part, although both M3TM and LLB models qualitatively show the demagnetization similar to our experimental observations, in details our temperature-dependent experimental results are not reproduced with either of these models. M3TM predicts the value of demagnetization time which coincides with our experimental values, however, the temperature dependence is different from the experimental observa-

## 5. $T_0$ dependent quasi-equilibrium magnetization dynamics

---

tions. On the other hand the LLB model shows the divergence of demagnetization time at  $T_C$ , however, the absolute value of demagnetization is different and suggests that more specific parameters related to Gd must be considered for a detailed comparison. In addition to fundamental mechanisms considered in these models, as responsible for demagnetization, the consideration of a temperature-dependent coupling to the bath parameter in the LLB model and spin-flip scattering rate in M3TM may improve the calculations. In the LLB model this task is successfully achieved in non-equilibrium demagnetization which is discussed in chapter 6. Furthermore, the electronic band structure is also not considered in either of these models.

According to the calculations of Hübner and Bennemann, as shown in equation 2.23 (in chapter 2), the spin-lattice relaxation time consists of two important terms: phonon population and spin-orbit coupling. Owing to well-defined temperature dependence of phonon population one can expect the decrease in the  $\tau_{S-L}$  with increasing temperature assuming a constant spin-orbit coupling. However, this is not observed experimentally and the demagnetization time  $\tau_2$  weakly changes as a function of  $T_0$  except close to  $T_C$ . This suggests that the spin-orbit coupling decreases and hence  $\tau_{S-L}$  increases in such a way that it competes with the decrease in the  $\tau_{S-L}$  with increasing phonon population.

One of the most important conclusion from our experimental results is that the spin-fluctuations contribute to the quasi-equilibrium demagnetization of Gd hence demagnetization follows the critical slowing down. Furthermore, experimental observations suggest that the demagnetization amplitude changes due to the phonons while the time scale of demagnetization is not strongly affected by them. The possible origin of this effect could be the spin-lattice relaxation bottleneck.

### 5.2 Recovery of magnetization

Another interesting aspect of the experimental results discussed in the earlier section is the recovery of magnetization. Figure 5.6 represents the time-resolved MOKE signal for different temperatures for a long time range of up to 500 ps. The recovery of magnetization starts at about 60 ps at 50 K and finishes at 400-500 ps. At higher temperatures demagnetization starts at longer time delays and the signal does not recover in the investigated time for temperatures above 270 K. The recovery dynamics is also complex and may not be described by simple exponential dependence for the whole

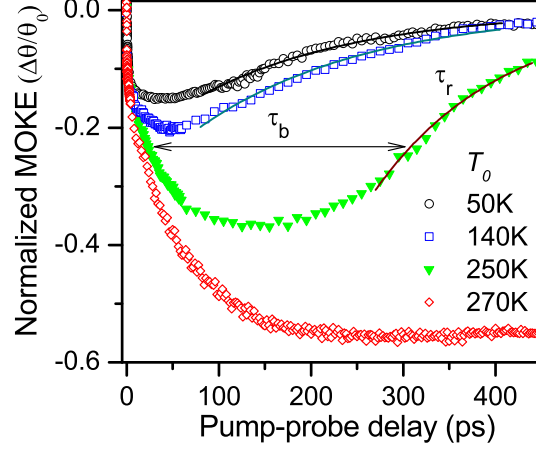


**Figure 5.6:** Transient MOKE curves after femtosecond laser excitation as a function of pump-probe delay for different equilibrium temperatures, emphasizing the recovery of magnetization. Symbols show the experimental results and lines are exponential fits to extract the magnetization recovery time  $\tau_r$ . The curves show a slowing down of the recovery as well as broadening of magnetization transients as a function of temperature.

time range. Two effects can be clearly observed in the temperature-dependent recovery of the magnetization. One is the broadening of the MOKE transients as temperature increases and the second is the recovery of magnetization itself. To estimate the characteristic time of magnetization recovery  $\tau_r$ , time-dependent rotation results are fitted by an exponential function for a selected time range at long delays.

$$\Delta\theta/\theta_0 = \Delta M/M_0(e^{-(t-t_0)/\tau_r}), \quad (5.3)$$

where  $\Delta M/M_0$  represents the amplitude and  $\tau_r$  the time of magnetization recovery with offset  $t_0$ . All the parameters are kept free during fitting. The broadening time  $\tau_b$  is determined by the width of the transients at half of the maximum drop in the signal.

The recovery time weakly changes as a function of temperature within the experimental error bars as shown in figure 5.7. On the other hand the broadening increases from 140 ps at 50 K to 280 ps at 250 K, however, the change in time is more pronounced above 150 K. The weak dependence of the recovery time  $\tau_r$  on temperature can be explained in a similar way as the demagnetization time  $\tau_2$  (previous section). It is suggested that the increase in the phonon population and decrease in the spin-orbit coupling results in a very weak change of spin-lattice relaxation time with temperature. However, the potential reason for the increase in the broadening time could be the com-

## 5. $T_0$ dependent quasi-equilibrium magnetization dynamics

---

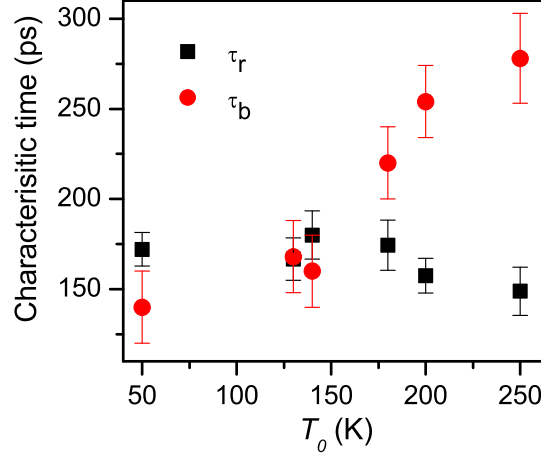


**Figure 5.7:** Magnetization recovery time as a function of temperature (squares). Circles show the temperature dependence of the  $\tau_b$ , the broadening of the magnetization transients. Magnetization recovery time weakly changes while  $\tau_b$  increases with increasing temperature after 150 K.

bined effect of spin fluctuations and the spin-lattice relaxation. More spin fluctuations will contribute to magnetization close to the Curie temperature which will result in an increase in the broadening (critical slowing down). However, as the broadening starts to increase in the vicinity of the Debye temperature of Gd, the contributions of spin-lattice relaxation may not be ignored.

Magnetization recovery is not observed at all for temperatures above 270 K up to the measured range of 500 ps, which in principle is also the critical slowing down of relaxation of magnetization as discussed in section 5.1.1. This experimental behavior is in agreement with the theoretical calculations, where magnetization recovery slows down with increasing pump laser fluence [134], which suggest that the recovery of the exchange interaction takes longer with a rise in the temperature. Such behavior has also been predicted in theoretical calculations for the recovery of magnetization at higher laser fluence [132, 135]. The increase in the recovery time was attributed to the critical slowing down [132] and reduction of spin-orbit coupling [135], the latter is inversely proportional to the temperature [33].

From the temperature-dependent demagnetization it is concluded that both the spin-orbit coupling and critical spin fluctuations contribute to the recovery of magnetization and broadening of demagnetization transients, respectively.

The divergence of the amplitude (or total demagnetization to zero) is not observed

close to  $T_C$  which suggests that the specific heat increases enormously in the excited state of the system. The strong increase in the specific heat results in a decrease in pump-induced change of the lattice temperature and hence full demagnetization (-1 in figure 5.6) is not observed even very close to  $T_C$ . The competition between demagnetization and the recovery may also result in the broadening and the limited demagnetization even very close to the Curie temperature.

### 5.3 Summary

The role of the phonons and critical spin fluctuations in the laser-induced magnetization dynamics is discussed by investigating the temperature-dependent magnetization dynamics of Gd from 50 K to Curie temperature. An observation of the critical fluctuations in quasi-equilibrium demagnetization near the ferro- to paramagnetic phase transition is made in a time-resolved experiment.

The experimental results suggest that the phonons play a dominant role in the amplitude of demagnetization while the demagnetization time slightly changes as  $T_0$  increases at low temperatures. This weak dependence could be due to the spin-lattice relaxation bottleneck defined by the competition between the spin-orbit coupling and phonons. A strong increase of the demagnetization time is observed as the system approaches the Curie temperature. After power law analysis, these effects are attributed to the critical slowing down. By analyzing the recovery dynamics as a function of  $T_0$ , two contributions are discerned: the recovery of the magnetization and the broadening of the transients which are explained as the consequence of spin-orbit coupling and spin fluctuations, respectively.

The experimental results are compared with the theoretical calculations based on the M3TM and LLB models. It is found that in details the experimentally measured demagnetization time shows different temperature dependence than the theoretical predictions. The M3TM model calculations give a comparable values of the demagnetization time at intermediate temperatures; however, the detailed temperature dependence differs from the experimental observations. The consideration of spin fluctuations as well as appropriate temperature dependent spin-lattice relaxation is found to be essential for the explanation of the dynamics. On the other hand, the LLB predicts the

## 5. $T_0$ dependent quasi-equilibrium magnetization dynamics

---

contribution of spin fluctuations to demagnetization; however, material-specific conditions must be considered for the correct description of demagnetization on the basis of the LLB model.

## 6

# Non-equilibrium magnetization dynamics investigated by TRMOKE

Ferromagnetic Gd features two separate demagnetization regimes following femtosecond laser excitation as discussed in chapter 4. These two regimes are: (i) quasi-equilibrium, where demagnetization is determined by the equilibrium spin-flip probability set by spin-lattice coupling, which has been discussed in detail in chapter 5, and (ii) non-equilibrium, of the order of electron-phonon equilibration time, which is further discussed in the present chapter. The purpose is to disentangle the different microscopic contributions in non-equilibrium regimes. Specifically it is investigated whether electron-phonon equilibration defines the ultrafast demagnetization alone or some other processes are also involved.

In this chapter I will analyze the non-equilibrium magnetization dynamics of Gd within few picoseconds following laser excitation, studied by time-resolved MOKE. The emphasis will be on the laser fluence and temperature-dependent studies. As the used wavelength is the same for the pump and probe, the time resolved MOKE signal can be affected by non-magnetic contributions at the early delays following optical excitation. Therefore, this temporal regime requires careful investigation which is achieved by measurement of both MOKE rotation and ellipticity.

In the first section the investigation of non-equilibrium magnetization dynamics as a function of laser fluence is discussed. In section [6.2](#) the temperature dependence

## 6. Non-equilibrium magnetization dynamics investigated by TRMOKE

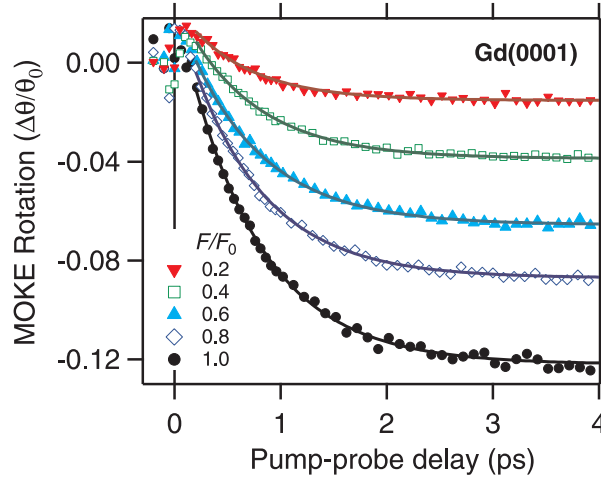


**Figure 6.1:** Time-dependence of the normalized MOKE rotation signal for different relative pump fluences  $F/F_0$ , with  $F_0 \approx 1 \text{ mJ/cm}^2$  [117]. Symbols indicate experimental data and solid lines are fits considering a single exponential decay.

of demagnetization and the theoretical modeling of the observed experimental results within the framework of the LLB model will be presented. Finally, in section 6.3 a comparison of  $5d6s$  and  $4f$  dynamics measured by time-resolved MOKE rotation and ellipticity as well as by time-resolved XMCD is presented, with emphasizing the extreme non-equilibrium dynamics within initial few hundred femtoseconds following laser excitation.

### 6.1 Laser fluence-dependent magnetization dynamics

As already discussed in chapter 5, the sample studied was an epitaxial Gd(0001)/W(110) film with 20 nm thickness deposited and investigated in ultrahigh vacuum conditions. Pump-probe experiments were performed at a 50 K equilibrium temperature of the sample. Using a combination of  $\lambda/2$  wave plate and Glan-Thomson polarizer the absorbed fluence  $F$  was reduced from the maximum value  $F/F_0 = 1$ , with  $F_0$  determined as  $1.0 \pm 0.3 \text{ mJ/cm}^2$ .

Figure 6.1 shows the time-dependence of the MOKE rotation signals for different  $F/F_0$  up to delay times of 4 ps. A clear pump-induced change is observed in the MOKE signal  $\Delta\theta/\theta_0$ . As expected the values at 4 ps decrease linearly with  $F/F_0$ . This ensures that we are analyzing a low excitation density regime reasonably far away from a full demagnetization of the sample, where magnetic fluctuations would



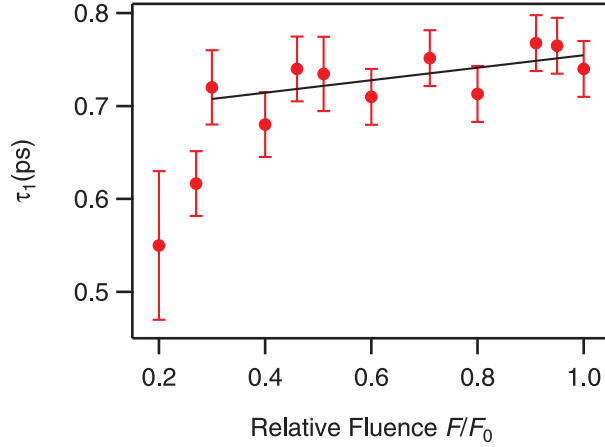


**Figure 6.2:** Characteristic demagnetization times ( $\tau_1$ ) determined by the single exponential fitting of  $\Delta\theta/\theta_0$  as a function of relative fluence [117]. The line is a linear fit to the data with  $F/F_0 \geq 0.30$

contribute to the ultrafast magnetization dynamics [132]. Near time zero, the data feature an effectively positive contribution in  $\Delta\theta/\theta_0$ . The time delay at which the signal crosses the zero line shifts closer to time zero with increasing fluence. While for  $F/F_0 = 0.2$  the amplitudes of the positive and negative contributions are comparable to each other, the negative one dominates for larger  $F/F_0$ . In this section I shall focus on the pronounced demagnetization dynamics, i.e. at those fluences where the negative contribution dominates. The dynamics within few hundred femtoseconds following laser excitation will be discussed further in the next section and at the end of this chapter. Here we will analyze the dynamics after few hundred femtoseconds to few picoseconds.

The pump-induced reduction  $\Delta\theta/\theta_0$  is fitted by a single exponential time-dependence with fixed time zero and variable vertical offset and amplitude in the temporal range of 0.2 to 4 ps. The obtained fits are shown by lines in figure 6.1 and describe the experimental data well. Figure 6.2 depicts the time constants  $\tau_1$  determined by the fitting procedure. The numbers range from about 0.5 to 0.8 ps with a trend towards larger times for higher  $F/F_0$ . The smallest  $\tau_1$  are obtained for the lowest  $F/F_0 = 0.20$  and 0.27 and deviate from the weak linear increase observed for  $F/F_0 \geq 0.30$ . As already mentioned, for such small  $F/F_0$  the positive signal near time zero is comparable in size to the demagnetization observed at later delays. It is therefore well possible that the obtained  $\tau_1$  is influenced by the processes that are responsible for the positive  $\Delta\theta/\theta_0$  which are dominant for  $F/F_0 < 0.30$ .

## 6. Non-equilibrium magnetization dynamics investigated by TRMOKE

---

A linear fit to the  $\tau_1(F)$  values for  $F/F_0 \geq 0.30$  is used and the result is represented by a line in figure 6.2. We find that the demagnetization time increases weakly by  $67 \pm 30$  fs within  $F/F_0 = 1$  with a nominal zero fluence limit of  $\tau_1 = 690 \pm 20$  fs.

For itinerant ferromagnets like Ni or Co an observed increase in the demagnetization time with fluence in combination with a finite value at zero fluence was explained by model descriptions based on Elliott-Yafet scattering [37] and Stoner excitations [132]. A fluence dependence of the ultrafast demagnetization of Gd was also predicted [37], which was determined by the increase of the transient lattice temperature. Therefore, in the following the electron-phonon equilibration based on transient electron and lattice temperatures is calculated and compared with our experimental results.

### Comparison with electron-phonon equilibration time

To calculate the time-dependence of electron  $T_e(t)$  and lattice temperature  $T_l(t)$  as well as their equilibration for different fluences, the well established two-temperature model [66] is employed. An improved version of this model was published earlier [68] (regarding its application to Gd(0001) see Ref. [27]). Considering a variation in fluence following the experimentally investigated range a pronounced quantitative increase of the time scale, on which the transient electronic and lattice temperatures equilibrate, is found. However, a systematic analysis of the time scale at which  $T_e(t)$  and  $T_l(t)$  are changed is non-trivial since they vary in a non-exponential way. Therefore, we turn instead to a discussion of the excess energy  $E_e$  of the electronic system which is related to the electron temperature through  $E_e = \gamma T_e(t)^2$ , with  $\gamma$  being the linear parameter in the temperature-dependent specific heat of the electron system. Figure 6.3 shows the calculated results for  $E_e(t)$  with  $F/F_0$  varying between 0.2 and 1. The transient behavior can be described by a single exponential that represents energy transfer from the electron system to the lattice. It should be noted that the decrease in the excess electron energy, with time, means an increase in lattice energy and hence in temperature. It can be clearly seen from the calculated fluence-dependent transients in figure 6.3 that with increasing fluence the energy stays in the electronic system longer. The relevant time scale for the energy transfer from electron to phonon  $\tau_{e-p}$  is determined by fitting  $E_e(t)$  of figure 6.3 from 100–800 fs (an exemplary fit is included at  $F/F_0 = 0.6$  as a thick solid line). The resulting values of energy transfer time from electrons to phonons  $\tau_{e-ph}$  are plotted in the inset of figure 6.3. The energy

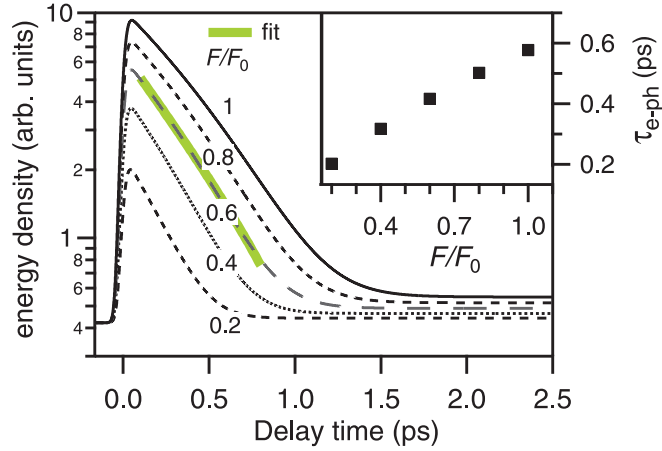


**Figure 6.3:** Main panel: Time-dependent excess electronic energy density for different relative fluence [117], calculated by the two-temperature model. The inset shows the characteristic times  $\tau_{e-ph}$  of energy transfer from the electronic system to the lattice mediated by electron-phonon scattering which is determined by single exponential decay to the excess energy density in time interval of 100 to 800 fs.

transfer time shifts to larger values for higher fluence and increases by three times in the investigated fluence range.

The comparison between the time-dependent demagnetization curves and the time evolution of excess energy emphasizes two points which lead to the conclusion that the explanation of the ultrafast demagnetization in Gd solely through the time-dependent electron or lattice temperature is incomplete. Firstly, we argue that the range of the energy transfer times  $\tau_{e-ph}$  found in the investigated fluence range is with 0.2–0.6 ps considerably broader than the range observed for  $\tau_1$  which is about 0.65–0.8 ps (see figures 6.2 and 6.3). Secondly, and maybe more generally, the demagnetization can be described by a simple exponential time-dependence similar to the transient energy density. In contrast, the transient electron and lattice temperatures follow a more complicated evolution.

By studying the laser fluence dependence of demagnetization, it is concluded that only electron-phonon equilibration time does not explain the experimental demagnetization behavior. It is expected that the consideration of the spin-dependent phenomena will yield the appropriate description, this however requires insight into these elementary processes. Therefore, temperature-dependent studies were performed to understand these dynamics which are presented in the next section.

## 6. Non-equilibrium magnetization dynamics investigated by TRMOKE

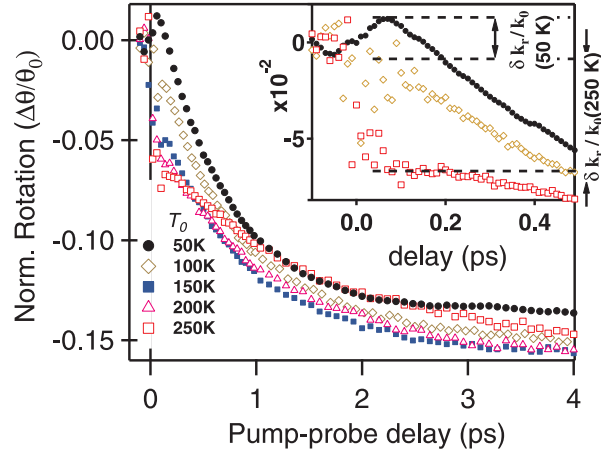


**Figure 6.4:** Time-dependent changes of the MOKE rotation signals after fs laser excitation normalized to the respective equilibrium values for 20 nm Gd(0001)/W(110) measured at different equilibrium temperatures  $T_0$ . As emphasized by the inset, within few hundred femtoseconds rotation shows a change in signal from positive to negative as  $T_0$  increases. From Ref. [136].

### 6.2 Effect of temperature on non-equilibrium magnetization dynamics

The temperature-dependent studies were performed on epitaxial Gd(0001)/W(110) film in a nominally constant absorbed pump fluence of  $\sim 1 \text{ mJ/cm}^2$ , as described in section 5.1.

Figure 6.4 shows the time-dependence of the transient MOKE rotation signal  $\Delta\theta$  normalized to the MOKE rotation signal without optical excitation  $\theta_0$  for different  $T_0$  for the initial few picoseconds following laser excitation. Similar to the discussion in the earlier section, the data features two contributions; some effects within few hundred femtoseconds, followed by a negative drop in the signal up to several picoseconds. A pronounced variation in  $\Delta\theta/\theta_0$  of 12–15 % is observed at a delay of 4 ps. At a closer look, an initial step-like contribution, which we term  $\delta k_r$  is also observed. This effect occurs essentially within 300 fs and is characterized by a change in the sign from positive to negative with increasing  $T_0$ , as highlighted in the inset of figure 6.4. Subsequent to these initial effects a continuous reduction in  $\Delta\theta/\theta_0$  is observed, which tends to saturate at 3 ps. At later time delays the signal is reduced further up to few hundred picoseconds, as discussed in chapters 4 and 5. Results for the MOKE ellipticity  $\Delta\varepsilon(t)/\varepsilon_0$  are shown in figure 6.5.  $\Delta\varepsilon$  show a similar behavior as in  $\Delta\theta$  at  $T_0 < 100$  K including the 15 % change

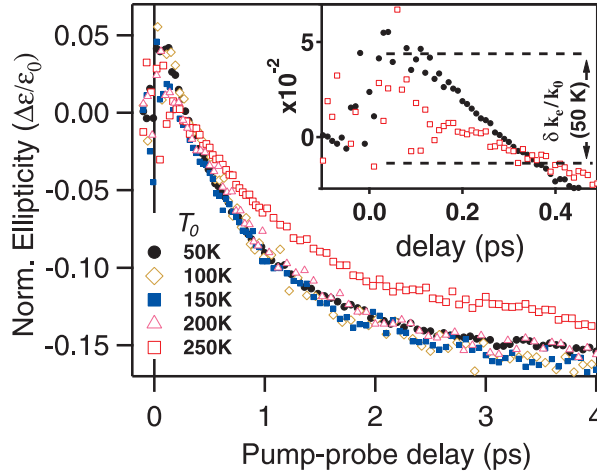


**Figure 6.5:** Time-dependent changes of the MOKE ellipticity signals after fs laser excitation normalized to the respective equilibrium values measured at different equilibrium temperatures  $T_0$ . As emphasized by the inset, positive change in ellipticity signal approaches to zero as temperature increases. From Ref. [136].

at 4 ps and a change  $\delta k_e$  at  $t < 300$  fs. However, with increasing  $T_0$  the sign of  $\delta k_e$  does not change, contrary to  $\delta k_r$ . From the temperature-dependent behavior depicted in figures 6.4 and 6.5 it is concluded that the dynamics can be divided into two regimes. The first one at delays close to 100 fs, shows a different temperature dependence for rotation and ellipticity. The second regime is characterized by an exponential decay in both MOKE signals with a characteristic time scale of about 1 ps. In the following a criterion is discussed to separate these two temporal regimes.

### 6.2.1 Extraction of concomitant $4f$ and $5d6s$ magnetization dynamics

Due to the optical wavelength employed in the experiment, MOKE is primarily sensitive to the conduction electrons and could contain non-magnetic contributions [17, 18, 19]. Although the total magnetization of Gd in equilibrium, i.e. on infinitely long time scales, is the sum of these  $5d$  and  $4f$  contributions, a dynamic picture might require a separate treatment of the localized and the conduction electrons. The time scale where both spin sub-systems behave concomitantly depends on the strength of the intra-atomic exchange interaction. To describe the laser-induced magnetization dynamics, the dynamic magnetization  $M(t)$  represents the concomitant demagnetization of the  $4f$  and  $5d6s$  moments. Here a procedure is introduced to separate the concomitant demagnetization from the rest of dynamics observed in the transient MOKE signal.

## 6. Non-equilibrium magnetization dynamics investigated by TRMOKE

---

In order to determine  $M(t)$ , which was established by fs-XMCD to follow a single exponential evolution as shown in figure 4.3, from the MOKE data we assume a time-dependent factor  $k_{r,e}(t)$  that accounts for the deviation from a well-defined 4f magnetization dynamics in the MOKE rotation and ellipticity.

$$\begin{aligned}\Delta\theta(t)/\theta_0 &= (\Delta M/M_0 + 1) \cdot k_r(t)/k_{0r} - 1 \\ \Delta\varepsilon(t)/\varepsilon_0 &= (\Delta M/M_0 + 1) \cdot k_e(t)/k_{0e} - 1.\end{aligned}\tag{6.1}$$

The determination of  $\Delta M$  requires assumptions on  $k_{r,e}(t)$ . A linear expansion of this quantity with the transient electronic energy density  $E_e(t)$  is used to separate  $\Delta M$  and  $k_{r,e}$ . This is reasonable because we observe a pronounced difference in  $\Delta\theta/\theta_0$  and  $\Delta\varepsilon/\varepsilon_0$  for  $t < 300$  fs, where the conduction electrons carry the dominant part of the excess energy as shown in figure 6.3 [27, 41]. The  $k_{r,e}$  are expanded with respect to  $E_e(t)$  as

$$k_{r,e}(T_0, t) = k_{0r,e}(T_0, t_0) + \frac{\delta k_{r,e}}{\delta E_e} \Delta E_e(T_0, t) + \dots \tag{6.2}$$

The first term  $k_0$  represents the value without laser excitation, obtained from static MOKE measurements;  $\delta k_{r,e}$  is the extremum value found near 80 fs, indicated in the insets of figures 6.4 and 6.5, and  $\delta E_e$  is the corresponding maximum in the electronic excess energy density  $E_e(t)$ , as shown in figure 6.3. Here we use the calculated values of  $E_e(t)$ , employing the two-temperature model (2TM) as discussed in section 6.1. Note that the 2TM is certainly a simplification of the electronic and lattice dynamics excited by the laser pulse. This model is used here because (a) it was demonstrated to hold after  $\sim 150$  fs [27, 41] and (b) it works well for the purpose of separation of  $M$  and  $k_{r,e}(T_0, t)$  here. After the separation of  $M$  and  $k_{r,e}(T_0, t)$ , it is possible to discuss each of these quantities independently. However, here only the concomitant demagnetization is discussed in detail.

In Eq. 6.1,  $k_{r,e}/k_{0r}$  are included as spectroscopic factors which describe the efficiency of the magneto-optical detection which can be modified by the pump laser excitation. However, pump-induced variations of the magnetic moment of the 5d electrons could also result in magnetic contributions in  $k_{r,e}/k_{0r,e}$ . However, here we briefly report on first observations, which we find worth to note. The temporal evolution of  $k_{r,e}(T_0, t)$  is calculated from the time-dependent  $\Delta E_e(t) = E_e(t) - E_0$ ;  $E_0$  being the energy density at  $T_0$  before optical excitation, from the 2TM. The results were scaled by  $\delta k_{r,e}(T_0)$  which were determined from the experimental results as shown in the insets of figures

## 6.2 Effect of temperature on non-equilibrium magnetization dynamics

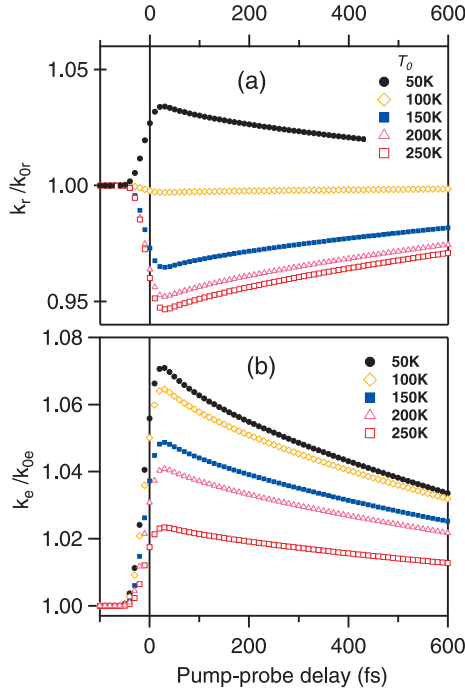


**Figure 6.6:** The variation of  $k_r/k_{0r}$  and  $k_e/k_{0e}$  for different temperatures  $T_0$  as a function of time. The amplitude is extracted from experimental data and the transient evolution is calculated by the electron energy density (see text). Both  $k_r/k_{0r}$  and  $k_e/k_{0e}$  increase for  $t < 300$  fs at 50 K while at higher temperatures their respective changes are of opposite sign. From Ref. [136].

6.4 and 6.5. The resulting time evolution of the  $k_r/k_{0r}$  and  $k_e/k_{0e}$  are shown in figure 6.6 a and b, respectively. These figures emphasize the changes within few hundred femtoseconds after optical excitation and their different temperature dependence. At  $T_0=50$  K, both  $k_r/k_{0r}$  and  $k_e/k_{0e}$  increase within 100 fs and decrease at later delays. At higher  $T_0$ ,  $k_r/k_{0r}$  and  $k_e/k_{0e}$  present a different behavior. While  $k_r/k_{0r}$  decreases to -6%,  $k_e/k_{0e}$  remains positive before both signals approach unity at later delays. The potential non-magnetic origin of the found temperature-dependent contributions could be the temperature-dependent changes in the electronic band structure [137, 138] which affect the magneto-optical response. The potential magnetic origin of this effect is discussed further in section 6.3. It should be noted that the above discussed procedure is reasonable to extract the concomitant 4f and 5d6s demagnetization, however, it may not be sufficient to describe the dynamics within initial few hundred femtoseconds unless all contributions are considered in equation 6.2. Figure 6.6 is presented to highlight the magnitude of the difference in the MOKE rotation and ellipticity transients observed within few hundred femtoseconds. In a femtosecond MOKE experiment these contributions are difficult to disentangle and a full treatment might require future, especially theoretical, work similar to [19].

## 6. Non-equilibrium magnetization dynamics investigated by TRMOKE

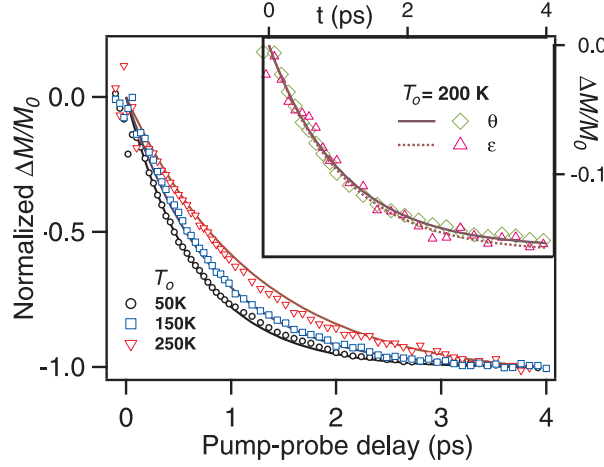


**Figure 6.7:** The main panel depicts  $\Delta M/M_0$  extracted from  $\Delta\theta/\theta_0$  for selected equilibrium temperatures. The curves have been normalized to -1 at  $t = 4$  ps. The inset compares the transient changes in the magnetization  $\Delta M/M_0$  at  $T_0 = 200$  K which were determined from the MOKE rotation and the ellipticity measurements. Lines represent single exponential fits. From Ref. [136].

As discussed above, it is possible to separate the concomitant demagnetization of  $4f$  and  $5d6s$  sub-systems. Now let us discuss the  $M(t)$  within few picoseconds for different temperature but excluding the initial few hundred femtosecond dynamics following laser excitation (the latter aspect is discussed in section 6.3).

### 6.2.2 Temperature dependence of non-equilibrium demagnetization time

In time-resolved XMCD work it was shown that the  $4f$  magnetic moment changes with a time constant of 0.76 ps after laser excitation. As discussed below, and shown in section 4.2, this time constant is also observed in time-dependent MOKE. In addition to this, a systematic temperature dependence of the demagnetization time is discussed.

After several 100 fs we find a continuous decrease of the MOKE ellipticity and the rotation, which agrees reasonably well with the dynamics of the  $4f$  magnetization as discussed in section 4.1.2. At this timescale the  $5d$  and  $4f$  spin systems are in equilibrium with each other and present identical dynamics.

The transient  $\Delta M/M_0$  is determined from  $\Delta\theta$  and  $\Delta\epsilon$  using Eqs. 6.1, 6.2 as discussed in the previous section. The resulting two data sets for  $\Delta M/M_0$ , which were determined from the MOKE rotation and ellipticity, agree with each other as exem-



## 6.2 Effect of temperature on non-equilibrium magnetization dynamics

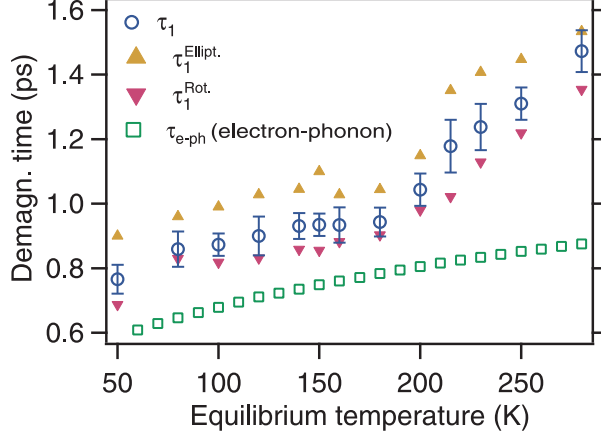


**Figure 6.8:** The variation of the demagnetization time ( $\tau_1$ ) (open circles) with equilibrium temperature  $T_0$ . The triangles show the demagnetization time ( $\tau_1^{\text{rot.}}$ ), ( $\tau_1^{\text{ell.}}$ ) when rotation (down triangles) and ellipticity (up triangles) were fitted separately. Demagnetization time increases linearly with  $T_0$  and changes slope around 170 K. For comparison temperature dependence of the electron-phonon equilibration time  $\tau_{e-ph}$  is shown by squares, see text.

plarily shown in the inset of figure 6.7 for  $T_0 = 200$  K. To illustrate the dependence on  $T_0$ , data for  $\Delta M(t)/M_0$  are shown in the main panel of figure 6.7 after their normalization to -1 at  $t = 4$  ps. It is evident from this comparison that the demagnetization develops more slowly for higher  $T_0$ . We determined the demagnetization time  $\tau_1$  by fitting  $\Delta M/M_0$  for different  $T_0$  by a single exponential dependence in the time interval from 0.2 to 4 ps and averaging over the values obtained from the MOKE rotation and ellipticity. The resulting fits are shown by solid lines in figure 6.7. These fits reasonably describe the experimental results. Figure 6.8 depicts the temperature dependence of the demagnetization time  $\tau_1$ , extracted from these fits. We observe a substantial increase in  $\tau_1$  with rising  $T_0$ . More precisely,  $\tau_1$  exhibits a five time increase in slope  $\partial\tau_1/\partial T_0$  at temperatures above 170 K compared to lower  $T_0$ . To test the robustness of this effect we also fit  $\Delta M/M_0$  originating from rotation and ellipticity separately ( $\tau_1^{\text{rot.}}$  -down triangles and  $\tau_1^{\text{ell.}}$  - up triangles, respectively). While the absolute value of the demagnetization time varies by about 10% depending on the considered data set, the kink in  $\partial\tau_1/\partial T_0$  prevails. Furthermore, the original experimental data of figures 6.4 and 6.5 was also fitted for comparison. This analysis yielded an offset in  $\tau_1$  of 150 fs. However, the overall temperature-dependent change in  $\tau_1$  was comparable to the results reported in figure 6.8 and we conclude that our analysis is robust regarding the temperature-dependent change in  $\tau_1$ .

## 6. Non-equilibrium magnetization dynamics investigated by TRMOKE

---

Similar to the comparison of the demagnetization time and the electron-phonon equilibration time as a function of fluence, I now consider the comparison of  $\tau_1$  with the electron-phonon equilibration time for different temperatures.

The electron-phonon energy equilibration time  $\tau_{e-ph}$  is determined from the transient electronic energy density as discussed in section 6.1 (and also shown in figure 6.3). The calculated  $\tau_{e-ph}$  as a function of  $T_0$  is shown by squares in figure 6.8. Similar to our observation in  $\tau_1(T_0)$ , the electron-phonon equilibration requires longer time for higher  $T_0$ . The electron-phonon thermalization and the demagnetization follow the comparable slope  $\partial\tau_1/\partial T_0$  at low temperatures. However, for  $T_0 > 170$  K,  $\tau_1$  deviates from the  $\tau_{e-ph}(T_0)$  trend.

These findings indicate that although a qualitative agreement between the temperature dependence of the demagnetization time and the electron-phonon equilibration time exists for  $T_0 < 170$  K, the whole temperature dependence of demagnetization is not in agreement with that of the electron-phonon equilibration. Demagnetization clearly proceeds more slowly than electron-phonon equilibration. Moreover, the pronounced kink in  $\partial\tau_1/\partial T_0$  at 170 K suggests that different processes are determining  $\tau_1$  below and above 170 K.

To understand the underlying mechanism of the demagnetization, we employ a theoretical modeling of the demagnetization using the Landau-Lifshitz-Bloch (LLB) equation, which is discussed in the following section.

### 6.2.3 Theoretical modeling based on the Landau-Lifshitz-Bloch (LLB) equation

The theoretical modeling of our temperature-dependent experimental results, presented in the earlier section, is done by means of the Landau-Lifshitz-Bloch (LLB) equation<sup>1</sup>. The theoretical model presented here is a step forward compared to the previous versions [35, 132, 134, 140] of LLB models. In these models the spin-flip rate had been included as a coupling-to-the bath parameter which up to now has been considered to be temperature-independent. Here we use a multi-spin quantum LLB model with interlayer heat diffusion and a temperature-dependent coupling-to-the bath parameter. In addition, the coupling is included considering both electrons and phonons as bath

---

<sup>1</sup>The LLB modeling is developed in a collaboration by Unai Atxitia and Oksana Chubykalo-Fesenko, CSIC, Madrid, Spain.

## 6.2 Effect of temperature on non-equilibrium magnetization dynamics

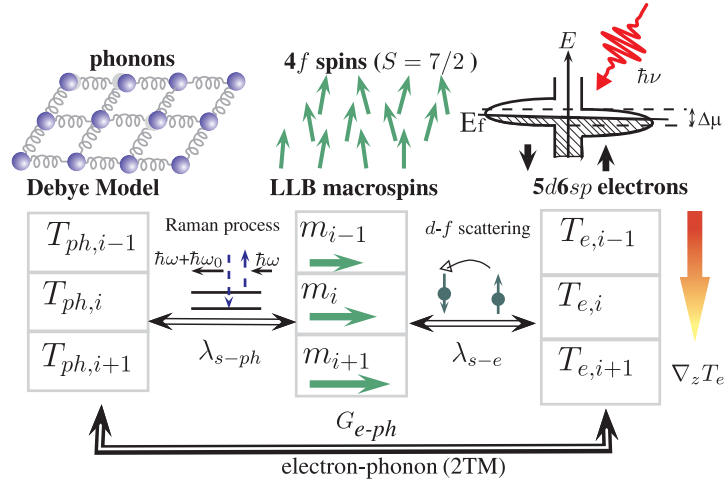


**Figure 6.9:** Schematic diagram of the model [139]. The multispin LLB model (center) is coupled to the 2T model via two coupling mechanisms: phonon contribution via Raman processes (left) and electron contribution via dynamical spin polarization of carriers which produces a change of chemical potential  $\Delta\mu$  [81] (right). The 2T model and the LLB model are time and layer resolved and the electron temperature diffusion is considered. The change in the phonon population with temperature is taken into account within the Debye model. From Ref. [136]

for the spins. Our model is related to the situation when the  $5d$  and  $4f$  spin systems are in equilibrium. The  $5d$  electrons provide a *thermal bath* for the joint magnetization dynamics. The magnetization of the  $5d$  system is neglected and the  $4f$  spin system interacts with external systems (laser and phonons) via  $5d$  electrons only.

Most of the previous works using the LLB model for ultrafast demagnetization [26, 37, 132, 141] consider the effect of the electron mechanism only, disregarding the phonon mechanism due to its potentially smaller and slower contribution. However, since in Gd the observed demagnetization is slower than in other materials like Ni, the spin-phonon coupling (via the spin-orbit coupling of  $5d$  electrons) can also play an important role [33]. In the following we describe the laser-induced dynamics in Gd considering that the localized  $4f$  part of its magnetic moment is affected by two contributions: coupling to the  $5d$  fraction through (a) electronic scattering processes and (b) scattering with phonons. We make use of the fact that the phonon population is well characterized as a function of  $T_0$ . The pronounced change in  $\tau_1(T_0)$  in the vicinity of the Debye temperature  $\Theta_D = 163$  K as depicted in figure 6.8 should provide a key to separate electron- and phonon-mediated spin-flip processes. Consequently, in our

## 6. Non-equilibrium magnetization dynamics investigated by TRMOKE

model both mechanisms are included. The obtained results will be compared to the experimental results in figure 6.10.

The schematic representation of our model for laser-induced demagnetization is shown in figure 6.9. The ultrafast demagnetization dynamics is modeled by a micromagnetic approach based on the (quantum) LLB equation [36, 88]. This equation (without the precessional term) for a system of ferromagnetic quantum spins interacting with a heat bath, describes the dynamics of the thermally averaged spin polarization  $m_i = M_i v_0 / \mu_0$  in the atomic layer  $i$ :

$$\frac{\dot{m}_i}{\gamma} = \sum_b \Lambda_b^i(T_b^i) \begin{cases} \frac{1}{2\tilde{\chi}_{||,b}^i} \left(1 - \frac{m_i^2}{m_{e,b,i}^2}\right) m_i & T_b^i \leq T_C \\ -\frac{1}{\tilde{\chi}_{||,b}^i} \left(1 + \frac{3m_i^2 T_C}{5(T_b^i - T_C)}\right) m_i & T_b^i \geq T_C \end{cases} \quad (6.3)$$

where the sum is over baths  $b$  (electron or phonon sub-systems). The longitudinal damping parameter  $\Lambda_b^i(T_b^i) = \lambda_b^i \frac{2T_b^i}{3T_C} \left[ \frac{2q_b^i}{\sinh 2q_b^i} \right]$  includes an intrinsic coupling-to-the-bath parameter  $\lambda_b^i$  (defined by the square of the scattering matrix elements [88]) as well as the spin part coming from the disordering at the quasi-equilibrium bath temperature  $T_b^i$ . Here  $\gamma = 1.76 \times 10^{11} (\text{Ts})^{-1}$  is the absolute value of the gyromagnetic ratio;  $m_{e,b,i}(T_b^i)$  is the quasi-equilibrium magnetization,  $q_b^i = 3T_C m_{e,b,i} / [2(S+1)T_b^i]$ ;  $v_0 = (5 \text{ \AA})^3$  is the unit-cell volume;  $\mu_0 = 7.55 \mu_B$  is the atomic magnetic moment for Gd;  $S = 7/2$  is the quantum spin number and  $T_C = 293 \text{ K}$  the Curie temperature. The longitudinal effective field (r.h.s in Eq.(6.3)) also accounts for magnetic fluctuations through the longitudinal susceptibility  $\tilde{\chi}_{||,b}^i$  within a dynamical mean-field approach for spin-spin interactions [88].

In this model, for laser-induced demagnetization the laser excites the  $5d$  electrons system which are coupled to the localized  $4f$ -electron spin system. After the pump pulse excitation a temperature gradient  $\nabla_z T_e$  is created due to an optical penetration depth  $\lambda_{op} = 20 \text{ nm}$  and the electron thermal conductivity. This leads to different quasi-equilibrium temperatures  $T_e^i(t)$  and  $T_{ph}^i(t)$  for each layer, obtained from the integration of the 2TM model [27, 41] as discussed in section 2.2.2. We consider the Gd thin film as 40 coupled macrospins [35, 142], each one representing a  $5 \text{ \AA}$ -thick layer, described by the set of LLB equations (6.3), coupled to electron and phonon systems. The exchange coupling between layers is considered to be temperature-dependent and scaled with the average magnetization [35, 132].

## 6.2 Effect of temperature on non-equilibrium magnetization dynamics

The modeling is performed by considering the possible dissipation mechanisms leading to a reduction of  $M$ . For the electronic mechanism, we use the  $d$ - $f$  indirect exchange interaction as responsible channel for the exchange of angular momentum between excited  $5d$  carriers and the localized  $4f$  spin system, similar to the  $sp$ - $d$  exchange model for magnetic semiconductors [81], as discussed in section 2.2.3. In this model, carriers act as a momentum sink and their finite relaxation time ( $\tau_{sr} \sim 100$  fs) reduces the available phase-space for spin-flip events leading to a dynamical spin polarization of the carriers. In the first approximation we model such a behavior as a time-dependent coupling parameter

$$\lambda_{s-e}(t) = \lambda_{s-e}^0 (1 - \sigma \Delta T_e(t)/T_e(t)). \quad (6.4)$$

The factor  $\lambda_{s-e}^0$  is adjusted to obtain an experimentally measured demagnetization of 15% within 4 ps at  $T_0 = 50$  K, leading to a reasonable small coupling parameter  $\lambda_{s-e}^0 = 0.00026$ . The value of  $\sigma$  is defined by the relaxation time of the carriers [81]. Therefore, the coupling parameter decreases with the increase of  $T_e$ . The total longitudinal relaxation parameter  $\Lambda_e(T_e)$ , which includes the spin part, increases with  $T_e$  but this increase is slowed down for high temperatures. The dotted line in figure 6.10 shows the demagnetization time obtained from the numerical integration of the system of Eqs.(6.3), considering only this scattering mechanism. The agreement between modeling (dashed line in figure 6.10) and experimental data holds until  $T_0 \approx 170$  K, a value close to  $\Theta_D = 163$  K.

Considering the pronounced change in  $\partial\tau_1/\partial T_0$  near  $\Theta_D$ , we add to the LLB equation the spin-phonon relaxation mechanism, coupling the magnetization dynamics also to  $T_l$ . Note that this coupling is also indirect and occurs through  $5d$  electrons. The Raman process, where a phonon  $\mathbf{k}$  is absorbed and a phonon  $\mathbf{q}$  is emitted in combination with a spin-flip, as described in section 2.2.3, is adequate to describe the spin-lattice relaxation  $\lambda_{s-ph} \sim D^2 \int d\omega_{\mathbf{k}} \omega_{\mathbf{k}}^6 n_{\mathbf{k}} (n_{\mathbf{k}} + 1)$ , where  $D$  is defined by the spin-orbit coupling [33]. We use the Debye model for the phonon frequency  $\omega_{\mathbf{k}}$  for the calculation of  $\lambda_{s-ph}$ . Its time-dependence is defined by  $T_l$  in each layer in the following way [33]:

$$\lambda_{s-ph}(t) = \lambda_{s-ph}^0 (T_l/\Theta_D)^7 G_6(\Theta_D/T_l), \quad (6.5)$$

where  $G_n(y) \equiv \int_0^y dx x^n e^x / (e^x - 1)^2$ . For  $T \ll \Theta_D$  the rate grows as  $T_l^7$ , whereas for  $T \gg \Theta_D$  it grows as  $T_l^2$  with a transition between the two regimes at  $T_l > 0.2\Theta_D$ .

## 6. Non-equilibrium magnetization dynamics investigated by TRMOKE

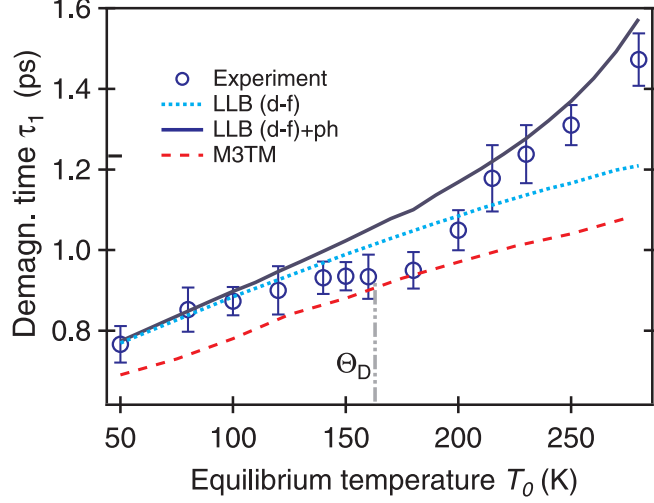


**Figure 6.10:** Comparison of experimentally determined demagnetization time  $\tau_1$  with theoretical results, as a function of  $T_0$ . Symbols represent the experimental data points while lines represent the modeling results considering only electron-spin flip coupling (dotted line) and combined electron-/phonon-mediated spin-flips (solid line) with  $\lambda_{s-ph}^0 = 0.0002$ . The dashed line represents the results obtained within the M3TM model assuming EY scattering mechanism. From Ref. [136]

Thus, the coupling to the phonon sub-system is negligible at  $T_l < \Theta_D$  but starts to increase with temperature in the vicinity of  $\Theta_D$ . The results of the integration of the LLB equations [136] with the two coupling mechanisms are in perfect agreement with experimental results presented in figure 6.7. The magnetization decay takes place in the time-scale up to 50 ps and is not single-exponential. Similar to the experiment, we focus our attention to the timescale of several ps and fit the modeling results to a single exponential function with characteristic demagnetization timescale  $\tau_1$ . The resulting values of  $\tau_1$  also show a good quantitative agreement with the experimental data, see figure 6.10 (black line). Please note that when only the phonon mechanism is considered, the demagnetization time is found in our model to be of the order  $\tau_2 \sim 50 - 100$  ps (the experimental results are discussed in section 5.1), in agreement with theoretical predictions [33], and is found to decrease with temperature. This process alone cannot account for the observed ultrafast demagnetization. It is shown that the experimentally determined temperature dependence of demagnetization time is successfully reproduced by LLB modeling with two coupling mechanisms.

Before finalizing the discussion it is also important to talk about the amplitude of

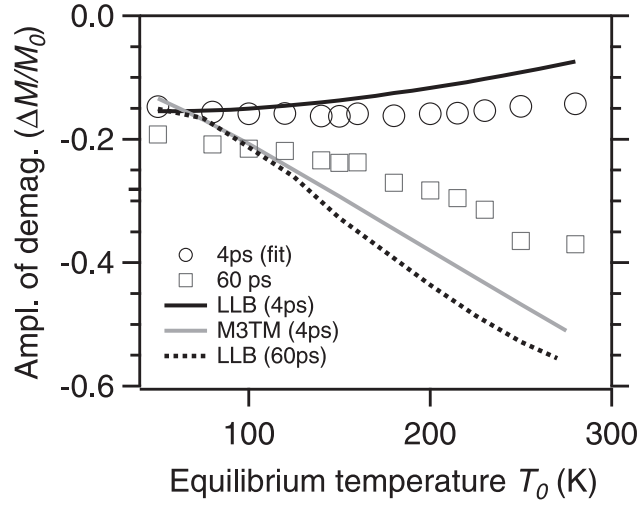


**Figure 6.11:** Variation of demagnetization amplitude  $\Delta M/M_0$  with equilibrium temperature and comparison with theoretical results. Symbols represent the experimental data points, black and gray lines represent the amplitude of demagnetization at 4 ps calculated by LLB and M3TM modeling, respectively. The dotted line represents the amplitude at 60 ps by LLB model.

demagnetization of the non-equilibrium and quasi-equilibrium demagnetization<sup>1</sup>. The amplitude of non-equilibrium demagnetization  $\Delta M/M_0(4ps)$  determined from fitting of experimental results is shown by the open circles in figure 6.11. In order to analyze the influence of  $T_0$  on the photo-induced change of the quasi-equilibrium demagnetization,  $\Delta M/M_0(60ps)$  is determined from the experimental measurements at fixed delays ( $t_0$ ) of 0.1, 4, and 60 ps as a function  $T_0$ . The open squares in figure 6.11 represent  $\Delta M/M_0$  at a delay of 60 ps. We note that the phonon-mediated demagnetization is intrinsically slower than the electronic one. Thus the observed behavior is different at different timescales. At  $t < 4$  ps (neglecting the first 0.1ps interval) the dynamics is dominated by  $T_e$ . In agreement with the slowing down of  $\Lambda_e(T_e)$ , the value  $\tau_1$  increases and the demagnetization value  $|\Delta M/M_0|(4ps)$  changes weakly as a function of  $T_0$  (see figure 6.11).

At longer timescales  $> 10$  ps, the electron and phonon temperatures have equilibrated and the coupling to the phonon system starts to dominate, with increasing temperature. As a result  $\Delta M/M_0$ , at 60 ps, increases with  $T_0$  (shown by open squares

<sup>1</sup>Since in this LLB modeling the phonon-mediated process is one which drives the quasi-equilibrium demagnetization, which is already discussed in chapter 5. The discussion of slower (quasi-equilibrium) demagnetization is included again for comparison of amplitude of the fast and slow processes.

## 6. Non-equilibrium magnetization dynamics investigated by TRMOKE

---

in figure 6.11), contrarily to the behavior at 4 ps. The analysis of experimental and theoretical data also shows that there is a contribution of phonons to  $\tau_1$  at  $T_0 > \Theta_D$  when the coupling to the phonon system increases considerably. The contribution of both relaxation mechanisms slows down the demagnetization via the nonlinearity of the response in Eq. (6.3).

As the LLB equations correctly take magnetic fluctuations at temperatures close to  $T_C$  into account [133] and explicitly include the critical slowing down effect, which was discussed in section 5.1.1, we also discard mechanisms based on such fluctuations [141] as responsible for the observed increase in  $\partial\tau_1/\partial T_0$  for  $T_0 \gtrsim 170$  K. Finally, in contrast to the widely used Matthiessen's rule, the scattering rates  $\Gamma = 1/\tau_M$  of different processes do not add up  $\Gamma \neq \Gamma_{s-ph} + \Gamma_{s-e}$  due to the nonlinear dependence on magnetization, of the relaxation rates in Eq.(6.3).

For comparison, we present in figure 6.10 (grey line) the results of the integration of the M3TM model, recently proposed in Ref. [37], which is based on phonon-mediated Elliott-Yafet scattering. The M3TM model has been implemented using the same 2T model as the LLB model. It is equivalent to the LLB model with  $S = 1/2$  and  $\lambda_{EY} \sim (T_l/T_e)$ , see Ref. [36]. The parameter  $\lambda_{EY}$  was taken from Ref. [37] which gave a correct demagnetization at 4 ps and  $T_0 = 50$  K. Although demagnetization time calculated by M3TM shows a similar behavior as our LLB results for  $T_0 < 170$  K (see figure 6.10), it does not account for the slower demagnetization at  $T_0 > 170$  K. Furthermore,  $|\Delta M/M_0|$  at 4 ps increases with temperature, contrary to the experimental observations as shown in figure 6.11.

Finally, laser fluence dependence of demagnetization time is also calculated by M3TM and results were compared with our experimentally determined demagnetization time (section 6.1). Our experimental results of figure 6.2 show weak dependence on laser fluence, whereas the M3TM [37] predicts a linear increase in the demagnetization time from 0.2 to 0.8 ps corresponding to fluence variation of  $1 \text{ mJ/cm}^2$  which is again stronger than the experimental values.



### 6.3 Dynamics within the initial few hundred femtoseconds

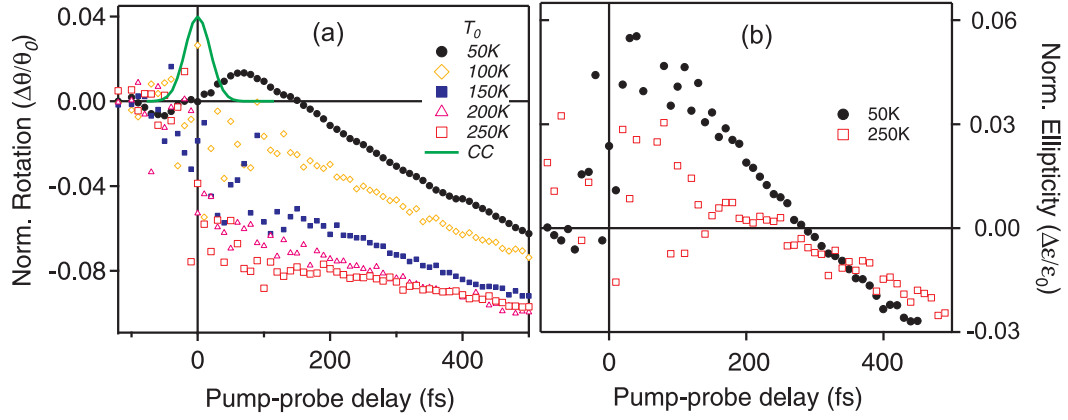


**Figure 6.12:** Time-dependent changes of the MOKE signals after fs laser excitation measured at different equilibrium temperatures  $T_0$ , emphasizing the dynamics of initial few hundred fs. Panel (a) depicts the transient MOKE rotation and (b) the MOKE ellipticity. The rotation and ellipticity results show a different  $T_0$  dependence behavior within the initial few hundred fs. The green solid line is a Gaussian function representing a cross-correlation signal corresponding to the 40 fs laser pulse.

### 6.3 Dynamics within the initial few hundred femtoseconds

As discussed in chapter 4, the  $4f$ - $5d$  exchange interaction is so strong that  $4f$  and  $5d$  magnetization measured by the MOKE and XMCD, respectively, show similar dynamics down to few hundred fs. So far, I have discussed the concomitant demagnetization of  $4f$  and  $5d$ . Now let us look at the dynamics for  $t < 300$  fs where the transient change is different in MOKE rotation and ellipticity and also different from the XMCD results.

Figure 6.12(a) shows the time-dependence of the normalized MOKE rotation  $\Delta\theta/\theta_0$  signal for different  $T_0$ . These are the same results as in the inset in figures 6.4 and 6.5, with special emphasis on the dynamics of few hundred fs following laser excitation. At equilibrium temperature  $T_0 = 50K$  the  $\Delta\theta/\theta_0(t)$  initially increases to 2 % with a peak at about 100 fs and then decreases showing the exponential decay. The latter can be observed similarly in the XMCD results (see figure 4.4). At higher temperatures the MOKE signal  $\Delta\theta/\theta_0(100 \text{ fs})$  changes the sign and decreases linearly with increasing  $T_0$ . The green solid line is a Gaussian function to represent the temporal width of the cross-correlation signal and it is clear that the observed initial maximum in the signal at  $T_0 = 50K$  is beyond this cross-correlation signal. Therefore, optical contributions originating directly from the pump laser pulses can be ruled out. Complementary to

## 6. Non-equilibrium magnetization dynamics investigated by TRMOKE

---

the MOKE rotation, ellipticity  $\Delta\varepsilon/\varepsilon_0$  measurements were also recorded to compare the ultrafast dynamics which is shown in figure 6.12 (b).  $\Delta\varepsilon/\varepsilon_0(t)$  increases to 7% within the initial 100 fs and then decreases similar to the MOKE rotation at low temperatures. At higher  $T_0$ ,  $\Delta\varepsilon(100 \text{ fs})/\varepsilon_0$  decreases with temperature but does not change the sign, contrary to the MOKE rotation. Two contributions to this can be separated from the experimental results with increasing  $T_0$ . Firstly, we note that the positive change in both rotation and ellipticity signals starts to increase continuously after laser excitation and peaks at about 100 fs. Secondly, in MOKE rotation (at higher temperatures) the negative drop in the signal appears within the laser pulse duration.

As discussed in chapter 4, measured by the time-resolved XMCD, the  $4f$  magnetization changes with a time constant of 0.8 ps after laser excitation [58] and the transient change in the signal can be described by an exponential function without an increase in the signal within 100 fs. It had already been shown in section 4.2 that this time constant is also observed in time-dependent MOKE. However, in addition to the behavior found in XMCD, a partial increase in the MOKE signal is also observed.

Due to the positive change in both rotation and ellipticity signals for  $t < 300$  fs observed at 50 K, the increase in the signal is attributed to an increase in the transient spin polarization of the conduction electrons. Since at higher temperatures  $T_0 > 50\text{K}$ ,  $\Delta\theta/\theta_0$  and  $\Delta\varepsilon(t)/\varepsilon_0$  differ in the sign of the pump-induced change, one can consider the non-magnetic effects here [17, 18, 19].

A scenario is suggested here for a consistent explanation of this earlier dynamics following optical excitation. Owing to the similarity of the MOKE rotation and ellipticity, we attribute the observed increase in the signal within few hundred femtoseconds to the magnetic  $5d$  contributions. A change of magnetization requires angular momentum transfer from the magnetic moment of interest to (a) the lattice or (b) another magnetic moment. In Gd, the direct coupling of  $4f$  spins to the lattice is inhibited by the zero orbital momentum of the  $4f$  shell and only the  $5d$  electrons present the spin-orbit interaction required for an angular momentum transfer to the lattice. Owing to that, the angular momentum is transferred (i) from  $4f$  magnetic moments to  $5d$  spins and then (ii) from  $5d$  spins to the lattice. The efficiency of the last step could be limited by the available phonons forming a phonon bottleneck for demagnetization. This effect would be even larger at early delays when only few phonons are excited. Finally, one

### 6.3 Dynamics within few hundred femtoseconds

---

can suppose that process (ii) is faster for higher equilibrium temperatures  $T_0$  and accelerates with the increasing pump-probe delay time. On the contrary, process (i) may be accelerated by the elevated electron temperature, i.e. it may slow down with the increasing pump-probe time delay. Such variations of the relative spin transfer rates of these two processes could lead to the angular momentum accumulation in the spin sub-system of  $5d$  electrons at low  $T_0$  and small delays if the channel (i) is fast enough. Such is the case for Gd where the energy of the intra-atomic-like exchange interaction between  $4f$  magnetic moments and spins of  $5d$  electrons is about 700 meV [52]. This transient increase of the conduction band spin polarization which primarily influences the MOKE signal, is in agreement with our observation in figure 6.12 at 50 K within  $t < 300$  fs. Since the  $4f$  magnetic moment is larger than the  $5d$  one, the latter will follow the  $4f$  dynamics at longer delays which is also mediated by  $5d6s$  spins. Therefore, the interplay between these two spin systems can result in the transient spin polarization. Note that a similar mechanism was suggested employing the  $sp-d$  model where localized magnetization can change at the cost of conduction electron spin polarization and vice versa. This effect is called the (inverse) Overhauser effect [79, 80, 81], as discussed in section 2.2.3. The mechanism based on the  $sp-d$  model is depicted in figure 6.13 where laser excites the conduction electrons and the energy and angular momentum are shared between different sub-systems. Our experimental results show the accumulation of the angular momentum in the conduction electrons at low temperatures when phonons are not excited which is in principle some indication of agreement with the  $sp-d$  model prediction [79, 80, 81]. However, this is only a comparison on a quantitative basis because the original model was employed on magnetic semi-conductors which have completely different electronic band structure than lanthanides.

Very recently Mentink et al. [143] suggested that the dynamics of a two sublattice magnetic system can be divided into two regimes depending on the temperature at which ferro-/ ferri-magnet is excited. To explain the angular momentum conservation, the authors suggest that at high temperatures (above the Curie temperature) while the thermal energy is higher than the exchange interaction the angular momentum is transferred to the environment (electrons/lattice). On the other hand at low temperatures, the dynamics is dominated by exchange interaction and the angular momentum is shared between two spin sub-lattices. In our experimental results we observed a similar behavior where the increase in the MOKE signal depends on the temperature.

## 6. Non-equilibrium magnetization dynamics investigated by TRMOKE

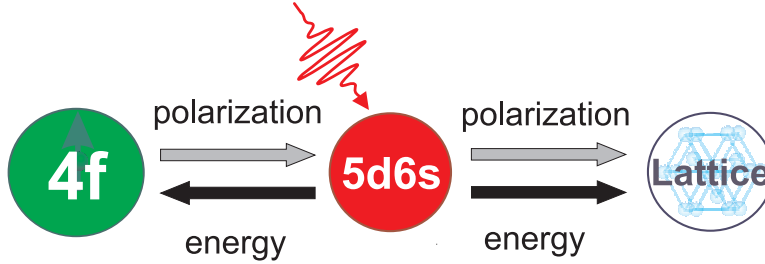


**Figure 6.13:** Schematic showing the excitation of the conduction electron and distribution of energy and angular momentum among the three sub-systems in Gd. Experimentally an increase in the magneto-optical signal is observed for  $t < 300\text{fs}$ , which is explained as a competition of the angular momentum transfer between different sub-systems (see text). The schematic is similar to one presented to explain the ultrafast demagnetization of the magnetic semiconductors [79, 80, 81] on the basis of the Overhauser effect.

At low temperatures the angular momentum is shared between the spins of the two ( $4f$  and  $5d6s$ ) spin sub-systems. At higher temperatures when phonons are available for sharing the angular momentum, the MOKE signal at 100 fs decreases. However, theoretical calculations similar to [143] could give more insights into the microscopic process for Gd as well.

In addition to consequences of angular momentum conservation and hence  $5d$  spin polarization (which is discussed above), one could also expect further magnetic as well as nonmagnetic contributions after fs laser excitation. Magnetic contributions which were discussed in the literature include the coherent [24] and transport [26] effects. A quantitative assignment of the observed transient MOKE signals to either of these contributions is clearly beyond our experimental sensitivity. In particular since a difference between the transient MOKE rotation and ellipticity after an optical excitation is affected by dichroic bleaching or state blocking [17, 18, 19], which cannot be excluded at early delays following fs laser excitation. The verification of this scenario and more detailed analysis of the spin dynamics proceeding before the equilibration of  $5d$  spins and  $4f$  magnetic moments, would require further experimental and theoretical efforts.

### 6.4 Summary

Laser-induced magnetization dynamics is analyzed focusing on the non-equilibrium regime.

Time-resolved MOKE measurements are performed as a function of pump fluence on Gd(0001). Variations of the pump fluence of up to  $1 \text{ mJ/cm}^2$  show a weak increase in the bulk demagnetization time of about  $70 \text{ fs}/(\text{mJ/cm}^2)$ . A comparison of the fluence-dependent energy transfer among electrons and the lattice (electron-phonon equilibration) with the demagnetization revealed a qualitative agreement in the increase of the demagnetization time and the time scale of the energy transfer. On a quantitative level there are, however, deviations which are attributed to the fact that in the simplified description of energy transfer spin-dependent processes were not taken into account.

To disentangle different microscopic contributions, a temperature-dependent analysis of fs laser-induced demagnetization of Gd(0001) is performed by time-resolved MOKE and the Landau-Lifshitz-Bloch model. The obtained experimental data is separated into two regimes: several 100 fs after the optical excitation, when the  $5d6s$  conduction electrons carry the major part of the excess energy; and a subsequent regime until several picoseconds, i.e. the regime in which the conduction electrons equilibrate with the phonons.

In the picosecond regime transient variations of both the MOKE ellipticity and rotation is observed which agree well with each other and we assign them to the magnetization dynamics dominated by the  $4f$  magnetic moments. A two time increase in the characteristic demagnetization time from 0.8 ps at 50 K to 1.5 ps at 280 K is observed. A successful quantitative explanation of this behavior is presented on the basis of the results from the Landau-Lifshitz-Bloch model by microscopic electron- and phonon-mediated demagnetization processes. In general a temperature increase results in a slower demagnetization. At low temperatures the demagnetization times observed in experiment can be modeled by considering electronic processes only. At temperatures above the Debye temperature, however, phonon-mediated processes have to be taken into account as well.

For the explanation of the dynamics within the initial few hundred femtoseconds following laser excitation a scenario is suggested for magnetic contributions. In particular an increase in the ellipticity and rotation signals is recognized at 50 K that is attributed to the increase in the  $5d6s$  spin-polarization as compared to the decrease in the  $4f$  magnetization. These results are explained by considering the competition between the angular momentum transfer from localized  $4f$  to the  $5d6s$  moments and  $5d6s$  to the lattice. If the rate at which the momentum is injected to the  $5d6s$  electrons

## **6. Non-equilibrium magnetization dynamics investigated by TRMOKE**

---

is larger than the rate at which it is transferred to the lattice, accumulation of angular momentum and hence a transient spin polarization is expected in conduction electrons which is observed as an increase in the MOKE signal at 100 femtoseconds. However, further theoretical as well as experimental investigations are essential to understand this initial dynamics where non-magnetic contributions in the MOKE signal cannot be ruled out.

## 7

# Comparison of dynamics: bulk vs surface

In this chapter, I will present a study where bulk and surface contributions to magnetization are investigated. This is achieved by the comparison of surface and bulk sensitive detection of the transient magnetization in Gd(0001) measured by time-resolved magnetic second harmonic generation (MSHG) and magneto-optical Kerr effect (MOKE), respectively.

## 7.1 Comparison of surface and bulk magnetization dynamics

The discussion of the surface and bulk dynamics starts with the comparison of surface sensitive SHG and the bulk sensitive MOKE measurements from an epitaxial 20 nm thin Gd(0001) film grown on W(110) substrate. The experimental details has already been described in chapter 3.

Figure 7.1 shows the odd part  $\Delta_{\text{odd}}^{2\omega}$  (solid line, left axis) of second harmonic signal, which is sensitive to the surface magnetization, and MOKE signal  $\Delta\theta/\theta_0$  (dotted line, right axis), which is sensitive to the bulk magnetization, measured simultaneously at an equilibrium temperature of 50 K and absorbed pump fluence of  $1 \text{ mJ/cm}^2$ . Both signals indicate a pronounced laser-induced demagnetization, but their transient behavior is different. The magnetic SHG signal is reduced within the laser pulse duration of 35 fs by 0.5 and exhibits almost on that level oscillations that are damped out within 3 ps.

## 7. Comparison of dynamics: bulk vs surface

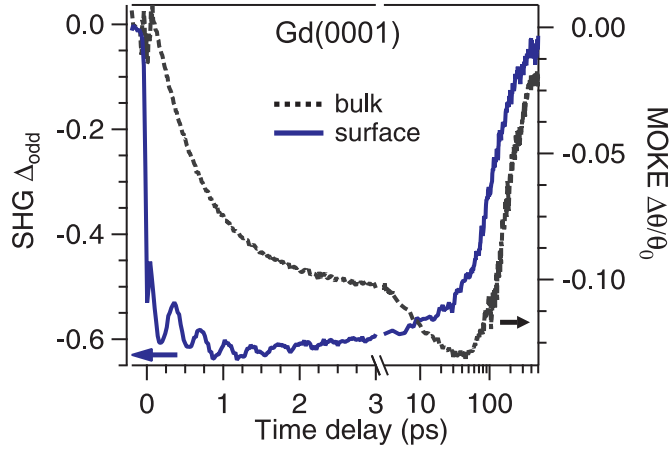


**Figure 7.1:** Time-dependent magneto-optical signals measured on 20 nm thick Gd(0001) films, which were grown epitaxially on W(110). The solid line indicates the pump-induced change of the magnetic SHG contribution  $\Delta_{\text{odd}}^{2\omega}$  sensitive to the surface. Similar results were published before [43, 144, 145]. The dotted line depicts the pump-induced MOKE polarization rotation  $\Delta\theta$  normalized to the static rotation  $\theta_0$ . From Ref. [117].

Averaging over the oscillations one finds that the  $\Delta_{\text{odd}}^{2\omega}$  signal is slightly reduced further until about 1 ps. The signal starts to recover subsequently and returns to its value before optical excitation after several 100 ps. The oscillatory part has been explained before as a coupled phonon-magnon mode localized to the surface [43, 146] and thus not expected in the bulk (MOKE) signal. The MOKE data can be described by a continuous reduction that will be fitted by a single exponential decay below and tends to saturate at a delay of 3 ps, before it demagnetizes further according to the weak spin-lattice coupling, as discussed in section 4.2 and in chapter 5. The bulk sensitive signal is reduced on a much slower time scale than the surface one and is in agreement with femtosecond x-ray magnetic dichroism studies, as discussed in section 4.1.

To explain the difference between the surface and bulk demagnetization it is informative to inspect the electronic structure at the surface and to take transfer processes into account. Figure 7.2, depicts several data sets which in their combination represent the electronic states near the Fermi energy  $E_F$ , of epitaxial Gd(0001) films. For a ferromagnetically ordered situation the states are exchange-split due to intra-atomic exchange interaction with the strong magnetic moment of the half filled  $4f$  shell. At the  $\bar{\Gamma}$ -point the bulk  $5d$ -states appear at 1.4 eV (minority) and 2.4 eV (majority) binding energy and disperse towards  $E_F$  with increasing  $k_{||}$  [149]. The majority component of the exchange-split  $5d_{z^2}$ -surface state is dominantly occupied and the minority one



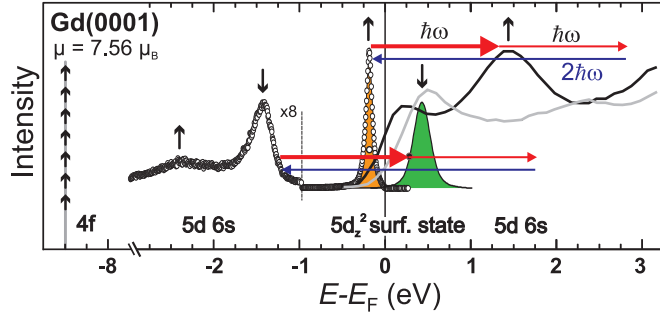


**Figure 7.2:** From Ref. [43], the valence electron states of Gd(0001) taken from normal direction photoemission (circles), inverse photo-emission (solid lines) [147], and scanning tunneling spectroscopy data above the Fermi level (solid line, filled) [148]. The exchange-split surface state (filled area) appears around the Fermi level. Vertical arrows represent the majority and minority character of the electronic states. Indicated are the two main absorption channels for 1.5 eV pump photons and the resonant second harmonic probing scheme.

unoccupied. The system also contains unoccupied exchange-split bulk states probed by inverse photoemission [147].

For linearly polarized light, within the dipole approximation, optical transitions proceed among occupied and unoccupied electronic states in (bulk) valence bands with the same spin character. In case of the excitation by the 800 nm (or 1.55 eV) pump laser pulses, an additional excitation channel becomes available at the surface because of resonant transitions coupling the bulk and the localized surface electronic states, see figure 7.2. Therefore a difference of the surface sensitive SHG response with respect to the bulk sensitive MOKE can be expected. Similar to a charge-transfer excitation across molecular interfaces [150], such surface-bulk resonances can lead to effective electron transfer between surface and bulk which modify the transient population of the minority and majority components of the surface state. The population of the initially occupied majority surface state component is reduced due to the surface-to-bulk spin-up electron transfer, see figure 7.2. At the same time, the population of the initially unoccupied minority surface state component increases due to the bulk-to-surface spin-down electron transfer, which can alternatively be viewed as a surface-to-bulk spin-down hole transfer. The carriers in the surface state which are transferred to bulk bands represent initially a wave packet at the surface which spreads and propagates into the bulk material with its Fermi velocity  $v_F$  [72] of about 1 nm/fs. A typical value for the Gd determined from the calculated electronic band structure [149] is about 0.3

## 7. Comparison of dynamics: bulk vs surface

---

nm/fs. Thus, a spin-polarized current which propagates from the surface to the bulk is optically excited. In the vicinity of the surface, hot carriers excited in the surface state propagate ballistically and the current consists of electron and hole contributions. In terms of a charge current, electron and hole propagation compete with each other. Assuming electron and hole excitation with the identical probability, no charge current would be excited. This is different for the spin current because spin-down holes have the same spin polarization as spin-up electrons. Therefore, the spin components of these two current contributions will add up. If the charge of electrons and holes is in sum zero, it is concluded that a net spin current between surface and bulk is excited. Note that this does not necessarily imply charging of the surface because a transient charge imbalance will be screened by electron rearrangement on the time scale of the inverse plasma frequency [63]. Furthermore, it is likely that the efficiency of electronic transitions in spin-up and spin-down channels are different (figure 7.2) which will lead to a prevalence of either the electron or hole component of the spin-polarized current. On the basis of these considerations an effect due to optically excited transfer of spin polarization between surface and bulk should proceed within few femtoseconds, i.e. well within the time resolution of the SHG experiment.

It is known that optically excited charge carrier distributions in ferromagnets can modify the linear magneto-optical response by dichroic bleaching or state blocking effects [19]. Therefore one could ask whether the non-linear data discussed here are affected by such effects. It is unlikely due to the following reasons. First, our analysis is based on an intensity measurement, rather than on an analysis of the complex Kerr angle in linear magneto-optics (latter discussed in section 6.2.1). Second, a change in  $\Delta_{\text{odd}}^{2\omega}$  appears within the laser pulse duration and remains until a time delay of 10 ps, i.e. during time scales where the hot charge carrier distribution, which is responsible for optical artefacts, have already decayed. Third, in  $E_{\text{even}}^{2\omega}$  (which is sensitive to non-magnetic contributions) we do not observe any significant features which may be attributed to optical artefacts. Therefore it can be safely concluded that the dominant part of  $\Delta_{\text{odd}}^{2\omega}$  is of genuine magnetic origin.

As seen in figure 7.1, the pronounced initial drop in the surface sensitive magneto-optical signal occurs within the experimental time resolution and clearly faster than the bulk demagnetization. Therefore, the pronounced difference in the bulk and surface demagnetization times is explain as spin transfer between surface and bulk of the film.

The time scale at which the magnetic SHG signal  $\Delta_{\text{odd}}^{2\omega}$  changes from 0 to -0.5 at time zero is in agreement with a ballistic or super-diffusive character of these transport effects [26]. The pump-induced reduction of the relative magneto-optical signals differ by a factor of six. A resonant surface excitation among bulk and the surface states near  $\bar{\Gamma}$ , see figure 7.2, is considered as essential for an explanation of the pronounced effects at the surface.

By combining ultrafast bulk and surface sensitive magneto-optical techniques, the femtosecond laser-induced demagnetization of epitaxial Gd(0001) films is analyzed. In the bulk, demagnetization occurs with a characteristic time of about 0.7 ps. Considering that the surface sensitive signal changes within the laser pulse duration of 35 fs and taking resonant optical transitions between valence electronic surface and bulk states into account, this ultrafast change is attributed to the transfer of spin-polarized charge carriers between surface and bulk states.

As a remark, from the comparison of the MSHG and MOKE results in figure 7.1 the initial increase in the MOKE signal (for  $t \leq 300$  fs which has been discussed in section 6.3) is on a similar time scale when the surface signal drops to 50 %. One could expect the spin polarized electrons, which transfer from the surface to the bulk, can contribute to the MOKE signal. Considering this we investigated the dynamics using MOKE after quenching the surface state of Gd(0001) by oxygen and yttrium evaporation (not shown here). The overall dynamics was largely unaffected. Therefore, we rule out the possibility of surface spin transport as dominant contribution in MOKE signal for  $t \leq 300$ .

## 7.2 Summary

By comparing the surface- and bulk-sensitive time-resolved MSHG and MOKE results, respectively, possible mechanisms of spin transport are discussed. The initial drop in the surface-sensitive magneto-optical signal is observed within the experimental time resolution and is clearly faster than the bulk demagnetization. The pronounced difference in the bulk and surface demagnetization times is explained as the resonant spin transfer between bulk and surface state of Gd.

## 7. Comparison of dynamics: bulk vs surface

---

# Magnetization dynamics of the GdTb alloys

Spin-lattice relaxation mediated via spin-orbit coupling is a key parameter in ultrafast magnetization dynamics. After investigating the role of spin-orbit coupling in demagnetization of Gd and Tb metals, in this chapter the static and dynamic magnetic properties of GdTb alloys are investigated.

As already described in chapter 2, due to the half-filled  $4f$  shell Gadolinium has an orbital angular momentum  $L=0$ , hence the direct  $4f$  spin-lattice coupling in Gd is rather weak. On the other hand Tb has  $L=3$  with a non-spherical orbital, therefore the spin-orbit coupling in Tb is very strong. It has already been established in chapter 4 that the spin-orbit coupling plays an important role in the quasi-equilibrium magnetization dynamics of Gd and Tb metals, however, demagnetization in the non-equilibrium state is not affected by the difference of the spin-orbit coupling of these metals. GdTb alloys can thus provide the opportunity to control the ultrafast magnetization dynamics through the tuneable spin-orbit coupling by controlling the composition.

The detailed concentration dependent magnetization dynamics is investigated in  $\text{Gd}_x\text{Tb}_{100-x}$  alloys for  $30 \leq x \leq 100$ , employing the static and time-resolved magneto-optical Kerr effect (MOKE). The static magnetic properties are discussed in section [8.1](#) while the study of the magnetization dynamics is discussed in section [8.2](#).

## 8. Magnetization dynamics of the GdTb alloys

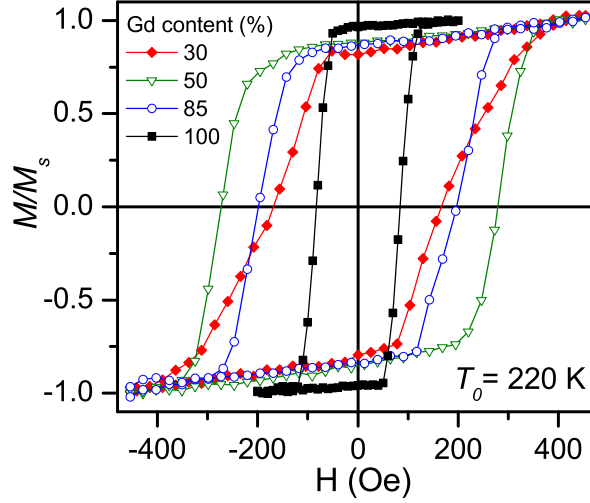


**Figure 8.1:** Hysteresis loops for different atomic % of Gd in GdTb alloys measured by MOKE rotation at  $T_0 = 220$  K. The magnetization is normalized to the saturation value  $M_s$ . With substitution of Tb, coercivity increases and shape of hysteresis also changes.

### 8.1 Static magnetic properties

Epitaxial films of 20 nm thickness with changing concentrations in  $\text{Gd}_x\text{Tb}_{100-x}$  were prepared on W(110) substrate in the ultrahigh vacuum conditions, as described in chapter 3. The experimental details for static magnetic properties and magnetization dynamics has already been described in chapter 3.

Before moving on to magnetization dynamics, static magnetic properties were investigated as a function of concentration. Magnetic hysteresis curves for different atomic % of Gd in GdTb alloy films are shown in figure 8.1, where magnetization is normalized to saturation value. The magnetic hysteresis curves were measured using MOKE rotation on equilibrium temperature of 220 K. The symbols are experimental results whereas lines are merely guides to the eye. The coercivity of the alloys increases from 85 Oe for pure Gd to about 280 Oe for  $\text{Gd}_{50}\text{Tb}_{50}$  alloy film. Moreover, the shape of the hysteresis changes from the rectangular to a more flat one for  $\text{Gd}_{30}\text{Tb}_{70}$  alloy film and higher Tb concentrations. The increase in the coercivity is consistent with the strong spin-orbit coupling of the Tb which increases the magneto-crystalline anisotropy of the system. However, the changing shape of the hysteresis for higher Tb concentrations might be due to change in easy axis of magnetization.

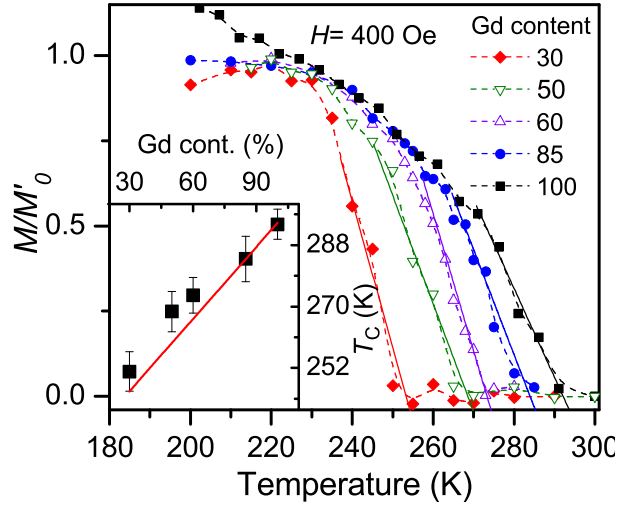


**Figure 8.2:** Temperature-dependent magnetization  $M/M'_0$  with  $M'_0$  is the magnetization at  $T_0=220\text{K}$  for different atomic % of Gd in GdTb alloys measured by MOKE rotation. Dashed lines are a guide to the eye while the solid lines are the fit to data to extract the  $T_C$ . The inset shows the Curie temperature  $T_C$  extracted from temperature-dependent results.  $T_C$  increases linearly with increasing Gd content in alloys.

Secondly, to check if the alloys are uniform with a common  $T_C$ , we measured the temperature dependence of magnetization for different concentration of Gd. Figure 8.2 shows the temperature dependence of magnetization normalized to the magnetization at 220 K. The magnetization was measured for two opposite directions of the saturation magnetic field. The temperature-dependent magnetization for pure Gd shows a behavior similar to the temperature-dependent magnetization calculated by the Brillouin function (figure 2.3 in chapter 2). With increasing Tb concentration the phase transition temperature  $T_C$  shifts to lower values. In order to determine the  $T_C$  quantitatively, temperature-dependent magnetization curves are fitted with the Bloch law ( $M/M_0 = 1 - (T/T_C)^{3/2}$ ), as shown by the solid lines in figure 8.2. The resulting values of  $T_C$  as a function of Gd atomic % are shown in the inset of figure 8.2. With substitution of the Tb the Curie temperature of the alloys decreases linearly from 293 K for pure Gd to 250 K for  $\text{Gd}_{30}\text{Tb}_{70}$  alloy. The line in the inset shows the function

$$T_C^x = \frac{xT_C^{\text{Gd}} + (100 - x)T_C^{\text{Tb}}}{100}. \quad (8.1)$$

In this equation  $x$  is the atomic % of Gd in alloys while  $T_C^{\text{Gd}}$  and  $T_C^{\text{Tb}}$  are the Curie tem-

## 8. Magnetization dynamics of the GdTb alloys

---

peratures of pure Gd and Tb metals, respectively. As is shown in figure 8.2 (inset), the equation 8.1 fits the experimental results reasonably. The  $T_C$  decreases almost linearly following our expectation since for pure Tb;  $T_C=220$  K and for pure Gd;  $T_C=293$  K. These results are also in agreement with the earlier observation on amorphous GdTb alloy films [151]. The MOKE signal decreases with decreasing temperature below about 220 K for the high Tb concentrations. The origin of this decrease in the MOKE signal is strong anisotropy of the Tb which increases coercivity of the system and requires stronger magnetic field to align all the spins in the field direction. This is also evident from the magnetic hysteresis curves in figure 8.1 where hystereses with high concentration of Tb are hardly saturated. This is a limitation on our experimental setup for the measurement of magnetization dynamics on GdTb alloys for higher Tb concentrations and at low equilibrium temperatures. Therefore, the magnetization dynamics was investigated at a fixed equilibrium temperature of 220 K, which can be easily saturated with available field and is reasonably below the measured Curie temperature of Gd<sub>30</sub>Tb<sub>70</sub> alloy of about 250 K.

The increase in the coercivity of the GdTb alloys and linear decrease of  $T_C$  with increasing Tb concentration confirms that the alloys are uniform with one  $T_C$  without forming the clusters of individual metal, and spin-orbit coupling of the GdTb alloy system changes the static magnetic properties. To investigate how this affects the dynamical magnetic properties, magnetization dynamics was studied as a function of concentration in GdTb alloys after fs laser excitation.

### 8.2 Concentration dependent laser-induced magnetization dynamics of GdTb alloys

For the study of the magnetization dynamics the GdTb alloy sample was excited with fs laser of 35 fs pulse duration with absorbed fluence of about  $1 \text{ mJ}/\text{cm}^2$ . The dynamics was investigated in the applied longitudinal magnetic field which can saturate the films in plane.

Figure 8.3 shows the time-dependent MOKE rotation, normalized to the MOKE signal before laser excitation, following fs laser excitation for different atomic % of Gd in GdTb alloys. Similar to the studies on pure Gd films (chapter 4), we can separate the different regions in the time-dependent signal for different concentrations



## 8.2 Concentration dependent magnetization dynamics of GdTb alloys

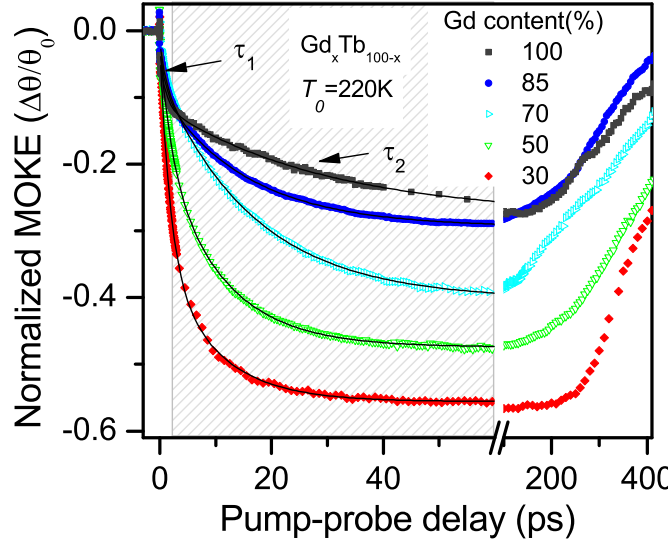


**Figure 8.3:** Time-dependent normalized MOKE signal for different atomic % of Gd in GdTb alloys at an equilibrium temperature of 220 K. The symbols are experimental results and lines are double exponential fit to the data. The demagnetization amplitude increases while the transients become fast with decreasing Gd concentration in alloys.

of alloys. (i) Ultrafast drop in the magnetization within the initial few ps after laser excitation. (ii) Slow demagnetization or quasi-equilibrium demagnetization emphasized by the hatched area. (iii) Recovery of magnetization after heat transfer from the experimentally investigated region to the substrate.

To quantitatively determine the time scale and amplitude of demagnetization, we used a double exponential fit of the form

$$\frac{\Delta\theta}{\theta_0} = \frac{\Delta M_1}{M} \left\{ 1 - e^{-\frac{(t-t_0)}{\tau_1}} \right\} + \frac{\Delta M_2}{M} \left\{ 1 - e^{-\frac{(t-t_0)}{\tau_2}} \right\} + C_0, \quad (8.2)$$

where  $\frac{\Delta M}{M}$  is the demagnetization amplitude,  $\tau$  demagnetization time,  $t_0$  time zero and  $C_0$  is the step demagnetization within the initial 150 fs; subscripts 1 and 2 are used for non-equilibrium (fast) and quasi-equilibrium (slow) demagnetization, respectively. The first part of the equation 8.2 represents demagnetization on the non-equilibrium time scale, i.e. about 1 ps, while the second part represents the quasi-equilibrium demagnetization when electron and phonon temperatures are equilibrated. With increasing Tb (or decreasing Gd) concentration in alloys one can observe three effects right away: (i) the magnitude of demagnetization increases; (ii) the demagnetization gets faster; and

## 8. Magnetization dynamics of the GdTb alloys

---

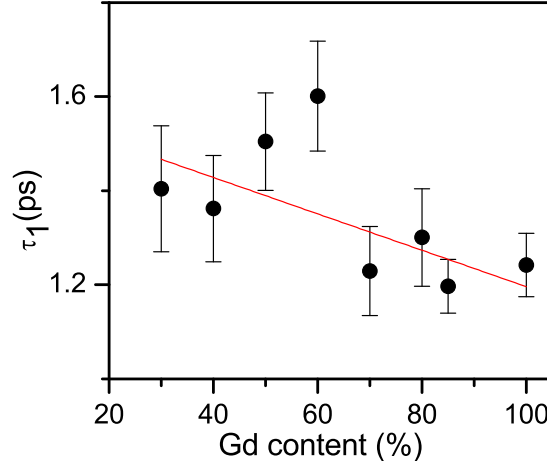


**Figure 8.4:** The non-equilibrium demagnetization time  $\tau_1$  as a function of Gd concentration in GdTb alloys. The dotted line is a linear fit to see the overall change in the demagnetization time as a function of concentration. The demagnetization time changes weakly with changing the concentration.

(iii) the recovery starts at longer time delays with increasing Tb concentration. All these time scales are quantitatively discussed in the following.

Figure 8.4 shows the dependence of non-equilibrium time  $\tau_1$  on the atomic % of Gd. The demagnetization time  $\tau_1$  shows a non-monotonic dependence on the concentration and slightly changes for the whole Gd concentration. Due to contributions within the initial few hundred fs, as discussed in section 6.2.1, it seems difficult to disentangle the contributions at the sub-picosecond time scale. With the conservative error bars the demagnetization time  $\tau_1$  weakly decreases with increasing the Gd concentration in the alloys. The overall change in  $\tau_1$  estimated by linear fit is about 3 fs/%(Gd). Since the dynamics in this regime is not changing strongly with the concentration, these results prove that the dynamics at this time scale is governed by the conduction electrons. Moreover, the conduction electron band structure is similar for Gd and Tb metals and we also expect it to be similar in alloys, following this the demagnetization slightly changes with concentration. The weak dependence of  $\tau_1$  on concentration is more than plausible because this time scale is smaller than the established spin-lattice relaxation time of both metals (as discussed in chapter 4 and 5).

The quasi-equilibrium demagnetization time  $\tau_2$  is shown as a function of Gd concentration in figure 8.5. The demagnetization time increases about 4 times from 9 ps

## 8.2 Concentration dependent magnetization dynamics of GdTb alloys

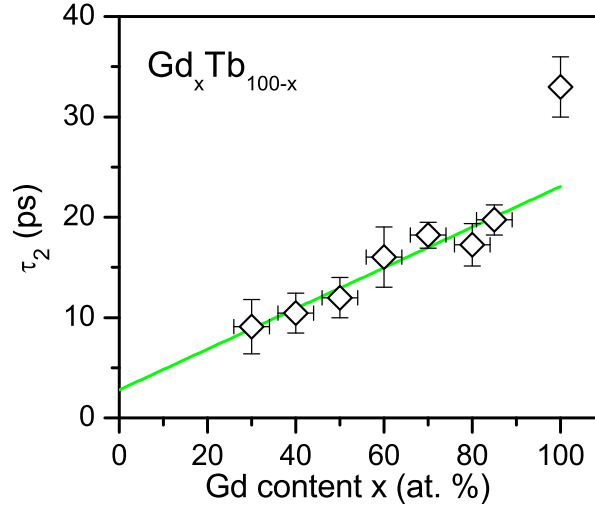


**Figure 8.5:** Concentration dependence of the quasi-equilibrium demagnetization time  $\tau_2$  of GdTb alloys. The time scale of demagnetization increases with Gd concentration following the decrease in the strength of the spin-orbit coupling of the system. For a few percent Tb impurities, the demagnetization time is strongly affected. The solid line is the linear fit to the  $\tau_2(x)$  for  $x \leq 85$ .

for  $\text{Gd}_{30}\text{Tb}_{70}$  to 33 ps for pure Gd. The increase in the demagnetization time is almost linear for Gd concentrations upto 85 at. %. A sizable increase in the demagnetization time can be seen within few percent of Tb in the alloys. The  $\tau_2$  is extrapolated to zero Gd concentration, for pure Tb this gives the value of demagnetization time of about 4 ps. This value is slightly lower than that of Tb metal (7 ps) measured by XMCD. The overall increase in the quasi-equilibrium demagnetization time is about 210 fs/%(Gd) which is fairly large and opposite as compared to the concentration dependence of non-equilibrium demagnetization. It should be noted that an anti-ferromagnetic phase exists in pure Tb between 220-229 K, this intermediary phase vanishes in GdTb alloys with even a few percent of Gd.

The observed concentration dependence of the  $\tau_2$  suggests that the spin-orbit coupling affects the quasi-equilibrium demagnetization. In addition to the linear dependence, the demagnetization time is strongly affected within the 15 % Tb concentration in the alloys. The origin of this non-linear dependence could also be the Tb induced anisotropy of the system. With the substitution of Tb the effective spin-orbit coupling will be defined by that of Tb. This channel is dominated even if there is only a few percent Tb in the alloys and the strength of this channel increases further with

## 8. Magnetization dynamics of the GdTb alloys

---

increasing the Tb content in the alloys. The strong change in magnetic anisotropy has already been confirmed by studying the static magnetic properties. Even only 1.8 % of Tb alloyed in Gd showed a sizeable increase in the spin-orbit coupling between Gd and Tb, as a result, the anisotropy of the system was increased by order of magnitude [10, 152]. The nonlinear concentration dependence of the magneto-crystalline anisotropy was also reported in the GdTb alloys [151]. Since the quasi-equilibrium demagnetization depends on the spin-orbit coupling as discussed in chapter 5 [33], the strong change in anisotropy even at very low Tb concentration provides sufficient bridging to transfer the angular momentum from spin-system to the lattice, which results in faster demagnetization.

The recovery of magnetization also starts at longer time delays with increasing Tb concentration. Since the  $T_C$  also decreases with an increase in the Tb concentration (figure 8.2). With increasing Tb concentration, after optical excitation, the system remains above  $T_C$  for longer time as well as contributions of spin fluctuations increase which slow down the recovery of the magnetization, in a similar manner as discussed in chapter 5 for Gd metals, where the magnetization recovery time was increased with increasing temperature.

### 8.3 Summary

Using the tunable spin-orbit coupling of the GdTb alloys, the static magnetic properties and magnetization dynamics for different concentrations of  $\text{Gd}_x\text{Tb}_{100-x}$  alloys is investigated. Measurements of magnetic hysteresis loops and the temperature-dependent magnetization of  $\text{Gd}_x\text{Tb}_{100-x}$  alloys with  $30 \leq x \leq 100$  are performed employing MOKE. A linear decrease in  $T_C$  is observed as a function of Tb concentration in the alloys (from 293 K for pure Gd to 250 K for  $\text{Gd}_{30}\text{Tb}_{70}$ ).

The laser-induced magnetization dynamics is also investigated from femto- to hundreds of picosecond time scale. Demagnetization becomes more efficient and faster with increasing the Tb content in the GdTb alloys.

The non-equilibrium demagnetization time  $\tau_1$  weakly depends on this concentration, with a higher Tb content it increases slightly. This is at the time scale of non-equilibrium dynamics i.e. a time scale faster than the equilibrium spin-orbit coupling. Therefore, it also confirms that at such an ultrafast time scale some other mechanism,

rather than the established spin-lattice relaxation, is responsible for demagnetization. The most important finding is the conduction electron mediated demagnetization. The  $\tau_1$  is similar for Gd and Tb metals as well as their alloys within experimental error bars. It stems from the similar conduction electron band structure of the Gd, Tb metals and their alloys.

Spin-orbit coupling affects the quasi-equilibrium demagnetization strongly. The quasi-equilibrium demagnetization time  $\tau_2$  increases about 6 times with increasing Gd concentration. However, this change is nonlinear, and can be attributed to the strong anisotropy of the system induced by Tb which provides the channel for the flow of angular momentum from the spin to the lattice system. Because of the strong change in  $\tau_2$ , it is concluded that this channel is active even for a very small concentration of Tb in the alloys.

## 8. Magnetization dynamics of the GdTb alloys

---

## Summary and outlook

In this thesis, the laser-induced magnetization dynamics of lanthanide ferromagnets is investigated to disentangle different microscopic contributions in temporal regimes down to the verge of the spin-orbit and exchange interaction. This is achieved by analyzing the magnetization dynamics of ferromagnetic Gd, Tb and their alloys by time-resolved techniques: X-ray magnetic circular dichroism (XMCD), magneto-optical Kerr effect (MOKE) and magnetic second harmonic generation (MSHG); following fs laser excitation of conduction electrons. In this chapter the essential conclusions are summarized. First, the experimental findings are presented then they are compared with the theoretical models.

The investigation begins with the femtosecond time-resolved XMCD experiments on Gd and Tb metals following fs laser excitation of conduction electrons, which give access to the localized  $4f$  magnetization dynamics. The time constants of demagnetization are analyzed for the strong direct spin-lattice coupling in Tb and the weaker indirect interaction in Gd. A novel mechanism of spin-lattice coupling is identified in both lanthanides. Compared to the established spin-lattice relaxation, which proceeds in Gd with a characteristic time of 40 ps (Tb: 8 ps), this novel type of angular momentum transfer to the lattice is active approximately at the time scale of the electron-phonon equilibration.

The magnetization dynamics is investigated in further detail employing time-resolved MOKE. Comparison of the dynamics studied by time-resolved XMCD and MOKE reveal that both  $4f$  and  $5d6s$  spin systems couple strongly through intra-atomic exchange interaction which prevails the concomitant demagnetization of these two sub-systems

## 9. Summary and outlook

---

down to the time scale of a few hundred femtoseconds. Moreover, different microscopic contributions in demagnetization are disentangled studying the dependency of magnetization dynamics on the equilibrium temperature and fluence. The discussion of the dynamics is separated into non-equilibrium and quasi-equilibrium demagnetization with characteristic time scales  $\tau_1$  and  $\tau_2$ , respectively, due to potentially different physical conditions for the demagnetization of the system in these two regimes.

By investigating the temperature dependence of the quasi-equilibrium ( $t \gg 1ps$ ) magnetization dynamics after fs laser excitation, the role of phonons and critical fluctuation is investigated. It is concluded that the demagnetization at this time scale is mainly controlled by spin-orbit coupling which is weak in Gd and thus sets a slower demagnetization timescale. The quasi-equilibrium demagnetization time ( $\tau_2$ ) changes weakly as  $T_0$  increases from 50 K to 230 K, showing a weak dependence on phonon population. From the observed experimental results it is concluded that the phonons play a dominant role only in the demagnetization amplitude. A possible reason for the weak temperature dependence of the demagnetization time could be the spin-lattice relaxation bottleneck. On the other hand, a strong increase of the demagnetization time is observed as the system approaches Curie temperature. After a power law analysis this behavior is attributed to the critical slowing down.

In order to understand the non-equilibrium dynamics ( $t \lesssim 1$  ps) and disentangle different microscopic processes within the first few picoseconds, the temperature dependence of demagnetization is carefully analyzed by MOKE rotation and ellipticity measurements. In this regime, a similar variation of the MOKE ellipticity and rotation is found, in agreement also with the time-resolved XMCD results. Therefore, this is assigned to the concomitant  $4f$  and  $5d6s$  magnetization dynamics dominated by the localized  $4f$  magnetic moments. In general, according to these observations a temperature increase results in a slower demagnetization. A two time increase in  $\tau_1$  is observed, from 0.8 ps at 50 K to 1.5 ps at 280 K. It is shown that these results can be described quantitatively employing modeling by the Landau-Lifshitz-Bloch equation; considering both microscopic electron- and phonon-mediated demagnetization processes. The conclusion is that at low temperatures, the experimentally determined demagnetization time can be modeled by considering electronic processes only. At temperatures above Debye temperature, phonon-mediated processes have to be taken into account to explain the further slowing down of the experimentally measured demagnetization.



---

Detailed comparison of MOKE ellipticity and rotation reveals the presence of time-dependent processes at early delays after laser excitations ( $t \leq 300fs$ ), when the excess energy resides predominantly in the electronic system. The temperature- and time-dependent MOKE ellipticity and rotation data exhibits a complex behavior within a few hundred femtoseconds directly after laser excitation. These effects can originate from the magnetic as well as non-magnetic contributions. For potential magnetic contributions it is suggested that the competition between angular momentum transfer from  $4f$  to  $5d6s$  and  $5d6s$  to the lattice leads to a transient spin polarization of conduction electrons. As a result, the MOKE rotation and ellipticity signal increases within a few hundred femtoseconds at low temperatures when phonons are not excited to compensate the angular momentum. This scenario is consistent with our experimental observations. However, due to a complex interplay of different processes contributing to the MOKE signal, it is beyond the resolution of our magneto-optical probe to discern the different contributions within the initial few hundred femtoseconds. These are new observations which require further experimental as well as theoretical investigation.

To check the tunability of the ultrafast magnetization dynamics through spin-orbit coupling, GdTb alloys are investigated. Upon analysis of the dynamics of GdTb alloys it is concluded that a stronger spin-orbit interaction speeds up the quasi-equilibrium demagnetization process. The non-equilibrium demagnetization, however, is almost independent of the spin-orbit coupling strength. The characteristic quasi-equilibrium demagnetization time increases six times by decreasing the Tb content from  $70 \geq \text{Tb}(\%) \geq 0$ .

Finally, our experimental results are compared with recent theoretical models which include the microscopic three temperature model (M3TM) [37] and the Landau-Lifshitz-Block (LLB) [36] equation. This comparison shows that both the M3TM and LLB model are partially in agreement with our experimental observations. The experimental results for quasi-equilibrium and non-equilibrium demagnetization are then compared separately with the theoretical models.

In the quasi-equilibrium demagnetization regime ( $t \gg 1ps$ ), the calculated demagnetization time by M3TM for  $s=1/2$  concurs with the experimental results at intermediate temperatures. However, the detailed temperature dependence is different from the experimental results both at low temperatures as well as at high temperatures

## 9. Summary and outlook

---

close to  $T_C$ . One potential origin of this deviation is that the critical spin fluctuations are not considered in this model. Moreover, it is suggested that an appropriate microscopic demagnetization mechanism with a temperature-dependent coupling parameter needs to be considered. The LLB model, on the other hand, with its general calculations of demagnetization rates shows the contribution of spin fluctuations which were also observed experimentally, but the absolute value of the characteristic time is at least two orders of magnitude smaller than the experimental one. For this model, the appropriate calculations with material-specific coupling parameters must be considered in order to explain the experimental results. Moreover, both models (LLB and M3TM) suggest a decrease in demagnetization time with increasing temperature below Debye temperature. This is in pronounced contrast to our experimental observations. The decrease in the relaxation time with increasing  $T_0$  is also expected from Hübner's calculations when one assumes a constant spin-orbit coupling (equation 2.23) [33] as a function of temperature. The weak dependence of experimentally measured quasi-equilibrium demagnetization time ( $\tau_2$ ) on equilibrium temperature suggests that: (i) the spin-orbit coupling may decrease with temperature which competes with the increase in the phonon population and (ii) a consideration of direct and indirect processes [33], in addition to the Raman type of process, may be important for a complete analysis.

Focusing on the dynamics in the non-equilibrium regime, a successful description was achieved by LLB modeling considering the temperature-dependent coupling with electrons and phonons. However, the explanation of the dynamics within the first few hundred femtoseconds needs further investigation. In principle a separate equation of motion for the spin polarization of  $5d6s$  electrons can be written, similar to Ref. [87]. For a microscopic description of processes directly after laser excitation, the derivation of a two-component LLB equation with a more appropriate treatment of  $d$ - $f$  exchange interaction is necessary. In this case one can deal with the angular momentum distribution between different spin sub-systems in different temporal regimes. Note that the consideration of the non-thermal distribution of electrons in the two temperature model [68] is also essential for the description of electron dynamics within the initial few hundred femtoseconds.

# Bibliography

- [1] C. D. STANCIU, F. HANSTEEN, A. V. KIMEL, A. KIRILYUK, A. TSUKAMOTO, A. ITOH, AND TH. RASING. **All-Optical Magnetic Recording with Circularly Polarized Light**. *Phys. Rev. Lett.*, **99**(4):047601, 2007. [1](#), [3](#)
- [2] T. A. OSTLER, J. BARKER, R. F. L. EVANS, R.W. CHANTRELL, U. ATXITIA, O. CHUBYKALO-FESENKO, S.E. MOUSSAOUI, L. L. GUYADER, E. MENGOTTI, L.J. HEYDERMAN, F. NOLTING, A. TSUKAMOTO, A. ITOH, D. AFANASIEV, AND B.A. IVANOV. **Ultrafast heating as a sufficient stimulus for magnetization reversal in a ferrimagnet**. *Nature Communications*, **3**:666, 2012. [1](#), [2](#), [3](#)
- [3] G.C. HADJIPANAYIS. *Magnetic storage systems beyond 2000*. Kluwer Academic Publishers, 2001. [1](#)
- [4] I. TUDOSA, C. STAMM, A. B. KASHUBA, F. KING, H. C. SIEGMANN, J. STÖHR, G. JU, B. LU, AND D. WELLER. **The ultimate speed of magnetic switching in granular recording media**. *Nature*, **428**:831, 2004. [1](#)
- [5] R. J. HICKEN. **Ultrafast nanomagnets: seeing data storage in a new light**. *Philosophical Transactions of the Royal Society of London. Series A: Mathematical, Physical and Engineering Sciences*, **361**(1813):2827–2841, 2003. [1](#)
- [6] A. VATERLAUS, T. BEUTLER, AND F. MEIER. **Spin-lattice relaxation time of ferromagnetic gadolinium determined with time-resolved spin-polarized photoemission**. *Phys. Rev. Lett.*, **67**:3314, 1991. [2](#), [3](#), [4](#), [6](#), [25](#), [26](#), [30](#), [63](#)

## BIBLIOGRAPHY

---

- [7] T. OGASAWARA, K. OHGUSHI, Y. TOMIOKA, K. S. TAKAHASHI, H. OKAMOTO, M. KAWASAKI, AND Y. TOKURA. **General Features of Photoinduced Spin Dynamics in Ferromagnetic and Ferrimagnetic Compounds.** *Phys. Rev. Lett.*, **94**(8):087202, 2005. [2](#), [4](#), [66](#)
- [8] A. MELNIKOV, H. PRIMA-GARCIA, M. LISOWSKI, T. GIESSEL, R. WEBER, R. SCHMIDT, C. GAHL, N. M. BULGAKOVA, U. BOVENSIEPEN, AND M. WEINELT. **Non-equilibrium magnetization dynamics of Gadolinium studied by magnetic linear dichroism in time-resolved 4f core-level photoemission.** *Phys. Rev. Lett.*, **100**:107202, 2008. [2](#), [63](#)
- [9] J. STÖHR AND H.C. SIEGMANN. *Magnetism: from fundamentals to nanoscale dynamics.* Springer series in solid-state sciences. Springer, 2006. [2](#), [13](#), [42](#)
- [10] S. CHIKAZUMI AND C.D. GRAHAM. *Physics of ferromagnetism.* International series of monographs on physics. Oxford University Press, 2009. [3](#), [15](#), [122](#)
- [11] A. V. KIMEL, A. KIRILYUK, P. A. USACHEV, R. V. PISAREV, A. M. BALBASHOV, AND TH. RASING. **Ultrafast non-thermal control of magnetization by instantaneous photomagnetic pulses.** *Nature*, **435**:655, 2005. [3](#)
- [12] I. RADU, G. WOLTERS DORF, M. KIESSLING, A. MELNIKOV, U. BOVENSIEPEN, J. U. THIELE, AND C. H. BACK. **Laser-Induced Magnetization Dynamics of Lanthanide-Doped Permalloy Thin Films.** *Phys. Rev. Lett.*, **102**:117201, 2009. [3](#)
- [13] E. BEAUREPAIRE, J.-C. MERLE, A. DAUNOIS, AND J.-Y. BIGOT. **Ultrafast Spin Dynamics in Ferromagnetic Nickel.** *Phys. Rev. Lett.*, **76**:4250, 1996. [4](#), [5](#), [24](#), [31](#), [63](#), [69](#)
- [14] J. HOHLFELD, E. MATTHIAS, R. KNORREN, AND K. H. BENNEMANN. **Nonequilibrium Magnetization Dynamics of Nickel.** *Phys. Rev. Lett.*, **78**(25):4861–4864, 1997. [4](#), [6](#)
- [15] A. SCHOLL, L. BAUMGARTEN, R. JACQUEMIN, AND W. EBERHARDT. **Ultrafast Spin Dynamics of Ferromagnetic Thin Films Observed by fs Spin-Resolved Two-Photon Photoemission.** *Phys. Rev. Lett.*, **79**:5146–5149, 1997. [4](#)

- [16] J. GÜDDE, U. CONRAD, V. JÄHNKE, J. HOHLFELD, AND E. MATTHIAS. **Magnetization dynamics of Ni and Co films on Cu(001) and of bulk nickel surfaces.** *Phys. Rev. B*, **59**:R6608–R6611, 1999. [4](#)
- [17] B. KOOPMANS, M. VAN KAMPEN, J. T. KOHLHEPP, AND W. J. M. JONGE. **Ultrafast Magneto-Optics in Nickel: Magnetism or Optics?** *Phys. Rev. Lett.*, **85**(4):844–847, 2000. [4](#), [7](#), [26](#), [38](#), [40](#), [61](#), [68](#), [91](#), [104](#), [106](#)
- [18] L. GUIDONI, E. BEAUREPAIRE, AND J. Y. BIGOT. **Magneto-optics in the Ultrafast Regime: Thermalization of Spin Populations in Ferromagnetic Films.** *Phys. Rev. Lett.*, **89**(1):017401, 2002. [4](#), [7](#), [38](#), [40](#), [61](#), [91](#), [104](#), [106](#)
- [19] P. M. OPPENEER AND A. LIEBSCH. **Ultrafast demagnetization in Ni: theory of magneto-optics for non-equilibrium electron distributions.** *Journal of Physics: Condensed Matter*, **16**(30):5519, 2004. [4](#), [7](#), [38](#), [40](#), [61](#), [91](#), [93](#), [104](#), [106](#), [112](#)
- [20] H. S. RHIE, H. A. DÜRR, AND W. EBERHARDT. **Femtosecond Electron and Spin Dynamics in Ni/W(110) Films.** *Phys. Rev. Lett.*, **90**:247201, 2003. [4](#), [63](#)
- [21] J. Y. BIGOT, M. VOMIR, L.H.F. ANDRADE, AND E. BEAUREPAIRE. **Ultrafast magnetization dynamics in ferromagnetic cobalt: The role of the anisotropy.** *Chemical Physics*, **318**(1-2):137 – 146, 2005. [4](#)
- [22] G. JU, J. HOHLFELD, B. BERGMAN, R. J. M. VAN DE VEERDONK, O. N. MRYASOV, J.-Y. KIM, X. WU, D. WELLER, AND B. KOOPMANS. **Ultrafast Generation of Ferromagnetic Order via a Laser-Induced Phase Transformation in FeRh Thin Films.** *Phys. Rev. Lett.*, **93**(19):197403, 2004. [4](#)
- [23] J. U. THIELE, M. BUSS, AND C. H. BACK. **Spin dynamics of the antiferromagnetic-to-ferromagnetic phase transition in FeRh on a sub-picosecond time scale.** *Applied Physics Letters*, **85**(14):2857–2859, 2004. [4](#)
- [24] J. Y. BIGOT, M. VOMIR, AND E. BEAUREPAIRE. **Coherent ultrafast magnetism induced by femtosecond laser pulses.** *Nat. Phys.*, **5**(7):515, 2009. [4](#), [30](#), [65](#), [106](#)

## BIBLIOGRAPHY

---

- [25] G. P. ZHANG, W. HÜBNER, G. LEFKIDIS, Y. BAI, AND T. F. GEORGE. **Paradigm of the time-resolved magneto-optical Kerr effect for femtosecond magnetism.** *Nature Physics*, **5**:499, 2009. [4](#)
- [26] M. BATTIATO, K. CARVA, AND P. M. OPPENEER. **Superdiffusive Spin Transport as a Mechanism of Ultrafast Demagnetization.** *Phys. Rev. Lett.*, **105**(2):027203, 2010. [4](#), [5](#), [29](#), [65](#), [97](#), [106](#), [113](#)
- [27] U. BOVENSIEPEN. **Coherent and incoherent excitations of the Gd(0001) surface on ultrafast timescales.** *J. Phys.: Cond. Matter*, **19**:083201, 2007. [4](#), [6](#), [20](#), [22](#), [59](#), [63](#), [65](#), [79](#), [88](#), [92](#), [98](#)
- [28] A. F. BARTELT, A. COMIN, J. FENG, J. R. NASIATKA, T. EIMÜLLER, B. LUDESCHER, G. SCHÜTZ, H. A. PADMORE, A. T. YOUNG, AND A. SCHOLL. **Element-specific spin and orbital momentum dynamics of Fe/Gd multilayers.** *Appl. Phys. Lett.*, **90**:162503, 2007. [4](#), [64](#)
- [29] J. WALOWSKI, G. MÜLLER, M. DJORDJEVIC, M. MÜNZENBERG, M. KLÄUI, C. A. F. VAZ, AND J. A. C. BLAND. **Energy Equilibration Processes of Electrons, Magnons, and Phonons at the Femtosecond Time Scale.** *Phys. Rev. Lett.*, **101**:237401, 2008. [4](#), [29](#)
- [30] G. MALINOWSKI, F. DALLA LONGA, J. H. H. RIETJENS, P. V. PALUSKAR, R. HUIJINK, H. J. M. SWAGTEN, AND B. KOOPMANS. **Control of speed and efficiency of ultrafast demagnetization by direct transfer of spin angular momentum.** *Nat. Phys.*, **4**:855, 2008. [4](#), [6](#)
- [31] G. M. MÜLLER, J. WALOWSKI, M. DJORDJEVIC, G.-X. MIAO, A. GUPTA, A. V. RAMOS, K. GEHRKE, V. MOSHNYAGA, KONRAD SAMWER, JAN SCHMALHORST, A. THOMAS, A. HÜTTEN, G. REISS, J. S. MOODERA, AND MARKUS MÜNZENBERG. **Spin polarization in half-metals probed by femtosecond spin excitation.** *Nature Materials*, **8**:56, 2009. [4](#)
- [32] J. W. KIM, K.-D. LEE, J.-W. JEONG, AND S.-C. SHIN. **Ultrafast spin demagnetization by nonthermal electrons of TbFe alloy film.** *Appl. Phys. Lett.*, **94**:192506, 2009. [4](#), [65](#)

- [33] W. HÜBNER AND K. H. BENNEMANN. **Simple theory for spin-lattice relaxation in metallic rare-earth ferromagnets.** *Phys. Rev. B*, **53**(6):3422–3427, 1996. [4](#), [6](#), [26](#), [27](#), [30](#), [63](#), [65](#), [69](#), [82](#), [97](#), [99](#), [100](#), [122](#), [128](#)
- [34] B. KOOPMANS, H.H.J.E. KICKEN, M. VAN KAMPEN, AND W.J.M. DE JONGE. **Microscopic model for femtosecond magnetization dynamics.** *Journal of Magnetism and Magnetic Materials*, **286**:271 – 275, 2005. Proceedings of the 5th International Symposium on Metallic Multilayers. [5](#), [29](#), [32](#), [78](#)
- [35] U. ATXITIA, O. CHUBYKALO-FESENKO, N. KAZANTSEVA, D. HINZKE, U. NOWAK, AND R. W. CHANTRELL. **Micromagnetic modeling of laser-induced magnetization dynamics using the Landau-Lifshitz-Bloch equation.** *Appl. Phys. Lett.*, **91**:232507, 2007. [5](#), [96](#), [98](#)
- [36] U. ATXITIA AND O. CHUBYKALO-FESENKO. **Ultrafast magnetization dynamics rates within the Landau-Lifshitz-Bloch model.** *Phys. Rev. B*, **84**:144414, 2011. [5](#), [7](#), [32](#), [33](#), [34](#), [78](#), [79](#), [98](#), [102](#), [127](#)
- [37] B. KOOPMANS, G. MALINOWSKI, F. DALLA, D. STEIAUF, M. FÄHNLE, T. ROTH, M. CINCHETTI, AND M. AESCHLIMANN. **Explaining the paradoxical diversity of ultrafast laser-induced demagnetization.** *Nature Materials*, **9**:259, 2010. [5](#), [7](#), [28](#), [31](#), [65](#), [69](#), [77](#), [78](#), [88](#), [97](#), [102](#), [127](#)
- [38] S. ESSERT AND H. C. SCHNEIDER. **Electron-phonon scattering dynamics in ferromagnetic metals and their influence on ultrafast demagnetization processes.** *Phys. Rev. B*, **84**:224405, 2011. [5](#), [29](#)
- [39] B. KOOPMANS, J. J. M. RUIGROK, F. DALLA LONGA, AND W. J. M. DE JONGE. **Unifying Ultrafast Magnetization Dynamics.** *Phys. Rev. Lett.*, **95**:267207, 2005. [6](#), [29](#)
- [40] C. STAMM, T. KACHEL, N. PONTIUS, R. MITZNER, T. QUAST, K. HOLLDACK, S. KHAN, C. LUPULESCU, E. F. AZIZ, M. WIETSTRUK, H. A. DÜRR, AND W. EBERHARDT. **Femtosecond modification of electron localization and transfer of angular momentum in nickel.** *Nature Materials*, **6**:740, 2007. [6](#), [57](#), [69](#)

## BIBLIOGRAPHY

---

- [41] M. LISOWSKI. **Elektronen- und Magnetisierungsdynamik in Metallen untersucht mit zeitaufgelöster Photoemission.** *PhD Thesis, FU Berlin* <http://www.diss.fu-berlin.de/2006/9/>, 2005. 6, 14, 18, 21, 23, 59, 67, 92, 98
- [42] I. E. RADU. **Ultrafast Electron, Lattice and Spin Dynamics on Rare-Earth Metal Surfaces.** *PhD Thesis, FU Berlin* <http://www.diss.fu-berlin.de/2006/342/>, 2006. 6, 22, 24, 39, 40, 47, 50, 55
- [43] A. MELNIKOV, I. RADU, A. POVOLOTSKIY, T. WEHLING, A. LICHTENSTEIN, AND U. BOVENSIEPEN. **Ultrafast dynamics at lanthanide surfaces: microscopic interaction of the charge, lattice and spin subsystems.** *J. Phys. D: Appl. Phys.*, **41**:164004, 2008. 6, 56, 110, 111
- [44] S. Y. DAN'KOV, A. M. TISHIN, V. K. PECHARSKY, AND K. A. GSCHNEIDNER. **Magnetic phase transitions and the magnetothermal properties of gadolinium.** *Phys. Rev. B*, **57**(6):3478–3490, 1998. 7, 14
- [45] K.H.J. BUSCHOW AND F.R. BOER. *Physics of magnetism and magnetic materials.* Focus on biotechnology. Kluwer Academic/Plenum Publishers, 2003. 10
- [46] B. COQBLIN. *The electronic structure of rare-earth metals and alloys.* Academic Press, London and New York, 1977. 10, 12, 13, 15, 16, 17, 23
- [47] B. N. HARMON AND A. J. FREEMAN. **Spin-polarized energy-band structure, conduction-electron polarization, spin densities, and the neutron magnetic form factor of ferromagnetic gadolinium.** *Phys. Rev. B*, **10**:1979–1993, 1974. 11
- [48] J.M.D. COEY. *Magnetism and magnetic materials.* Cambridge University Press, 2010. 11
- [49] M. LARIDJANI AND J.F. SADOE. **Structure study of amorphous Gd-Y Alloys.** *J. Phys. France*, **42**(9):1293–1298, 1981. 11
- [50] S. BLUNDELL. *Magnetism in condensed matter.* oxford master. Oxford University Press, 2001. 12, 15, 32



- [51] K. A. GSCHNEIDNER AND J. L. EYRING. *Handbook on the Physics and Chemistry of Rare Earths, volume 24*. Elsevier, 1997. [12](#), [16](#)
- [52] R. AHUJA, S. AULUCK, B. JOHANSSON, AND M. S. S. BROOKS. **Electronic structure, magnetism, and Fermi surfaces of Gd and Tb**. *Phys. Rev. B*, **50**:5147–5154, 1994. [12](#), [68](#), [70](#), [105](#)
- [53] M. COLARIETI-TOSTI, S. I. SIMAK, R. AHUJA, L. NORDSTRÖM, O. ERIKSSON, D. ÅBERG, S. EDVARDSSON, AND M. S. S. BROOKS. **Origin of Magnetic Anisotropy of Gd Metal**. *Phys. Rev. Lett.*, **91**:157201, 2003. [13](#)
- [54] J. M. YEOMANS. *Statistical Mechanics of Phase Transitions*. Oxford University Press Inc., New York, 1992. [15](#)
- [55] M. GETZLAFF. *Fundamentals of Magnetism*. Springer, 2008. [15](#)
- [56] A. R. CHOWDHURY, G. S. COLLINS, AND C. HOHENEMSER. **Anomalous critical spin dynamics in Gd: A revision**. *Phys. Rev. B*, **33**(7):5070–5072, 1986. [16](#), [75](#), [76](#)
- [57] C. KITTEL. *Introduction to solid state physics*. Wiley, 1996. [16](#)
- [58] M. WIETSTRUK, A. MELNIKOV, C. STAMM, T. KACHEL, N. PONTIUS, M. SULTAN, C. GAHL, M. WEINELT, H. A. DÜRR, AND U. BOVENSIEPEN. **Hot-Electron-Driven Enhancement of Spin-Lattice Coupling in Gd and Tb 4f Ferromagnets Observed by Femtosecond X-Ray Magnetic Circular Dichroism**. *Phys. Rev. Lett.*, **106**(12):127401, 2011. [16](#), [62](#), [64](#), [68](#), [79](#), [104](#)
- [59] W. C. KOEHLER. **Magnetic Properties of Rare-Earth Metals and Alloys**. *J. Appl. Phys.*, **36**:1078, 1965. [17](#), [23](#)
- [60] J. JENSEN AND A.R. MACKINTOSH. *Rare earth magnetism: structures and excitations*. International series of monographs on physics. Clarendon Press, 1991. [17](#)
- [61] A. BERGER, A.W. PANG, AND H. HOPSTER. **Magnetic reorientation transition in epitaxial Gd-films**. *Journal of Magnetism and Magnetic Materials*, **137**(1-2):L1 – L5, 1994. [17](#), [67](#)

## BIBLIOGRAPHY

---

- [62] M. FARLE, A. BERGHAUS, AND K. BABERSCHKE. **Magnetic anisotropy of Gd(0001)/W(110) monolayers.** *Phys. Rev. B*, **39**:4838–4841, 1989. [17](#)
- [63] A. BORISOV, S. SÁNCHEZ-PORTAL, R. DíEZ MUIÑO, AND P. M. ECHENIQUE. **Building up the screening below the femtosecond scale.** *Chem. Phys. Lett.*, **387**:95, 2004. [18](#), [112](#)
- [64] D. PINES AND P. NOZIÈRES. *The theory of quantum liquids*. Number v. 1 in The Theory of Quantum Liquids. W.A. Benjamin, 1966. [19](#)
- [65] GRIMVALL G. *The Electron-Phonon Interaction in Metals*. North-Holland, New-York, 1981. [20](#)
- [66] S. I. ANISIMOV, B. L. KAPELIOVICH, AND T.L. PERELMAN. **Electron emission from metal surfaces exposed to ultrashort laser pulses.** *Sov. Phys. JETP*, **39**:375, 1974. [21](#), [88](#)
- [67] P. JACOBSSON AND B. SUNDQVIST. **Thermal conductivity and electrical resistivity of gadolinium as functions of pressure and temperature.** *Phys. Rev. B*, **40**:9541–9551, 1989. [21](#)
- [68] R. H. M. GROENEVELD, R. SPRIK, AND A. LAGENDIJK. **Femtosecond spectroscopy of electron-electron and electron-phonon energy relaxation in Ag and Au.** *Phys. Rev. B*, **51**:11433–11445, 1995. [23](#), [24](#), [88](#), [128](#)
- [69] W. MARTIENSSEN AND H. WARLIMONT. *Springer handbook of condensed matter and materials data*. Number XVII in Springer handbook. Springer, 2005. [23](#)
- [70] H. SCHÖBER AND P. DEDERICHS. *Phonon States of Elements. Electron States and Fermi Surfaces of Alloys*. New Series Group III Condensed Matter. Springer-Verlag GmbH, 1981. [23](#)
- [71] S. ABDELOUAHED AND M. ALOUANI. **Magnetic anisotropy in Gd, GdN, and GdFe<sub>2</sub> tuned by the energy of gadolinium 4f states.** *Phys. Rev. B*, **79**:054406, 2009. [23](#)
- [72] S. D. BRORSON, J. G. FUJIMOTO, AND E. P. IPPEN. **Femtosecond electronic heat-transport dynamics in thin gold films.** *Phys. Rev. Lett.*, **59**(17):1962–1965, 1987. [24](#), [111](#)

- [73] P. B. CORKUM, F. BRUNEL, N. K. SHERMAN, AND T. SRINIVASAN-RAO. **Thermal Response of Metals to Ultrashort-Pulse Laser Excitation.** *Phys. Rev. Lett.*, **61**:2886–2889, 1988. [24](#)
- [74] Y. EZZAHRI AND A. SHAKOURI. **Ballistic and diffusive transport of energy and heat in metals.** *Phys. Rev. B*, **79**:184303, 2009. [24](#)
- [75] F. DALLA LONGA, J. T. KOHLHEPP, W. J. M. DE JONGE, AND B. KOOPMANS. **Influence of photon angular momentum on ultrafast demagnetization in nickel.** *Phys. Rev. B*, **75**(22):224431, 2007. [25](#), [26](#)
- [76] G. P. ZHANG AND THOMAS F. GEORGE. **Total angular momentum conservation in laser-induced femtosecond magnetism.** *Phys. Rev. B*, **78**(5):052407, 2008. [25](#)
- [77] C. ZENER. **Interaction Between the  $d$  Shells in the Transition Metals.** *Phys. Rev.*, **81**:440–444, 1951. [27](#)
- [78] S. V. VONSOVSKII. *Magnetism*. Wiley, New York, 1974. [27](#)
- [79] J. WANG, C. SUN, J. KONO, A. OIWA, H. MUNEKATA, L. CYWIŃSKI, AND L. J. SHAM. **Ultrafast Quenching of Ferromagnetism in InMnAs Induced by Intense Laser Irradiation.** *Phys. Rev. Lett.*, **95**:167401, 2005. [27](#), [105](#), [106](#)
- [80] J. WANG, C. SUN, Y. HASHIMOTO, J. KONO, G. A. KHODAPARAST, L. CYWIŃSKI, L. J. SHAM, G. D. SANDERS, C. J. STANTON, AND H. MUNEKATA. **Ultrafast magneto-optics in ferromagnetic IIIIV semiconductors.** *Journal of Physics: Condensed Matter*, **18**(31):R501, 2006. [27](#), [28](#), [105](#), [106](#)
- [81] L. CYWIŃSKI AND L. J. SHAM. **Ultrafast demagnetization in the  $sp$ - $d$  model: A theoretical study.** *Phys. Rev. B*, **76**:045205, 2007. [27](#), [28](#), [97](#), [99](#), [105](#), [106](#)
- [82] J. K. FURDYNA. **Diluted magnetic semiconductors.** *Journal of Applied Physics*, **64**(4):R29–R64, 1988. [27](#)
- [83] R. J. ELLIOTT. **Effect of Spin-orbit Coupling on Paramagnetic Resonance in Semi-conductors.** *Phys. Rev.*, **96**:266, 1954. [28](#)

## BIBLIOGRAPHY

---

- [84] Y. YAFET. **g Factors and Spin-Lattice Relaxation of Conduction Electrons.** *Solid State Phys.*, **14**:1, 1963. [28](#)
- [85] D. STEIAUF, C. ILLG, AND M. FÄHNLE. **Extension of Yafet’s theory of spin relaxation to ferromagnets.** *Journal of Magnetism and Magnetic Materials*, **322**(6):L5 – L7, 2010. [28](#), [29](#)
- [86] A. MELNIKOV, I. RAZDOLSKI, T. O. WEHLING, EV. TH. PAPAIOANNOU, V. RODDATIS, P. FUMAGALLI, O. AKTSIPETROV, A. I. LICHTENSTEIN, AND U. BOVENSIEPEN. **Ultrafast Transport of Laser-Excited Spin-Polarized Carriers in Au/Fe/MgO(001).** *Phys. Rev. Lett.*, **107**:076601, 2011. [29](#)
- [87] J. SEIB AND M. FÄHNLE. **Calculation of the Gilbert damping matrix at low scattering rates in Gd.** *Phys. Rev. B*, **82**:064401, 2010. [32](#), [128](#)
- [88] D. A. GARANIN. **Generalized equation of motion for a ferromagnet.** *Physica A*, **172**:470, 1991. [32](#), [33](#), [98](#)
- [89] M. FARLE. **Ferromagnetic resonance of ultrathin metallic layers.** *Rep. Prog. Phys.*, **61**:755, 1998. [34](#)
- [90] B. HILLEBRANDS AND G. GÜNTHERODT. *Ultrathin magnetic structures*, **2**. Springer, Berlin, 1994. [34](#)
- [91] H. A. MOOK. **Neutron scattering studies of the high temperature spin dynamics of ferromagnetic materials.** *J. Magn. Magn. Mat.*, **31**:305, 1983. [34](#)
- [92] B. KOOPMANS. *Spin dynamics in confined magnetic structures II*, **87** of *Topics in Applied Physics*. Springer, Berlin, 2003. [34](#), [35](#), [38](#), [53](#)
- [93] BURKARD HILLEBRANDS. **Ultrafast magnetization processes.** *Journal of Physics D: Applied Physics*, **41**(16):160301, 2008. [34](#)
- [94] A. KIRILYUK, A. V. KIMEL, AND T. RASING. **Ultrafast optical manipulation of magnetic order.** *Rev. Mod. Phys.*, **82**(3):2731–2784, 2010. [34](#)
- [95] D.L. MILLS. *Nonlinear optics: basic concepts*. Springer, 1998. [34](#), [36](#)

- [96] Y.R. SHEN. *The principles of nonlinear optics*. Wiley classics library. Wiley-Interscience, 2003. [34](#), [35](#), [36](#)
- [97] A. K. ZVEZDIN, A.K. ZVEZDIN, V.A. KOTOV, AND V.A. KOTOV. *Modern magnetooptics and magneto-optical materials*. Studies in condensed matter physics. Institute of Physics Pub., 1997. [35](#)
- [98] K.H. BENNEMANN. *Nonlinear optics in metals*. International series of monographs on physics. Clarendon Press, 1998. [36](#), [37](#), [42](#)
- [99] U. PUSTOGOWA, W. HÜBNER, AND K. H. BENNEMANN. **Enhancement of the magneto-optical Kerr angle in nonlinear optical response**. *Phys. Rev. B*, **49**:10031–10034, 1994. [37](#)
- [100] P. A. FRANKEN, A. E. HILL, C. W. PETERS, AND G. WEINREICH. **Generation of Optical Harmonics**. *Phys. Rev. Lett.*, **7**:118–119, 1961. [39](#)
- [101] C. RULLIÈRE. *Femtosecond laser pulses: principles and experiments*. Advanced texts in physics. Springer, 2005. [39](#)
- [102] M. MANSURIPUR. *The physical principles of magneto-optical recording*. Cambridge University Press, 1998. [40](#)
- [103] Z. Q. QIU AND S. D. BADER. **Surface magneto-optic Kerr effect**. *Review of Scientific Instruments*, **71**(3):1243–1255, 2000. [40](#)
- [104] I. TUREK, J. KUDRNOVSKY, G. BIHLMAYER, AND S. BLÜGEL. **Ab initio theory of exchange interactions and the Curie temperature of bulk Gd**. *Journal of Physics: Condensed Matter*, **15**(17):2771, 2003. [41](#)
- [105] J. J. REHR AND R. C. ALBERS. **Theoretical approaches to x-ray absorption fine structure**. *Rev. Mod. Phys.*, **72**:621–654, 2000. [41](#)
- [106] J. STÖHR. *NEXAFS spectroscopy*. Springer series in surface sciences. Springer-Verlag, 1992. [41](#)
- [107] A.S. SCHLACHTER, F.J. WUILLEUMIER, AND NORTH ATLANTIC TREATY ORGANIZATION. SCIENTIFIC AFFAIRS DIVISION. *New directions in research with*

## BIBLIOGRAPHY

---

- third-generation soft x-ray synchrotron radiation sources*. NATO ASI series: Applied sciences. Kluwer Academic, 1994. [42](#)
- [108] P. BRUNO, Y. SUZUKI, AND C. CHAPPERT. **Magneto-optical Kerr effect in a paramagnetic overlayer on a ferromagnetic substrate: A spin-polarized quantum size effect**. *Phys. Rev. B*, **53**:9214–9220, 1996. [42](#)
- [109] B. T. THOLE, P. CARRA, F. SETTE, AND G. VAN DER LAAN. **X-ray circular dichroism as a probe of orbital magnetization**. *Phys. Rev. Lett.*, **68**:1943–1946, 1992. [42](#)
- [110] Y. TERAMURA, A. TANAKA, B. T. THOLE, AND TAKEO JO. **Effect of Coulomb Interaction on the X-Ray Magnetic Circular Dichroism Spin Sum Rule in Rare Earths**. *Journal of the Physical Society of Japan*, **65**(9):3056–3059, 1996. [42](#)
- [111] A. ZANGWILL. *Physics at surfaces*. Cambridge University Press, 1988. [45](#)
- [112] D. WELLER AND S. F. ALVARADO. **Preparation of remanently ferromagnetic Gd(0001)**. *J. Appl. Phys.*, **59**(8):2908–2913, 1986. [49](#)
- [113] A. ASPELMEIER, F. GERHARDTER, AND K. BABERSCHKE. **Magnetism and structure of ultrathin Gd films**. *J. Magn. Magn. Mat.*, **132**(1):22, 1994. [49](#)
- [114] MOULTON P. F. **Spectroscopic and laser characteristics of Ti:Al–2O–3**. *J. Opt. Soc. Am. B*, **3**:125, 1986. [50](#)
- [115] UWE CONRAD. **Statische und dynamische untersuchungen ultraduenner metallfilme mit optischer frequenzverdopplung und nichtlineare mikroskopie**. *PhD Thesis, FU Berlin*, 1999. [53](#)
- [116] M. VAN KAMPEN, C. JOZSA, J. T. KOHLHEPP, P. LECLAIR, L. LAGAE, W. J. M. DE JONGE, AND B. KOOPMANS. **All-Optical Probe of Coherent Spin Waves**. *Phys. Rev. Lett.*, **88**:227201, 2002. [53](#)
- [117] M. SULTAN, A. MELNIKOV, AND U. BOVENSIEPEN. **Ultrafast magnetization dynamics of Gd(0001): Bulk versus surface**. *Physica Status Solidi (b)*, **248**(10):2323, 2011. [53](#), [86](#), [87](#), [89](#), [110](#)

- [118] M. ABO-BAKR, J. FEIKES, K. HOLLDACK, G. WÜSTEFELD, AND H.-W. HÜBERS. **Steady-State Far-Infrared Coherent Synchrotron Radiation detected at BESSY II.** *Phys. Rev. Lett.*, **88**:254801, 2002. [56](#), [62](#)
- [119] R. W. SCHOENLEIN, S. CHATTOPADHYAY, H. H. W. CHONG, T. E. GLOVER, P. A. HEIMANN, C. V. SHANK, A. A. ZHOLENTS, AND M. S. ZOLOTOREV. **Generation of Femtosecond Pulses of Synchrotron Radiation.** *Science*, **287**:2237, 2000. [57](#)
- [120] QUAST T., FIRSOV A., HOLLDACK K., KHAN S., AND MITZNER R. **Upgrade of the BESSY femtoslicing source.** *Proceedings of PAC07, Albuquerque, New Mexico, USA*, pages 950–952, 2007. [57](#)
- [121] A. ERKO, A. FIRSOV, AND K. HOLLDACK. **New Developments in Femtosecond Soft X-ray Spectroscopy.** *AIP Conference Proceedings*, **1234**(1):177–180, 2010. [57](#)
- [122] MARKO WIETSTRUK. **Ultraschnelle Magnetisierungsdynamik in itineranten und Heisenberg-Ferromagneten.** *PhD Thesis, TU Berlin* <http://opus.kobv.de/tuberlin/volltexte/2010/2684/>, 2010. [60](#), [62](#), [64](#), [65](#)
- [123] J. L. ERSKINE AND E. A. STERN. **Magneto-Optic Kerr Effects in Gadolinium.** *Phys. Rev. B*, **8**:1239, 1973. [61](#)
- [124] J. L. ERSKINE. **Magneto-optical Study of Gd Using Synchrotron Radiation.** *Phys. Rev. Lett.*, **37**:157, 1976. [61](#)
- [125] K. STARKE, F. HEIGL, A. VOLLMER, M. WEISS, G. REICHARDT, AND G. KAINDL. **X-Ray Magneto-optics in Lanthanides.** *Phys. Rev. Lett.*, **86**:3415–3418, 2001. [61](#)
- [126] A. MELNIKOV, O. KRUPIN, U. BOVENSIEPEN, K. STARKE, M. WOLF, AND E. MATTHIAS. **SHG on ferromagnetic Gd films: indication of surface-state effects.** *Appl. Phys. B*, **74**(15):723, 2002. [67](#)
- [127] G. S. COLLINS, A. R. CHOWDHURY, AND C. HOHENEMSER. **Observation of isotropic critical spin fluctuations in Gd.** *Phys. Rev. B*, **33**(7):4747–4751, 1986. [76](#)

## BIBLIOGRAPHY

---

- [128] P. D. DE RÉOTIER AND A. YAOUANC. **Possibility of observation of the critical paramagnetic longitudinal spin fluctuations in gadolinium by muon spin rotation spectroscopy.** *Phys. Rev. Lett.*, **72**(2):290–293, 1994. [76](#)
- [129] E. FREY, F. SCHWABL, S. HENNEBERGER, O. HARTMANN, R. WÄPPLING, A. KRATZER, AND G. M. KALVIUS. **Determination of the Universality Class of Gadolinium.** *Phys. Rev. Lett.*, **79**(25):5142–5145, 1997. [76](#), [77](#)
- [130] A. K. MURTAZAEV AND V. A. MUTAILAMOV. **Dynamic Critical Behavior in Models of Ferromagnetic Gadolinium.** *Journal of Experimental and Theoretical Physics*, **101**(2):299–304, 2005. [76](#)
- [131] K.A. GSCHNEIDNER, L.R. EYRING, AND GERRY H. LANDER. *Handbook on the Physics and Chemistry of Rare Earths, Volume 32.* Elsevier, 2001. [77](#)
- [132] U. ATXITIA, O. CHUBYKALO-FESENKO, J. WALOWSKI, A. MANN, AND M. MÜNZENBERG. **Evidence for thermal mechanisms in laser-induced femtosecond spin dynamics.** *Phys. Rev. B*, **81**(17):174401, 2010. [78](#), [82](#), [87](#), [88](#), [96](#), [97](#), [98](#)
- [133] O. CHUBYKALO-FESENKO, U. NOWAK, R. W. CHANTRELL, AND D. GARANIN. **Dynamic approach for micromagnetics close to the Curie temperature.** *Phys. Rev. B*, **74**(9):094436, 2006. [78](#), [102](#)
- [134] N. KAZANTSEVA, U. NOWAK, R. W. CHANTRELL, J. HOHLFELD, AND A. REBEL. **Slow recovery of the magnetisation after a sub-picosecond heat pulse.** *EPL (Europhysics Letters)*, **81**(2):27004, 2008. [82](#), [96](#)
- [135] L. XIAODONG, X. ZHEN, G. RUIXIN, H. HAINING, C. ZHIFENG, W. ZIXIN, JUN D., Z. SHIMING, AND L. TIANSHU. **Dynamics of magnetization, reversal, and ultrafast demagnetization of TbFeCo amorphous films.** *Appl. Phys. Lett.*, **92**:232501, 2008. [82](#)
- [136] M. SULTAN, U. ATXITIA, A. MELNIKOV, O. CHUBYKALO-FESENKO, AND U. BOVENSIEPEN. **Electron- and phonon-mediated ultrafast magnetization dynamics of Gd(0001).** *Submitted*, 2012. [90](#), [91](#), [93](#), [94](#), [97](#), [100](#)



- [137] W. NOLTING, T. DAMBECK, AND G. BORSTEL. **Temperature-dependent electronic structure of gadolinium.** *Zeitschrift für Physik B Condensed Matter*, **94**:409–421, 1994. [93](#)
- [138] K. MAITI, M. C. MALAGOLI, A. DALLMEYER, AND C. CARBONE. **Finite Temperature Magnetism in Gd: Evidence against a Stoner Behavior.** *Phys. Rev. Lett.*, **88**:167205, 2002. [93](#)
- [139] The original schematic of the LLB model was courtesy of Unai Atxitia CSIC, Madrid Spain. [97](#)
- [140] K. VAHAPLAR, A. M. KALASHNIKOVA, A. V. KIMEL, D. HINZKE, U. NOWAK, R. CHANTRELL, A. TSUKAMOTO, A. ITOH, A. KIRILYUK, AND TH. RASING. **Ultrafast Path for Optical Magnetization Reversal via a Strongly Nonequilibrium State.** *Phys. Rev. Lett.*, **103**(11):117201, 2009. [96](#)
- [141] N. KAZANTSEVA, D. HINZKE, R. W. CHANTRELL, AND U. NOWAK. **Linear and elliptical magnetization reversal close to the Curie temperature.** *EPL (Europhysics Letters)*, **86**(2):27006, 2009. [97](#), [102](#)
- [142] N. KAZANTSEVA, D. HINZKE, U. NOWAK, R. W. CHANTRELL, U. ATXITIA, AND O. CHUBYKALO-FESENKO. **Towards multiscale modeling of magnetic materials: Simulations of FePt.** *Phys. Rev. B*, **77**:184428, 2008. [98](#)
- [143] J. H. MENTINK, J. HELLSVIK, D. V. AFANASIEV, B. A. IVANOV, A. KIRILYUK, A. V. KIMEL, O. ERIKSSON, M. I. KATSNELSON, AND TH. RASING. **Ultrafast Spin Dynamics in Multisublattice Magnets.** *Phys. Rev. Lett.*, **108**:057202, 2012. [105](#), [106](#)
- [144] A. MELNIKOV, I. RADU, U. BOVENSIEPEN, O. KRUPIN, K. STARKE, E. MATTHIAS, AND M. WOLF. **Coherent optical phonons and parametrically coupled magnons induced by femtosecond laser excitation of the Gd(0001) surface.** *Phys. Rev. Lett.*, **91**:227403, 2003. [110](#)
- [145] P. A. LOUKAKOS, M. LISOWSKI, G. BIHLMAYER, S. BLÜGEL, M. WOLF, AND U. BOVENSIEPEN. **Dynamics of the Self-Energy of the Gd(0001) Surface State Probed by Femtosecond Photoemission Spectroscopy.** *Phys. Rev. Lett.*, **98**(9):097401, 2007. [110](#)

## BIBLIOGRAPHY

---

- [146] A. MELNIKOV AND U. BOVENSIEPEN. *Coherent Excitations at Ferromagnetic Gd(0001) and Tb(0001) Surfaces*, **1** of *Dynamics at solid state surfaces and interfaces*. Wiley-VCH, Weinheim, 2010. [110](#)
- [147] M. DONATH, B. GUBANKA, AND F. PASSEK. **Temperature-Dependent Spin Polarization of Magnetic Surface State at Gd(0001)**. *Phys. Rev. Lett.*, **77**:5138–5141, 1996. [111](#)
- [148] A. REHBEIN, D. WEGNER, G. KAINDL, AND A. BAUER. **Temperature dependence of lifetimes of Gd(0001) surface states**. *Phys. Rev. B*, **67**(3):033403, 2003. [111](#)
- [149] PH. KURZ, G. BIHLMAYER, AND S. BLÜGEL. **Magnetism and electronic structure of hcp Gd and the Gd(0001) surface**. *Journal of Physics: Condensed Matter*, **14**(25):6353, 2002. [110](#), [111](#)
- [150] Q. YANG, M. MUNTWILER, AND X. Y. ZHU. **Charge transfer excitons and image potential states on organic semiconductor surfaces**. *Phys. Rev. B*, **80**(11):115214, 2009. [111](#)
- [151] D. M. S. BAGGULEY, J. P. PARTINGTON, J. A. ROBERTSON, AND R. C. WOODS. **Magnetisation and microwave absorption in GdTb alloys**. *Journal of Physics F: Metal Physics*, **10**(5):967, 1980. [118](#), [122](#)
- [152] KEISUKE T. **Magnetocrystalline Anisotropy of Rare Earth Impurities Doped in Gadolinium. I. Heavy Rare Earth**. *Journal of the Physical Society of Japan*, **31**(2):441–451, 1971. [122](#)

## List of publications

- Marko Wietstruk, Alexey Melnikov, Christian Stamm, Torsten Kachel, Niko Pontius, Muhammad Sultan, Cornelius Gahl, Martin Weinelt, Hermann A. Dürr, and Uwe Bovensiepen, **Hot-electron-driven enhancement of spin-lattice coupling in Gd and Tb 4f ferromagnets observed by femtosecond x-ray magnetic circular dichroism**, Phys. Rev. Lett. **106**, 127401 (2011).
- Muhammad Sultan, Alexey Melnikov, and Uwe Bovensiepen, **Ultrafast magnetization dynamics of Gd(0001): Bulk versus surface**, Physica Status Solidi B **248**, 2323 (2011).
- Muhammad Sultan, Unai Atxitia, Alexey Melnikov, Oksana Chubykalo-Fesenko, and Uwe Bovensiepen, **Electron- and phonon-mediated ultrafast magnetization dynamics of Gd(0001)**, Phys. Rev. B (Submitted).
- Muhammad Sultan, Alexey Melnikov, Alfred Hucht, and Uwe Bovensiepen, **Laser-induced demagnetization of Gd(0001): Critical slowing down near the Curie temperature from a time-domain study**, In preparation.
- Muhammad Sultan, Alexey Melnikov, and Uwe Bovensiepen, **Tunability of ultrafast magnetization dynamics through spin-orbit coupling of GdTb alloys**, In preparation.

## Conference contributions

- M. Sultan, A. Melnikov, U. Bovensiepen, **Laser-induced ultrafast magnetization dynamics in Gadolinium**, Winter School on Ultrafast Processes in Condensed Matter ( WUPCOM'09) February 22-27.2009 Winklmoosalm, Reit im Winkl Germany
- M. Sultan, A. Melnikov, U. Bovensiepen, **Separation of magnetic and non-magnetic contributions in the transient MOKE signal on Gd**, 7<sup>th</sup> International Symposium on Ultrafast Surface Dynamics (USD7) August 22-26.2010, Brijuni Islands National Park Croatia
- M. Sultan, A. Melnikov, U. Bovensiepen, **Temperature-dependent femtosecond laser-induced demagnetization of Gd**, International Workshop on Spin Dynamics in Nanomagnets: Dissipative versus Non-Dissipative Processes October 18- 20.2010, Mülheim an der Ruhr Germany
- M. Sultan, A. Melnikov, U. Bovensiepen, U. Atxitia, and O. C. Fesenko, **Laser-induced magnetization dynamics in Gd far away and close to thermodynamic equilibrium**, Winter School on Ultrafast Processes in Condensed Matter (WUPCOM '11) February 20-25.2011 Winklmoosalm, Reit im Winkl Germany
- M. Sultan, A. Melnikov, U. Bovensiepen, **Influence of equilibrium temperature on the femtosecond magnetization dynamics of Gd**, 75<sup>th</sup> Annual Meeting of the DPG and DPG Spring Meeting, March 13-18.2011, Dresden Germany
- M. Sultan, A. Melnikov, U. Bovensiepen, **Concentration dependent ultrafast magnetization dynamics of GdTb alloys**, Exciting Excitations: From Methods to Understanding, SFB 616 Summer School, July 25-29.2011, Waldbreitbach Germany
- M. Sultan, A. Melnikov, U. Bovensiepen, **Critical slowing down in laser-induced demagnetization of ferromagnetic Gd**, IEEE 56<sup>th</sup> conference on magnetism and magnetic materials, Oct. 30 - Nov. 03 2011, Scottsdale, AZ, USA

## Acknowledgements

I would like to express my sincere gratitude to my supervisor Prof. Uwe Bovensiepen for everything from my acceptance to the continuous support and fruitful discussions during the whole time span. The fact that his interest in my project has greatly encouraged me, while his critical questions have helped me rethink some aspects of this work. I am also grateful to Dr. Alexey Melnikov for his support in critical problems and our discussions.

Thank you also to Prof. Martin Weinelt for acting as a second supervisor of my dissertation and the opportunity to present my work in his group several times. I enjoyed the discussions with him as much as his skiing instructions in the Alps during the winter schools. Special thanks to our collaborators: Femtoslicing team at Bessy for XMCD experiments; Prof. O. Chubykalo-Fesenko and U. Atxitia CSIC, Madrid for theoretical modeling; and Dr. A. Hucht, Univ. Duisburg-Essen for valuable discussions.

Thank you to Ms. Dietgard Mallwitz and Dr. Peter West at FU Berlin and Ms. Christina Boese and Mr. Roland Kohn at Duisburg for their support in all bureaucratic, social and computer-related issues; to Dr. K. Sokolowski-Tinten, Dr. A. Tarasevitch, Dr. P. Zhou, Dr. M. Ligges and C. Streubühr for the fruitful discussions in the final stages of my thesis, and to Dr. N. Bergéard for the valuable input and the review of my thesis. I am greatly thankful to Dr. Sabine Prüfer for proof-reading the thesis.

Since I had the chance to work with wonderful people of two groups during this project; AG Wolf at FU Berlin and AG Bovensiepen at Univ. Duisburg Essen, it would be difficult to name them all here. Still, I would like to thank everyone who assisted in any way during this project, for your support as well as for the good company. I would especially like to thank Prof. Martin Wolf for making the times I spent in his group so memorable. I am also indebted to everyone in the cryogenic laboratory, electronics & precision workshops and official staff at FU Berlin.

Last but not least I would like to thank: my family; my parents, uncle and brothers, and especially my wife Hajra and daughter Haadia for their patience during this time; as well as friends for their company and prayers.

This project would not have been possible without funding from the Higher Education Commission of Pakistan and DAAD Germany, as well as from the SFB 616 project for the last year. Thank you.